Master Thesis

Nanowire core-shell heterostructures for photovoltaic applications

Manidakis Emmanouil

Supervisor: Nikos Pelekanos

DEPARTMENT OF MATERIALS SCIENCE AND TECHNOLOGY
UNIVERSITY OF CRETE
FOUNDATION FOR RESEARCH AND TECHNOLOGY OF HELLAS

Committee
Prof. N. Pelekanos (Supervisor)
Assistant Prof. Z. Chatzopoulos
Assistant Prof. G. Kioseoglou

Heraklion, October 2018

Table of Contents

Abstract

Nanowire arrays are intensively studied in view of third generation solar cells applications. Specifically, III-V nanowires are attractive due to their excellent optoelectronic properties as high mobility of the carriers and light emission. These nanowires however suffer from surface parasitic effects. Core-shell nanowire heterostructures reduce these effects and provide many advantages to such as band-gap engineering, antireflective properties and piezoelectric effects due to lattice mismatch of the materials. The critical parameters for an efficient solar cell based on nanowires are the nanowire diameter, height, distance between nanowires and the array's symmetry. In this thesis we study GaAs-InGaAs core-shell nanowire heterostructures for photovoltaic applications. The nanowire samples were grown on Si (111) by Ga-assisted molecular beam epitaxy via the vapor-liquid-solid mechanism. Scanning electron microscopy images were taken in order to study the diameter, the height, density and the parasitic 2D layer in between nanowires on the interface with the substrate. The optical characterization of the samples was accomplished with photoluminescence measurements versus temperature. Subsequently, solar cell devices based on the nanowire samples were fabricated. After fabrication, SEM images were taken again in order to measure the density of the protruding nanowires as only these are important for the carrier collection. The final characterization of the nanowire solar cells was achieved by I-V and spectral quantum efficiency measurements.

Acknowledgments

Firstly, I would like to thank my supervisor professor Nikos Pelekanos for giving me the opportunity as Master student to perform my research in the field of optoelectronics, for his guidance and his trustiness during my experimental work. I would also like to thank Maria Androulidaki for the daily support and inspiration during my experiments, Professor Zacharias Chatzopoulos for nanowire's growth and Siew Li Tan from National University of Singapore for providing the processing of the NW diodes and for her guidance in the analysis of electrical measurements. Additionally, I would like to thank the whole microelectronics research group for the excellent co-operation. Finally, I would like to thank my family because without their trust and support I would not have the ability to finish my research adventure as Master student.

CHAPTER 1

Introduction

Solar energy appears like an endless source of energy that could offer to the planet energy abundance and could replace all other energy sources giving hopeful messages for the future.

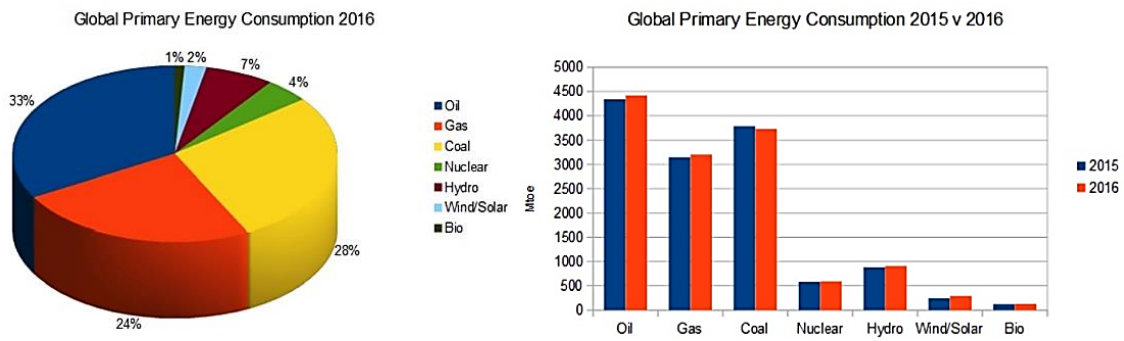

Figure 1. 1 Statistical Review of World Energy, BP Energy Review 2017.

According with the BP energy review, fossil fuels remain dominant with a share of 85% while renewable energy contributes only 2.2%. Full replacement of all fossil fuel sources seems to be impossible but at the same time the development of green energy sources is quite hopeful for the future of our planet.

The research, in order to harvest the Sun's energy is focused on the development of solar cells with various technologies to succeed the best cost-efficient result. The fabrication of solar cells passed through a large number of improvement steps from one generation to another providing a large variety of efficiency values [1].

The first-generation solar cells, mainly single crystals grown on silicon wafers.

- Single/ Mono-crystalline silicon solar cell
- Poly/Multi-crystalline silicon solar cell

The second-generation solar cells—Thin Film Solar Cells

- Amorphous Silicon Thin Film (a-Si) Solar Cell
- Cadmium Telluride (CdTe) Thin Film Solar Cell
- Copper Indium Gallium Di-Selenide (CIGS) Solar Cells

Third Generation Solar Cells

- Nano Crystal Based Solar Cells
- Polymer solar cells (PSC)
- Dye Sensitized Solar Cells (DSSC)
- Concentrating photovoltaic (CPV)

Perovskite Based Solar Cell

Cell type	Crystalline silicon		Thin Film			Third Generation				Perovskites
	Monocrystalline	Polycrystalline	CdTe	CIGS	Amorphous Silicon	Nanocrystal	Dye Sensitized	Polymer	Concentrated	
Efficiency	14% - 17.5%	12% - 14%	9% - 11%	10% - 12%	4% - 8%	7% - 8%	≈10%	≈3% - 10%	≈40%	31%
High temperature performance	Not good at high temperatures	Not good at high temperatures	Good in cool as well as high temperature conditions	Good in cool as well as high temperature conditions	Good in cool as well as high temperature conditions	Excellent thermal stability	Not good in high temperature conditions	Not good in high temperature conditions	Excellent thermal stability	Excellent thermal stability
Size	Significantly less volume to produce the same amount of power	Significantly less volume to produce the same amount of power	Offering a wide range of product design from flexible, light durable	Offering a wide range of product design from flexible, light durable	Offering a wide range of product design from flexible, light durable	Offering a wide range of product design from flexible, light durable	Offering a wide range of product design from flexible, light durable	Offering a wide range of product design from flexible, light durable	Offering a specialized range of product design	Offering a wide range of product design from flexible, light durable
Cost	Two times more expensive compared to thin-film.	Two times more expensive compared to thin-film.	50 percent less expensive than conventional silicon cells	50 percent less expensive than conventional silicon cells	50 percent less expensive than conventional silicon cells	50 percent less expensive than conventional silicon cells	50 percent less expensive than conventional silicon cells	50 percent less expensive than conventional silicon cells	50 percent less expensive than conventional silicon cells	50 percent less Expensive than conventional silicon cells
Additional detail	Oldest PV technology	Economical choice	Toxic due to Cd	Some CIGS have impressive 20% efficiency	Needs long installation time and large space	Needs short installation time and large space	Needs short installation time and large space	Needs short installation time and small space	Needs long installation time and large space	Latest technology. Needs short installation time and minimum space

Figure 1. 2 Comparison of various types of Solar Cells, 2015 [1].

As we observe, different technologies with many advantages and disadvantages have been developed. Nanowire systems belongs to third generation solar cells. In five years, until 2017 the efficiency of nanowire solar cells has improved from 5% to 15% [2].

Nanowire solar cell performance is determined by the diameter of the nanowire, the length, the distance between each nanowire, the array's symmetry, the geometry and the proper selection of the materials [2]. Due to the large surface-volume ratio, recombination effects on the surface reduce the electric response of the nanowires. The core shell structures present a better approach to this problem. The passivation shell enhances the optical and electrical properties of the nanowire, while at the same time core shell heterostructures introduce strain induced by the lattice mismatch of the materials [2]–[6]. The proper selection of the core-shell materials is important to bandgap engineering, for the effective absorption of the light as nanowires can react as antireflective layers, while wave guiding in nanowires is enhancing from piezoelectric fields due to strain effects. All these parameters are decisive for the final efficiency of the solar cell. In this thesis we study GaAs-InGaAs core-shell nanowire heterostructures for photovoltaic applications. Optical properties of nanowires were investigated through photoluminescence measurements at different temperatures. The length, the diameter and the density of each nanowire sample are studied through Scanning Electron Microscopy (SEM). Then, samples are prepared in solar cells in order to study the final properties as solar devices.

Semiconductors

As mentioned previously, the proper selection of the materials is crucial for nanowires, especially for nanowire solar cells. The most important criterium is the bandgap of semiconductors and if it is direct or indirect. The band gap is one of the most important parameters for the efficient absorption of the photon and the carrier generation. Materials from group IV as silicon and germanium, group II-VI compound materials such as cadmium telluride and compound III-V

materials such as gallium arsenide are well known in the solar industry. For core-shell structures also is important the lattice constant of the different compounds.

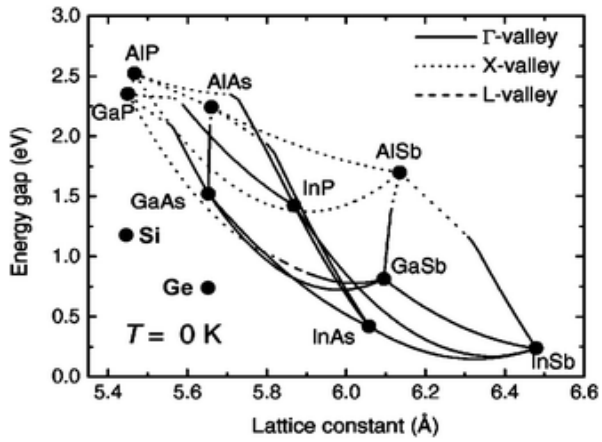

Figure 1. 3 Band gap and lattice constant for various III–V and- group-IV material alloys. The solid lines are direct bandgaps and the dotted are indirect. Si and Ge are indirect [7].

The photovoltaic effect is based on four basic steps, 1) the light absorption, 2) the carrier generation, 3) the carrier separation and 4) the collection of the carriers from the electrodes.

The sunlight energy is composed by photons with different energies. The absorption of the sunlight and the carrier generation are depending on bandgap of the semiconductor and the energy of each photon.

Three different cases can be observed when the incident light heads to the solar cell. If the photon energy is lower than the bandgap (Eph <Eg) the interaction will be very weak with the semiconductor and the photon passes through with no carrier generation. Photons with the same energy with the bandgap of the semiconductor (Eph = Eg) have just enough energy to excite an electron into the conduction band and an electron-hole pair is generated. Photons with higher energy than the bandgap (Eph >Eg) will interact strongly with the semiconductor and will create an electron-hole pair (fig. 1.4).

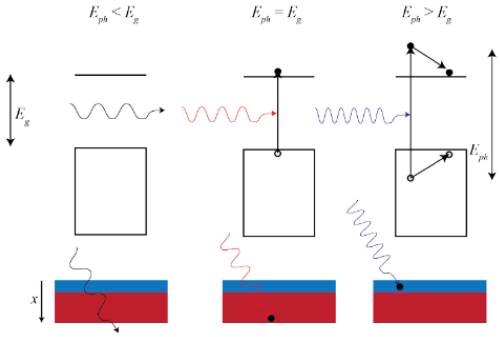

Figure 1. 4 Absorption of the light in a semiconductor [8].

However, the extra energy of the photon will be lost as the electron quickly thermalizes to the edge of the conduction band. The most efficient absorption, including the thermalization effects, happens when the photon energy is equal to the bandgap energy ($E_{ph} = E_g$) so semiconductors with Eg close to Eph of the sun are acceptable for solar cell applications [8].

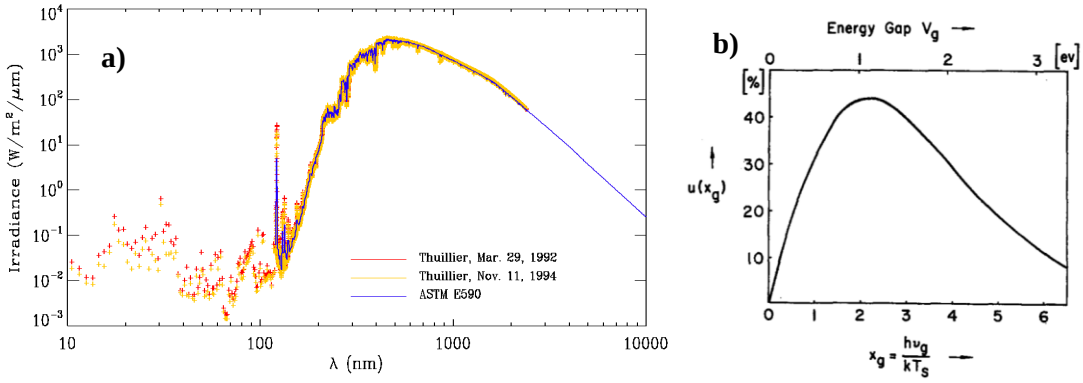

Figure 1. 5 a) Three models of solar cell irradiance measured on the earth [10]. b) The detailed balance efficiency as a function of the bandgap by Shockley and Queisser / Shockley-Queisser (SQ) limit [9].

Solar spectrum is dominated by IR and visible radiations (fig. 1.5, left), so semiconductors with energy band gap around 1.2-1.3 eV are suitable for solar cell applications (fig.1.5, right).

Intrinsic carriers and doping

The photovoltaic effect is based on excitation and carrier generation. In an intrinsic semiconductor the number of free carriers is too low. In order to enhance the number of free carriers and design an electronic potential as well, extra atoms called dopants are introduced and there are two different types: donors which increase the number of free electrons and acceptors which increase the number of free holes. When electrons are majority to a semiconductor it is called n-type while when holes are majority it is called p-type semiconductor. For an intrinsic semiconductor the fermi level is in the middle of the band gap, for a p-type semiconductor the fermi level is closer to the valence band and for an n-type semiconductor it is closer to the conduction band. Heterostructures of p-n semiconductors are used to create p-n junctions.

P-N Junction

When the solar light hits a semiconductor, the free generated photo-carriers have to be separated efficiently and collected by the electrodes. This is the basic operation of a p-n junction. Three different regions can be distinguished in the p-n junction: the p-region, the n-region and the space charge region (SCR) at the interface of the junction (fig. 1.6a). At the SCR, electric field is generated and forces the carriers to move to the electrodes (fig. 1.6b). It is important to find the optimum doping level for the most efficient generation and collection of the carriers.

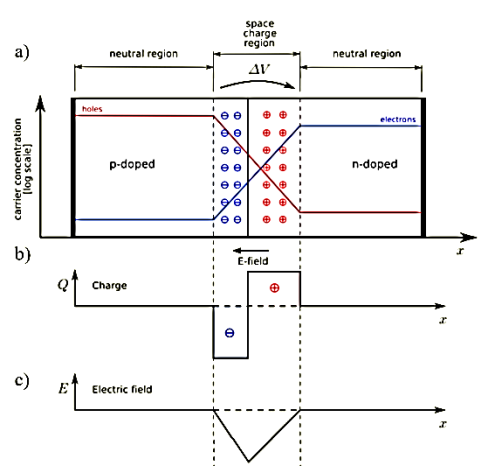

Figure 1. 6 a) A p-n junction at equilibrium with the gradation of the carrier concentrations b) The majority carriers of each region diffuse against their concentration gradient this movement generates two charged regions c) The electric field is generated due to the two charged regions.

Carrier Transport

In a P-N junction the carrier movement happens for two reasons, due to carrier diffusion and due to drift (diffusion and drift current). The diffusion current is driven by the gradient of carrier concentration in order to reach the equilibrium. According to the Fick's law [11]:

$$J_{D_n} = -D_n \frac{dn}{dx} \tag{1}$$

$$J_{D_p} = -D_p \frac{dp}{dx} \tag{2}$$

where D_n and D_p are the electron and hole diffusivity and $\frac{dn}{dx}$ and $\frac{dp}{dx}$ the concentration gradient respectively through the p-n heterostructure. The drift current occurs due to the internal electric field E of the p-n junction. The movement of the holes is through the electric field while for the electrons is opposite of the electric field. The velocity of the free carriers is given as [12], [13]:

$$u_n = -\mu_n E \tag{3}$$

$$u_p = \mu_p \mathrm{E} \tag{4}$$

The total current for electrons and holes respectively is given as [14]:

$$J_n = qn\mu_n E + qD_n \frac{dn}{dx} \tag{5}$$

$$J_p = qp\mu_p E + qpD_p \frac{dp}{dx} \tag{6}$$

Recombination

Recombination effect is observed when the minority carrier of each region is higher than the equilibrium concentration in order to attribute the concentration to equilibrium. Three mechanisms of recombination are identified, Radiative recombination, Shockley-Read-Hall (SRH) recombination [15], and Auger recombination [16].

Radiative recombination is also called band-to-band recombination and happens when an electron from conduction band recombine with a hole from the valence band. In this case a photon generated with energy at or near of the band gap of the semiconductor, depending on the loss mechanism of the material. Radiative recombination is minor for solar cell applications [17]. The total radiative recombination rate, given below as [18] :

$$R = Anp \tag{7}$$

where n and p are the electrons and holes concentrations and A is a constant calculated from the semiconductor's absorption. In thermal equilibrium recombination and generation rate are equal and opposites. The net equilibrium recombination rate U is given as [18]:

$$U = Anp - An_i{}^2 \qquad (8)$$

where the second term is the equilibrium generation rate with $n_i{}^2$ to represent the intrinsic carrier concentration.

Defects in a semiconductor are a parameter which determines the lifetime of carriers. These defects are due to the crystal defects or impurities which modify the electronic structure within the crystal. These defects are also called traps and create energy levels deep in the forbidden band (impurity levels or trap levels) [17]. The Shockley-Read-Hall recombination happens when conduction electrons relax to the defect level and then recombine with the holes to the valence band. The recombination rate R_T is given as:

$$R_T = \frac{np - n_i^2}{t_{h0}(n + n_1) + t_{e0}(p + p_1)} \qquad (9)$$

where τ_{h0} and τ_{e0} are lifetime parameters for holes and electrons respectively, n_1 and p_1 represent the dependence of the recombination rate with the trapping energy level are parameters that introduce the dependency of the recombination rate on the trapping energy level E_τ [18]. SRH recombination also contributes to surface recombination where crystal defects are significant.

Auger recombination is a non-radiative recombination where three particles participate in the process. The energy excess from an electron-hole recombination is transferred to another electron in the conduction band which leads this electron to higher levels. This energy is quickly lost on thermalization in the conduction band; this process is similar with holes at the valence band. Auger recombination is more frequent with high doping levels or under high illumination. The recombination rate for electrons and holes respectively is:

$$R_e = Bn^2p \qquad (10)$$

$$R_p = Bnp^2 \qquad (11)$$

where B is the Auger coefficient of the material [18].

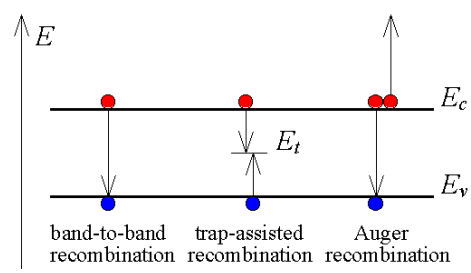

Figure 1. 7 Representation of three types of recombination [18].

P-N Junction as Solar Cell

A P-N junction behaves as a diode when illuminated, as it generates free carriers, which are separated to the SCR region and are collected to the electrodes.

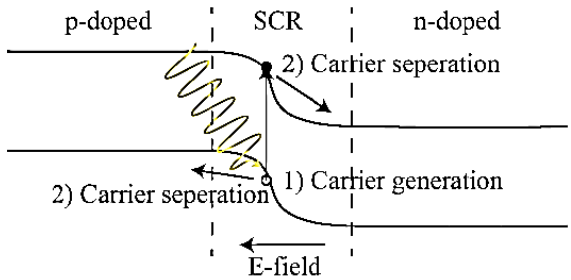

Figure 1. 8 Representation of current generation process to a p-n junction [19]

Otherwise, when we apply voltage to the P-N junction we can still collect carriers to the electrodes although the diode is not illuminated. The dark current equation is given as [8], [20]:

$$J_{dark} = J_{rec} - J_{gen} = J_0 e^{\frac{qV}{nk_BT}} - J_0 = J_0(e^{\frac{qV}{nk_BT}} - 1) \tag{12}$$

where J_o is the thermal generation current density (J_{gen}), q is the electron charge, k_B is the Boltzman constant, T is the temperature, V the applied voltage, n is the ideality factor who shows how close to ideal diode (n=1) is and J_{rec} is the recombination current due to diffusion of the minority carriers at the edge of the SCR through the neutral region.

The ideality factor can be extracted from the dark current equation where the term -1 can be avoided for applied voltage V > 50-100mV is given as:

$$Ln(J_{dark}) = Ln(J_0) + \frac{qV}{nk_BT} \leftrightarrow n = \frac{qV}{(Ln(J_{dark}) - Ln(J_0))k_BT} \tag{13}$$

When the diode is illuminated the current density is given as a superposition of the cell in the dark and the light generation current [21]:

$$J_{total} = J_L - J_{dark} = J_L - J_0\left(e^{\frac{qV}{nk_BT}} - 1\right) \tag{14}$$

Where J_L~J_{sc} is the current generating under illumination.

Three main parameters can be extracted from a J-V curve: the open circuit voltage (V_{OC}) which is the voltage when the current is zero, the short circuit current (I_{SC} or J_{SC}) which is the current when no voltage applied and the fill factor which shows how efficient the generated power can be extracted.

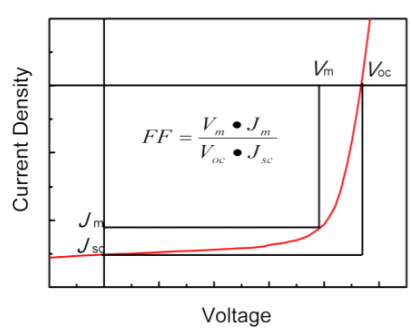

Figure 1. 9 J-V curve for an illuminated diode. The inner box represent the points with the maximum power Pm=VmJm [22].

According to the light generation current, the open circuit voltage is given as:

$$V_{oc} = \frac{nk_BT}{q} Ln(\frac{J_L}{J_0} + 1) \tag{15}$$

For the Fill Factor is given the empirical equation [22] :

$$FF = \frac{\upsilon_{oc} - \ln(\upsilon_{oc} + 0.72)}{\upsilon_{oc} + 1} \tag{16}$$

where,

$$\upsilon_{oc} = \frac{q}{\eta k_BT} V_{oc} \tag{17}$$

The final efficiency of the diode when the incident power light P_{in} is known is given as:

$$efficiency = FF \frac{V_{oc}I_{sc}}{P_{in}} 100\% \tag{18}$$

Loss Mechanisms

During the photovoltaic effect many "parasitic effects" decrease the efficiency of this process. Firstly, when the light hits the surface of the solar cell not all the photons are absorbed. Some of them pass through the device or are reflected. The solution to this problem came with the antireflective layers. The proper selection of the surface material is important and can reduce the reflections at many angles of the incident light.

An extra requirement for the efficient absorption and carrier generation is that the material needs to be thick enough. This requirement is opposite to the requirement of small optical path for the carrier's collections, as thick material means more recombination effects.

Except optical and recombination effects, power losses can be described with parasitic resistivity effects. The most common resistances are series and shunt resistance which can describe efficiently the power losses due to parasitic effects as shown below.

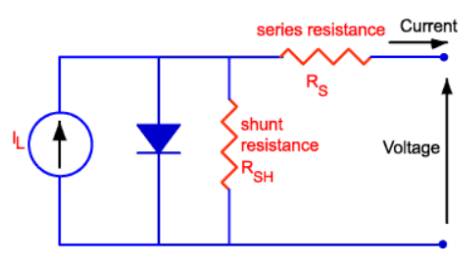

Figure 1. 10 Representation of a solar cell with shunt and series resistance.

The series resistance reflects to the bulk resistance of the semiconductor material, the metallic contacts and interconnections, carrier transport through the top diffused layer, and contact resistance between the metallic contacts and the semiconductor [8].

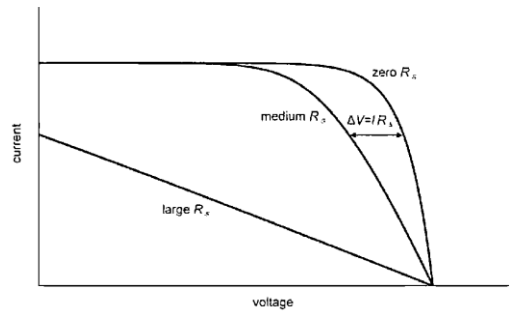

Figure 1. 11 The effect of series resistance to the solar cell.

The main impact of the series resistance is that reduces the FF while at high values reduces also the short circuit current. There is no affect to the open circuit voltage (fig1.11). By taking account the series resistance, the characteristic equation of the diode becomes:

$$I = I_L - I_0\, e^{\frac{q(V+IR_s)}{k_B T}} \tag{19}$$

Near the open circuit voltage, the equation contains information about Rs. By differentiating the eq.19 we have:

$$\frac{dI}{dV}_{I=0} = -\frac{1}{\frac{k_B T}{q I_L} + R_s} \tag{20}$$

The shunt resistance mainly occurs due to manufacturing defects of the device. Low values of R_{shunt} provide an alternative path for the carriers, especially when R_s value is high and significant losses of the device are observed.

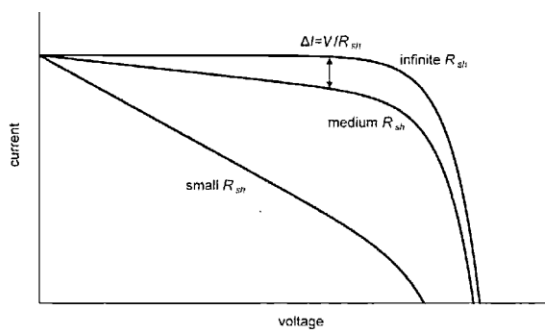

Figure 1. 12 Effect of shunt resistance on the device.

The shunt resistance is also reducing the fill factor and the open circuit voltage. Therefore, no effect of the shunt resistance is observed on the short circuit current. In this case, the characteristic equation of the diode becomes:

$$I = I_L - I_0\, e^{\frac{qV}{k_B T}} - \frac{V}{R_{shunt}} \tag{21}$$

Near the short circuit current, the derivative of the equation contains information about Rshunt, so:

$$\frac{dI}{dV}_{V=0} = -\left(\frac{I_0 q}{k_B T} + \frac{1}{R_{shunt}}\right) \tag{22}$$

In fact, on an I-V measurement both shunt and series resistance participate to the measurement. In that case the diode equation is given by

$$I = I_L - I_0\, e^{\frac{q(V+IR_s)}{k_B T}} - \frac{V + IR_s}{R_{shunt}} \tag{23}$$

Effect of Different Illumination Power

Changing the illumination of the solar cell affects the extracted parameters from an I-V measurement. According with the figure 1.13, the short circuit current and the open circuit voltage are shown that the I_{sc} depends linearly while V_{oc} depends logarithmically with the light intensity [23].

If L is the illumination intensity, $V_{oc,n}$ and L_n the normal values then for the new open circuit voltage the equation is:

$$Voc \approx Voc,n + \frac{nk_BT}{q} ln(\frac{L}{L_n}) \qquad (24)$$

The fill factor FF slightly increases until a point and then it decreases for higher intensity due to series resistance influence. The efficiency increases logarithmically, because the open circuit voltage depends logarithmically as a function of illumination intensity.

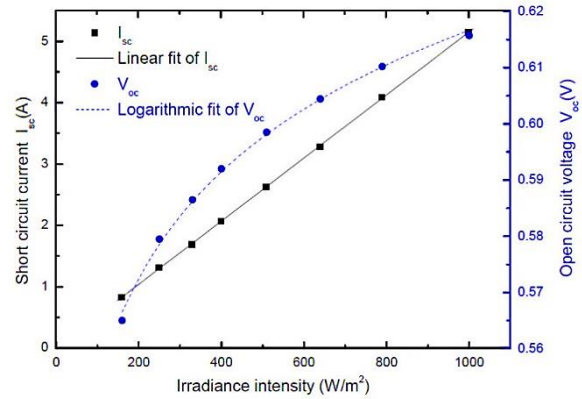

Figure 1. 13 Open-circuit voltage and short-circuit current as function of irradiance for a polycrystalline silicon solar cell [23].

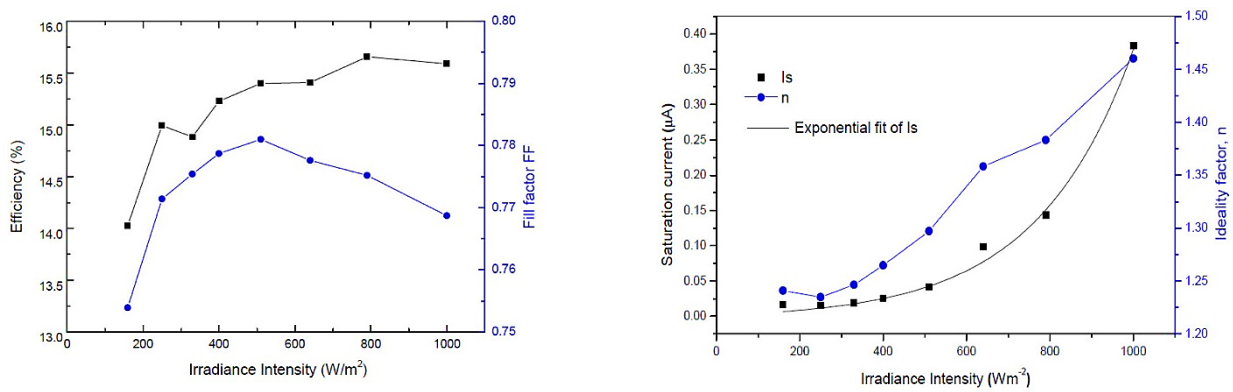

Figure 1. 14 Fill Factor and Efficiency (left), Saturation current and Ideality Factor (right) as function of irradiance for a polycrystalline silicon solar cell [23]

The ideality factor n increases linearly with irradiation to radiation above 350 W/m^2 while the saturation current increases exponentially as [23]:

$$I_s = Ce^{\varepsilon E} \qquad (25)$$

where C and ε are constant values [24].

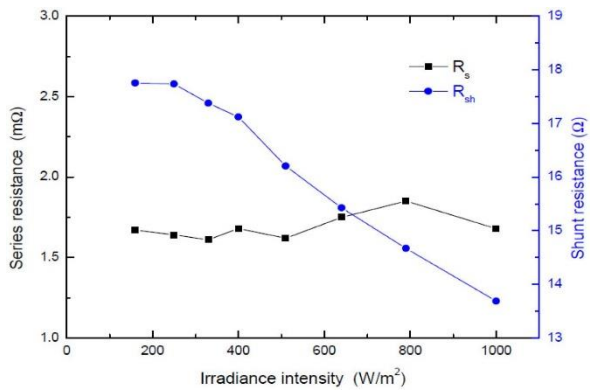

Figure 1. 15 Series and Shunt Resistance as function of irradiance for a polycrystalline silicon solar cell [23].

As we see, there is almost no effect on series resistance by changing the intensity. From the other hand, shunt resistance decreases linearly by increasing the intensity of the irradiance [23].

Responsivity and Quantum Efficiency

Responsivity is a quantity which identify the wavelength where the semiconductor generates more efficient free carriers. The energy of the photons and the energy gap of the material are the main parameter which depends the efficiency of the carrier generation. Especially, responsivity measures how much of the incident optical power is converted to photocurrent and for an ideal diode the responsivity equation is given as [8]:

$$Responsivity(\frac{A}{W}) = \frac{j_{photo}(\frac{A}{cm^2})}{P_{in}(\frac{W}{cm^2})} \quad (26)$$

It is obvious that for lower energies (or higher wavelengths) from the energy gap of the material no carriers are generated.

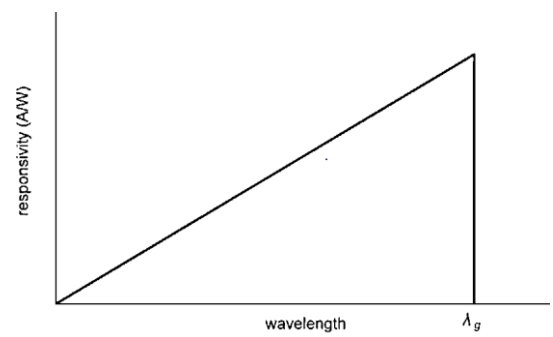

Figure 1. 16 Responsivity as a function of the wavelength.

The most important parameter to identify the real efficiency is the external quantum efficiency which is defined as the number of the extracted carriers to the number of the incident photons. The EQE equation is given as:

$$EQE = \frac{\#n_{out}}{\#n_{in}} = Responsivity \cdot \frac{1239.8}{\lambda(nm)} \quad (27)$$

In ideal conditions, when the energy of incident photons is equal or higher of the energy band gap of the material, the number of the incident photons and the number of the extracted carriers are the same as shown in figure 1.17.

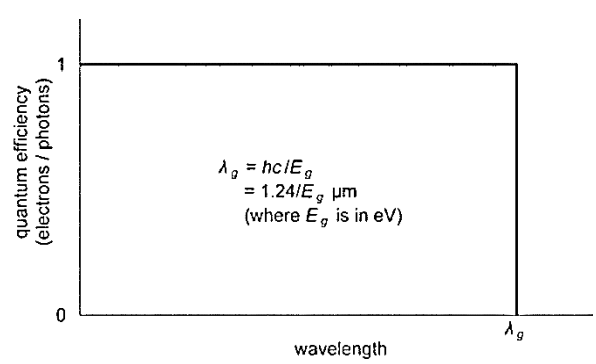

Figure 1. 17 EQE as a function of the wavelength.

CHAPTER 2

Semiconductor Growth

In this thesis, GaAs-InGaAs core-shell crystalline nanowire semiconductors have been grown via MBE on Si wafers. In order to understand the crystal growth mechanism, two different approaches are described, the atomistic approach and the thermodynamic approach.

According to the atomistic model, during the crystal growth, processes of adsorption/desorption, diffusion and incorporation of atoms occur billion of times. When a molecule or atom from vapor phase interacts with the substrate, it loses kinetic energy and becomes adsorbed on the substrate. If the atom/molecule is adsorbed but not incorporated in the crystal lattice it is called adatom. Two different types of adsorption are observed, physical and chemical adsorption. Physical adsorption is caused by van der Waals forces between atoms in close proximity and can be described as a potential well of the order of 10-100meV. Chemical adsorption is caused when adatoms are bounded with the substrate with chemical bonds with a much stronger energy of 1-10eV. Desorption is the opposite process of the adsorption and happens when the adatom has enough energy to escape from the surface. If the adatoms are bound to the surface, they do not incorporate unless they "sit" at energetically favorable incorporation positions. Until then, adatoms diffuse across the crystal's surface among neighboring adsorption sites.

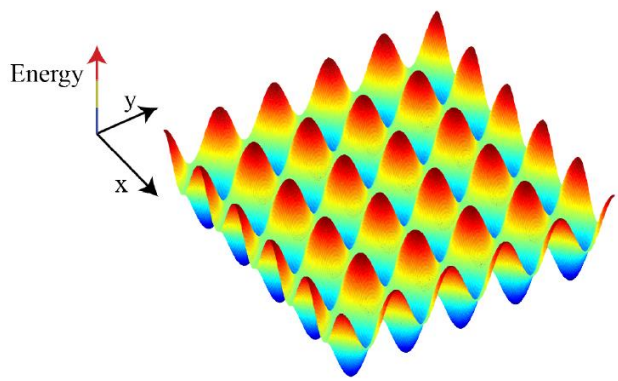

Figure 2. 1 Energy potential on the surface where the adatoms are diffusing until they incorporate to the crystal [19].

When an adatom meets an empty site in the crystal lattice it has the probability to incorporate. After incorporation the potential landscape will change for the next adatom (fig 2.2).

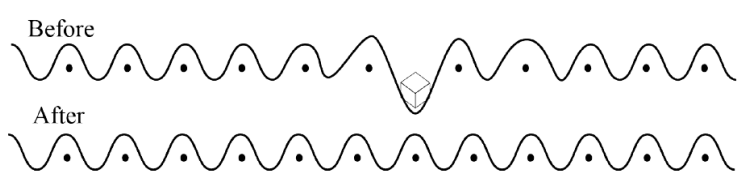

Figure 2. 2 Adatom incorporation from the crystal [19]

Using the thermodynamic approach, we can describe the thermodynamic properties of the involved materials. All processes during the crystal growth are based on the minimization of Gibbs free energy [25]:

$$G = U + PV - TS \tag{28}$$

Where U is the internal energy of the system, P and V are the pressure and volume respectively, T is the absolute temperature and S is the entropy of the system. In any case, the system seeks to minimize its Gibbs free energy. One of the most important aspects of a crystal phase is the chemical potential which is the change in Gibbs free energy when one particle is added or removed from the phase and is defined as the derivative of Gibbs free energy under constant pressure and temperature with respect to the number of particles in the phase:

$$\mu_a = \frac{dG_a}{dN_{a,P,T}} \tag{29}$$

The chemical potential can define if two phases are in equilibrium (in that case the chemical potential of each phase is equal to the chemical potential of the other phase). If the temperature or pressure of one phase is changed, a net transfer of particles is made due to supersaturation and is defined as:

$$\Delta\mu = \mu_a - \mu_b \tag{30}$$

If $\Delta\mu>0$ a driving force transfer particles from a to b until the system reaches equilibrium again. At each transition, there is an energy barrier E_a which the system has to overcome.

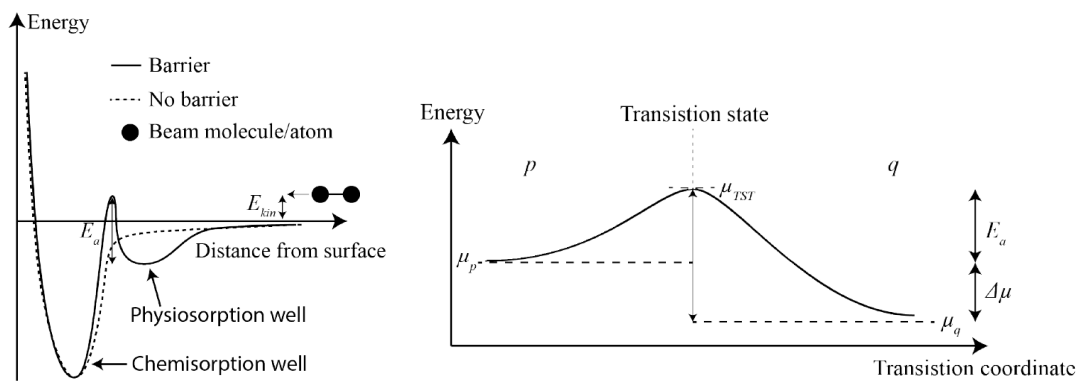

Figure 2. 3 (Left) The potential wells of adsorption. If no bond breaking is needed, there is no energy barrier to chemisorption as shown with the dashed line. If bonds have to be broken before chemisorption can proceed the activation energy E_a has to be overcome, (Right) A general transition between state p and q of chemical potential μ_p and μ_q. There is a difference in chemical potential of size: $\mu = \mu_p - \mu_q$. An energy barrier of Ea has to be overcome for the transition from p to q to take place. In order for the transition to occur it has to pass through a temporary transition state with chemical potential μ_{TST} [19]

In 1889, Svante Arrhenius proposed an equation to describe the rate constant of chemical reactions [26]:

$$\Gamma_{Ar} = Ae^{-\frac{E_a}{k_B T}} \tag{31}$$

where Γ_{Ar} is the rate of chemical reactions, A is the number of reactions attempts per second, E_a is the activation energy, k_B is the Boltzmann constant and T is the absolute temperature.

Molecular Beam Epitaxy

Molecular beam epitaxy (MBE) is a method of growing high-quality crystals. Molecules or atoms are released from effusion cells to the substrate. Effusion cells are special containers with very pure sources that are heated until the desirable materials sublimate or evaporate. As seen in figure 2.4, the growth process takes place in a high vacuum chamber. By opening the shutters of the heated effusion cells, the particles which form a beam, hit and interact with the substrate. A thermocouple is placed behind the substrate to measure the substrate temperature while an in-situ reflection high energy electron diffraction (RHEED) setup probes the planar crystal growth and the surface structure [19].

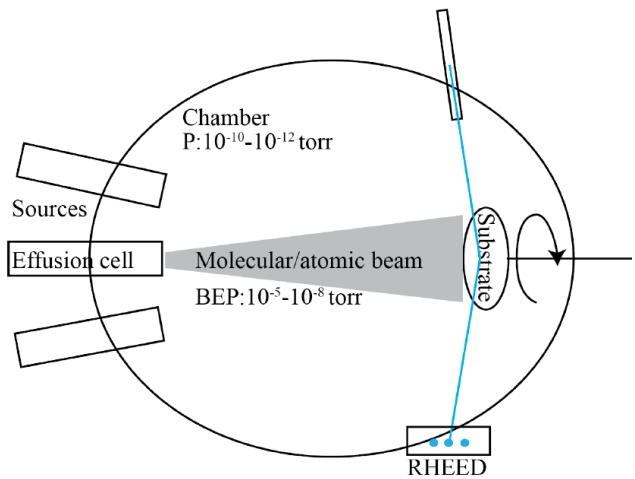

Figure 2. 4 Schematic representation of MBE [19].

Nanowire Growth

Nanowires are crystal structures with high aspect ratio where two dimensions have length scales of a few tens of nm. Due to their dimensions, nanowires are promising for applications in a wide range of areas. Two basic ways to nanowire growth are mentioned, the top down approach and the bottom up approach. The top down approach is less favorable in terms of materials saving and lack of freedom in materials design. On the other hand, bottom up approach provides a high-level control on nanowire geometry, crystal structure, doping and heterostructure formation. Nanowires are a result of anisotropic, 1D crystal growth on a nanometer scale. Many approaches of nanowire growth exist such as metal-catalyst-assisted vapor–liquid–solid (VLS) mechanism, the vapor–solid (VS) mechanism, and the template-assisted (TA) mechanism. In this thesis, VLS mechanism was used. The VLS growth is the most common method due to its simplicity and versatility to semiconductor systems.

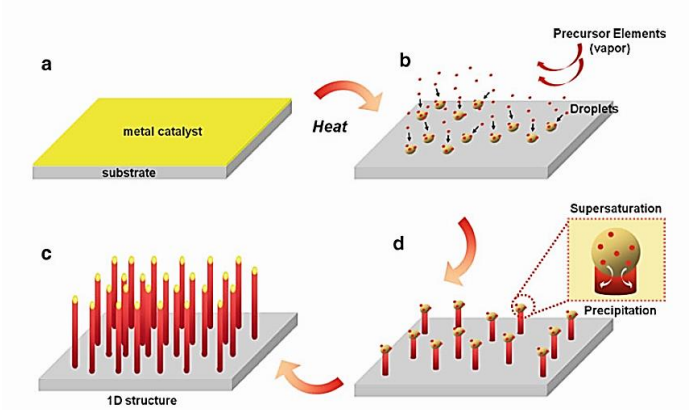

Figure 2. 5 Schematic Representation of VLS growth [27]

VLS growth is based on a catalyst, which forms metallic alloy droplets on the substrate at high temperature. Under certain conditions, the alloy is supersaturated because the concentration is higher than equilibrium concentration. This drives the precipitation of the supersaturated component to the liquid–solid interface to achieve minimum free energy of the system. As long as the vapor components of the effusion cells keep coming, the growth continues. Since the process involves vapor, liquid and solid phases it is called vapor-liquid-solid mechanism [27].
One of the most important benefits on nanowire growth is the creation of heterostructures with reduced requirements of lattice matching.

For axial heterostructures (fig. 2.6a), the growth can be achieved by changing growth precursors during axial nanowire growth, while radial nanowire heterostructures (fig. 2.6b) can be grown by altering growth conditions during synthesis from promoting axial to promoting radial growth [2]. In planar photovoltaic technologies, requirements for lattice matching substrate limited options to high cost materials. In nanowire technologies, the flexibility in lattice matching enables the growth of nanowires on a wide range of substrates.

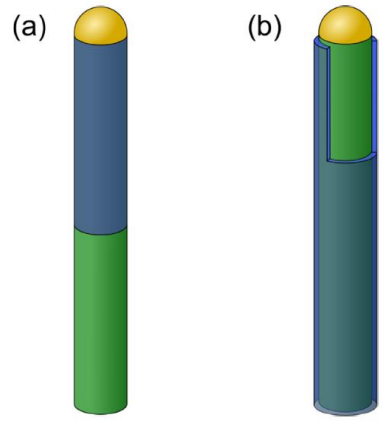

Figure 2. 6 Schematic representation of a) axial and b) radial heterostructures [2].

Individually, III-V nanowires are grown on (111) crystal direction due to low surface energy (or for wurtzite on (0001) direction) [2]. Silicon substrates are well established on nanowire technology. In this thesis, we investigate Ga-assisted nanowires grown on Si (111) substrates with radial heterostructures. The nucleation of GaAs NWs on Si substrate is a very sensitive process and sometimes there are different growth results when same substrates from different batches are used under the same growth conditions. Siew Li Tan et al. [29] described a solution to this problem. Specifically, a controlled chemical oxidation process replaced the native oxide on the Si substrate with a chemical oxide in order to succeed reproducibility on the growth of the GaAs nanowires with no dependence of wafer batch [29].

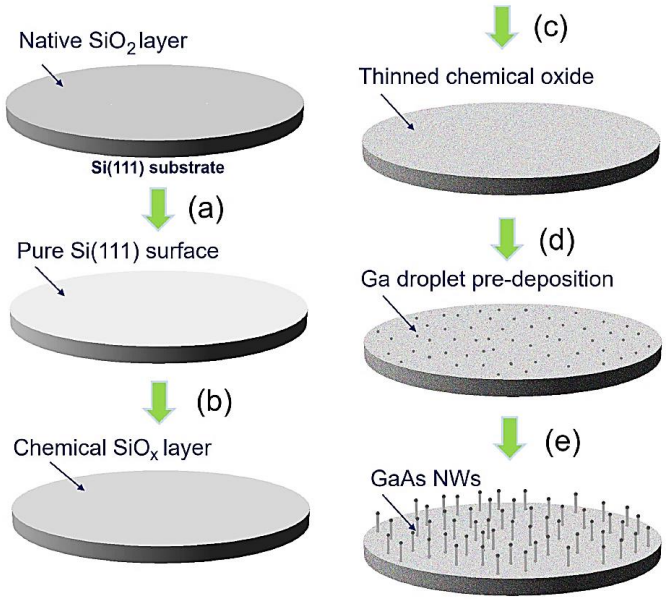

Figure 2. 7 Chemical oxidation process a) remove of native oxide from the substrate b) chemical oxidation of the processed substrate c) thinning treatment of the deposited oxide d) deposition of Ga droplets e) Ga-assisted growth of GaAs nanowires [29]

Comparing the growth process on native and chemical oxide on the substrate, it is observed that the conventional method fails to provide a good control over uniformity, reproducibility and yield of vertical nanowires. Instead, using a controlled chemical oxide provides a high yield of vertical nanowires, excellent uniformity, improved crystalline quality with pure zinc-blade structure, high reproducibility and the ability to produce different combinations of NW's densities and sizes on the same wafer and the same growth conditions [29].

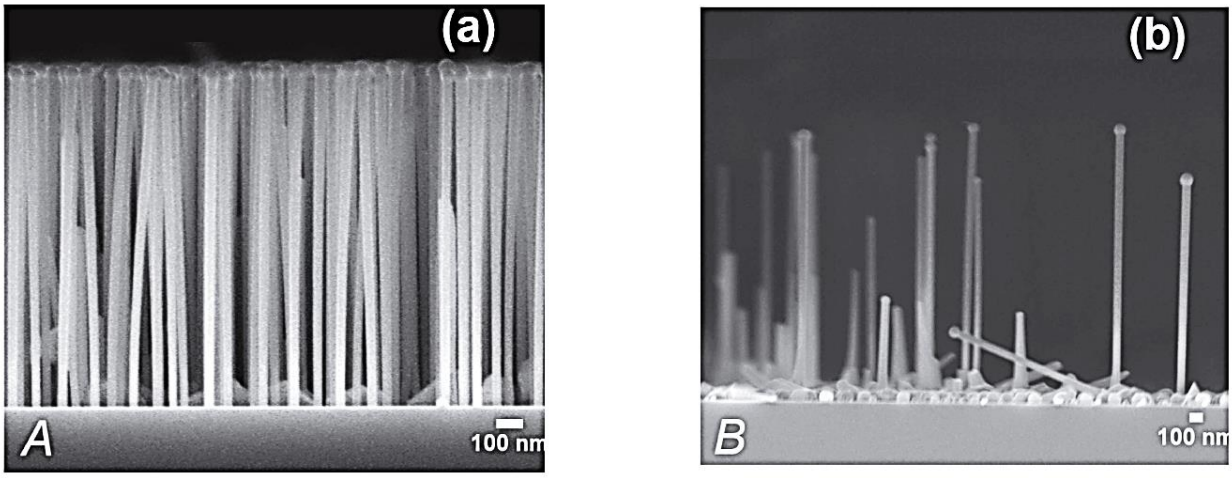

Figure 2. 8 SEM images of Ga-assisted GaAs nanowires on Si(111) substrates covered with a)chemical oxide and b) native oxide. The chem-oxide forms a smooth and highly uniform surface for Ga droplet nucleation with excellent length uniformity and verticality of the grown nanowires [29].

Another aspect of nanowires is that due to their large surface-to-volume ratio, they suffer from surface states. High surface recombination velocity leads to enhanced carrier recombination at the surface of the nanowire and affects the performance of devices. Core-shell structures reduce these effects and provide a better performance for the optical and electrical properties [2]. Furthermore, lattice mismatch between core and shell materials generate piezoelectric fields which boost the e-h pair separation and reduce the recombination losses in order to obtain enhanced NW-based photovoltaic devices [4], [5].

Photoluminescence Mechanism

Luminescence spectroscopy is used to investigate intrinsic electronic transitions and electronic transitions at impurities and defects in semiconductors and insulators. Photoluminescence (PL) is a variant of luminescence, where the luminescence is excited by photons, usually by a laser. The PL technique is used to detect an optical transition from an excited state to an empty lower electronic state, usually the ground state. For the optimum study of the semiconductor transitions, the excitation source energy (laser) should be $hv>E_g$. The PL intensity depends on the relative and absolute concentration of various impurities and defects, the excitation density and the temperature but is not a quantitative technique for measuring the concentration of impurities and defects [30]. Photoluminescence plays a major role in III-V semiconductors because it is a non-contact technique so there is no damage of the semiconductor material during the PL process.

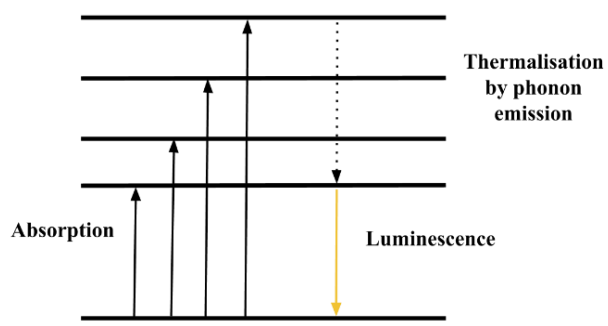

Figure 2. 9 Photon absorption, excitation and luminescence process.

Generally, when the semiconductor is excited with the laser, an electron-hole pair is generated. The way that the e-h pair recombines gives us the respective information of the excitonic transitions. For a defect free semiconductor, the luminescence is dominated by free exciton (FE), donor (D), acceptor (A) and bound-exciton (e-h) luminescence (right path of fig. 2.10). In high purity materials free exciton (FE) luminescence dominates (left path of fig. 2.10). If the semiconductor is extrinsic especially with relatively high doping levels, the free excitons are captured and bound exciton luminescence with sharp lines is observed (second path of fig. 2.10). At high excitation densities, more than one exciton are bound to the donors and acceptors traps and additional satellite lines in the spectrum can be observed and are caused due to the cascade decay of bound-multiexciton complexes (third path of fig. 2.10).

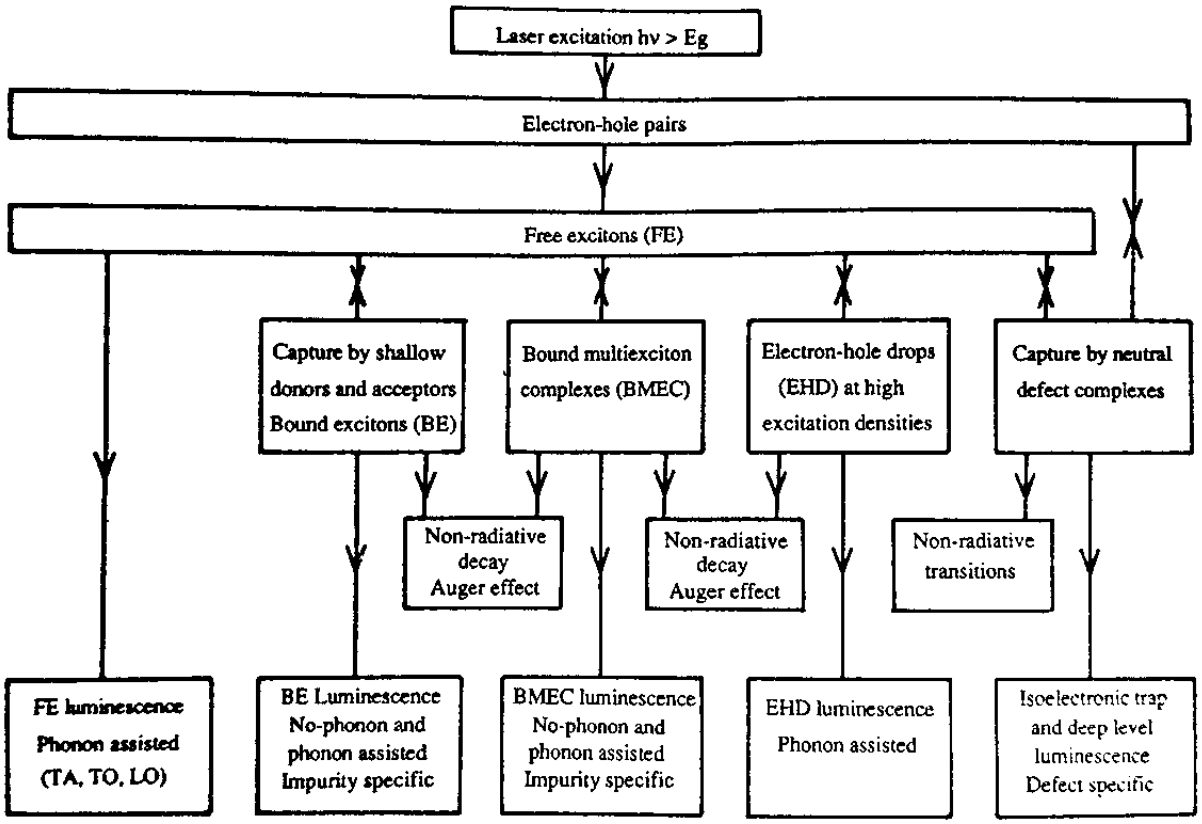

Figure 2. 10 Possible transitions and luminescence meaning [30]

Scanning Electron Microscopy

Scanning electron microscopy (SEM) is a technique which provides the opportunity to observe with a nano-scale resolution. The mechanism of SEM is based on an electron beam which scans the surface of the macrostructure and the signal which is generated is used for the final image. SEM operation is based on secondary electron mode and the depiction of the surface is occurred by secondary electrons and back-scattered electrons. Secondary electrons have low energy, even less than 50eV. Only electrons which are produced near the surface at a depth of 5-50 nm can escape from the material and produce the signal for the imaging of the surface topography (fig. 2.11).

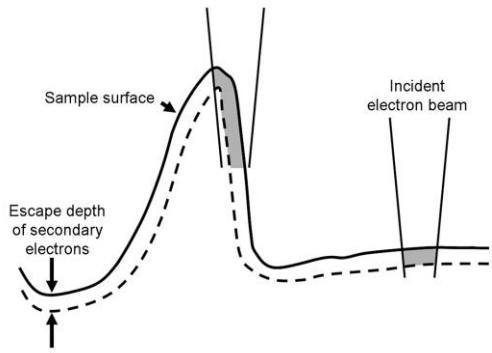

Figure 2. 11 Schematic representation of incident electron beam. The dotted line represents the limits of the escape depth for the electrons. The number of secondary electrons is lower when the beam is perpendicular to the surface while increases with increasing the angle. The shaded area represents the escape volume [31].

Figure 2.12 represents a schematic diagram of SEM. Electrons are extracted from a field emission tip with a moderate accelerating voltage between 1 and 40kV. The diameter of the electron beam has a diameter of 1 to 10 nm. The condenser lens controls the spot size while the objective lens focuses the electron beam into a small probe, which controls the final image. The electron beam convergence angle (α) is controlled by the aperture diameter. In the case of nanowires, the beam diameter, the depth of field and the signal strength are major parameters. A small diameter which is controlled by decreasing the working distance, provides a better image resolution. The depth of field is crucial as nanowires protrude several microns above the substrate and can be increased by narrowing the aperture-thus reducing the angle, or by increasing the working distance. Hence, decreasing the aperture limits the signal strength, while increasing the working distance reduces the image resolution, so an optimization of the SEM parameters is necessary.

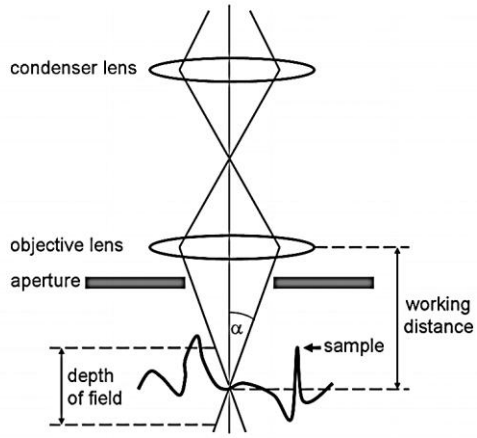

Figure 2. 12 Schematic representation of SEM, showing the working distance and the depth of field [31].

In this thesis, a JEOL 700F field emission scanning electron microscope (FE-SEM) has been used, operated at an accelerating voltage of 15kV, in order to identify nanowire structure and morphology, such as diameter, height, density etc.

CHAPTER 3

Core-Shell Nanowire Structures

Because of small diameters, III-V nanowires often suffer from strong surface effects leading to low optical efficiencies. Surface states are acting as non0radiative carrier traps and as source of potential fluctuations associated with surface-trapped charges, which both affect their optoelectronics properties. The core shell nanowire heterostructures present a solution to this problem.

F. Jabeen et al. [3] report InGaAs/GaAs core-shell nanowires grown by MBE. They claim that core-shell heterostructures where $E_g^{core} < E_g^{shell}$ provide an attractive solution to improve optical efficiency. In addition, the large gap material can also act as carrier reservoir for the inner core and as refraction-index adapter. They demonstrate that the InGaAs/GaAs nanowires luminesce with two to three orders of magnitude higher intensity than bare InGaAs nanowires grown under the same experimental conditions (fig. 3.1).

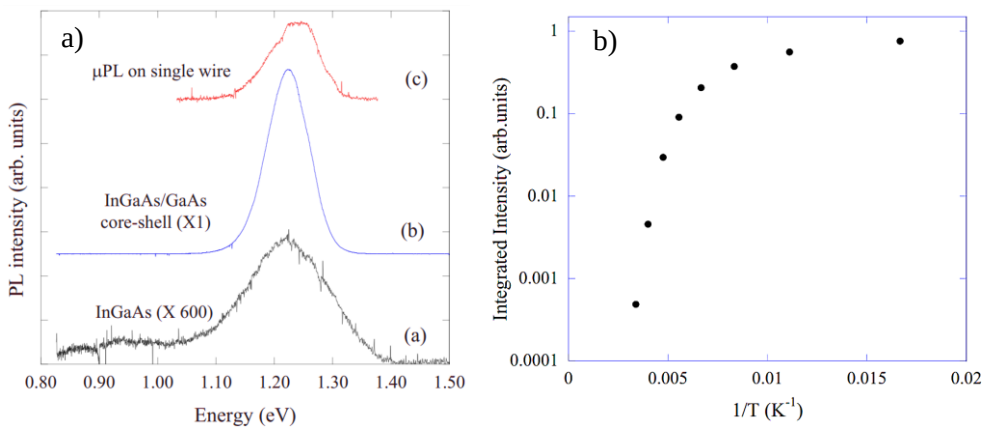

Figure 3. 1 a) PL spectra at 14 K of InGaAs NWs (a); InGaAs/GaAs core-shell NWs (b). Notice that the spectrum relative to the InGaAs wires is magnified by a factor of 600 with respect to the spectrum of the core-shell wires. (c): μPL spectrum taken at 5 K from the single InGaAs/GaAs NW. The zero lines of spectra are shifted for clarity. b) Arrhenius plot for $In_{0.35}Ga_{0.65}As$/GaAs core-shell NWs. The excitation power is 1 mW [3].

Especially, as seen in figure 3.1a, the PL energy position is almost the same for InGaAs NWs and InGaAs/GaAs core-shell NWs (1.22-1.25eV). Therefore, the growth of the shell does not modify the energy position of the PL (sometimes a blueshift is observed), but the line shape of the core-shell NWs is narrower. These features suggest that some In–Ga local rearrangement may occur during the shell growth, a kind of self-annealing, thus improving the general crystal quality of the material.

The In content of the NWs studied in Figure 3.1 is x= 0.35. The band gap at low temperature for unstrained zinc-blende InGaAs of this concentration is 1.043 eV,[32] a substantially smaller value than what is observed in PL spectra. This could be explained by assuming a wurtzite lattice structure which should increase the band gap of the material by 5%–10%,[33] giving a value that is closer to the observed one. A small contribution, of the order of 20 meV, could be attributed to carrier confinement.

As seen in figure 3.1b an intensity drop of more than three orders of magnitude is observed in the case of core-shell NWs from 14 K to room temperature, similar to what is observed in InGaAs/GaAs quantum well structures [34].

K.Moratis et al. [4] report a different kind of core-shell nanowires. In this article GaAs-InGaAs core-shell nanowires are investigated for photovoltaic applications. The band-gap engineering, the antireflecting properties of the shell and the piezoelectric fields due to lattice mismatch of core-shell heterostructures suggest a thorough investigation of these structures. In this paper, GaAs-InGaAs nanowires are grown on n^+ Si (111) substrate with molecular beam epitaxy via VLS method.

Computing methods are used to investigated the PZ polarization density from the strain tensor ε_{ij} and Poisson equation.

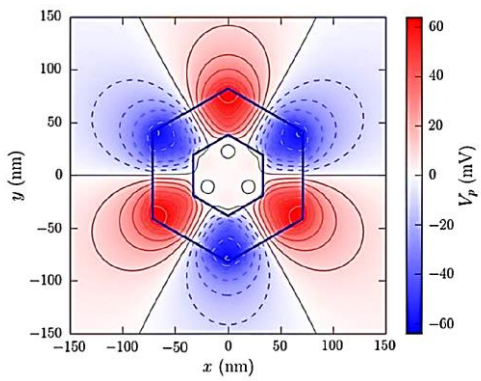

Figure 3. 2 Piezoelectric potential profile for an electron in a cross-section for a core-shell GaAs-$In_{0.05}Ga_{0.95}As$ nanowires with 70nm width fir the core and 40nm thick shell [4].

According to figure 3.2, significant PZ fields are generated. The potential difference between minima and maxima is ~100meV, strong enough for efficient separation of the photogenerated carriers which can minimize the recombination effects.

FE-SEM images carried out to investigate surface morphology and structural characteristics.

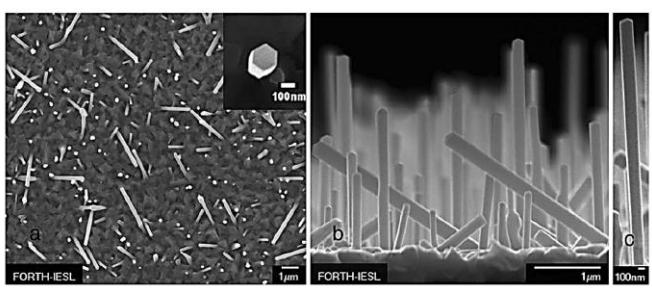

Figure 3. 3 a) FE-SEM image of core-shell GaAs/InGaAs nanowires with ≈50-nm shell thickness, with hexagonal morphology b) Side view of the same sample c) Close-up view illustrating small tapering effect of the core-shell nanowires [4].

As we observe, over 60% of the nanowires are grown perpendicular to the substrate while most of them display hexagonal morphology with {110} lateral facets and average density 10^8 NWs/cm^2 (fig. 3.3a). Figure 3.3c shows a small tapering effect with a diameter increasing by 5-10%.

Photoluminescence measurements are also obtained in the case of optical characterization of the nanowires.

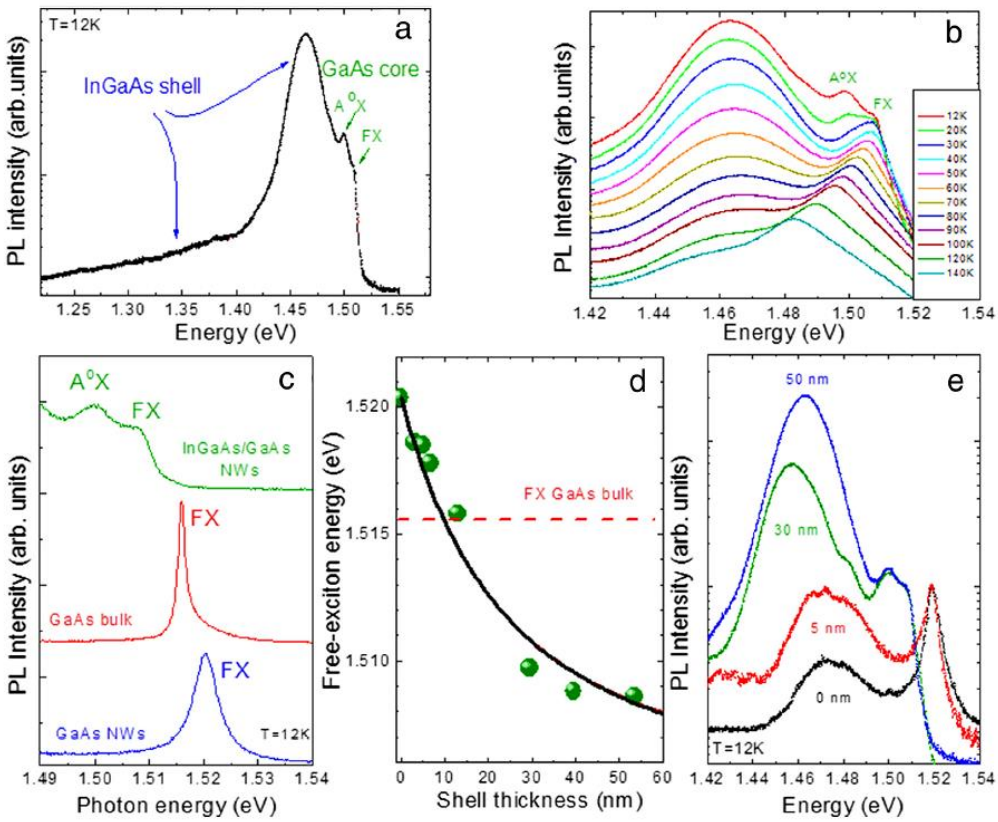

Figure 3. 4 a) PL spectrum at 12 K from a core-shell NW sample with ≈50-nm shell thickness, b) Temperature-dependent PL measurements from the same core-shell NW sample with ≈50-nm shell thickness c) Comparison of low-temperature PL spectra at the GaAs band edge between the core-shell NW sample with ≈50-nm shell thickness, an undoped GaAs bulk sample, and reference GaAs NWs, d) GaAs core free exciton energy position at 12 K as a function of InGaAs shell thickness e) Comparison of low-temperature PL spectra for core-shell NW samples with varying shell thicknesses [4].

In Fig. 3.4a, is presented a low temperature PL spectrum from a core-shell NW sample with ≈50 nm shell thickness. Two GaAs core-related peaks at 1.509 and 1.500 eV are visible, which are assigned as emission from GaAs free-like excitons (FX) and excitons bound to neutral acceptors (A^0X), respectively [35]. This assignment is justified by their temperature dependence, as shown in Fig. 3.4b, where a rapid ionization of the A^0X peak with temperature is observed, while the FX line persists and dominates the whole spectrum. In Fig. 3.4c, the FX emission peaks of the core-shell NWs with ≈50 nm shell thickness, an undoped GaAs bulk sample, and the reference GaAs NWs are presented. A first observation is that the FX peak of the reference GaAs NWs, situated at 1.520 eV, is blueshifted by as much as 4.5 meV with respect to the FX position of bulk GaAs. This blueshift is attributed to quantum confinement effects as the NW diameter decreases [36]. On the other hand, the FX peak of the core-shell NW sample is characteristically redshifted with

respect to the reference GaAs NWs, and as shown in Fig. 3.4d, the redshift increases with the InGaAs shell thickness, clearly suggesting that it is caused by the strain imposed to the core by the shell layer.

As seen again in PL spectrum of the core-shell NWs (Fig. 3.4a), the InGaAs shell gives rise to a broad emission spectrum from about 1.48 eV down to 1.23 eV. The intense PL peak around 1.46 1.47 eV, which is present in all core-shell NW samples with shell thicknesses above 10 nm, cannot be attributed to donor acceptor-type recombination [37] in the GaAs core and one reason is that it dramatically acquires strength as the shell thickness increases, as visible in figure 3.4e.

Single core-shell GaAs/AlGaAs nanowires grown by MBE via VLS method are investigated by L.V.Titova et al. [38]. In this letter the low temperature optical emission properties of bare GaAs and core shell GaAs/AlGaAs nanowires are examined; for eight different core-shell nanowires with average diameter of 80nm measured at 10K. PL spectra consist of a single broad peak at 1518eV which correspond well to free exciton emission in bulk GaAs. The large peak width and the variability in the peak position corresponds to the variations in the blueshift of the exciton emission energy due to strain and nonuniformity of nanowires (fig. 3.5a), while a dramatic increase in luminescence efficiency of the core-shell structure, over one order of magnitude, is observed in comparison with the bare nanowires (fig. 3.5b).

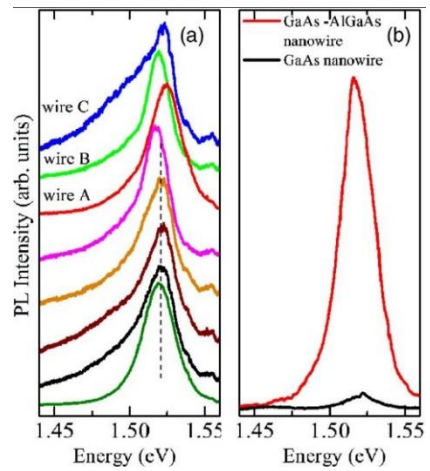

Figure 3. 5 PL spectra of: a) eight different GaAs-AlGaAs nanowires at 10K b) bare and core shell nanowires [38].

GaAs/AlGaAs core-shell nanowire structures are also investigated from M. Hocevar et al. [5]. In this paper, the optical properties are investigated and it is verified that the AlGaAs shell not only provides an excellent passivation of the GaAs core but also changes its band structure due to strain effects. Photoluminescence measurements are obtained in order to investigate the optical properties of the NWs. Additionally, time-resolved μ-PL measurements are employed to study the carrier dynamics.

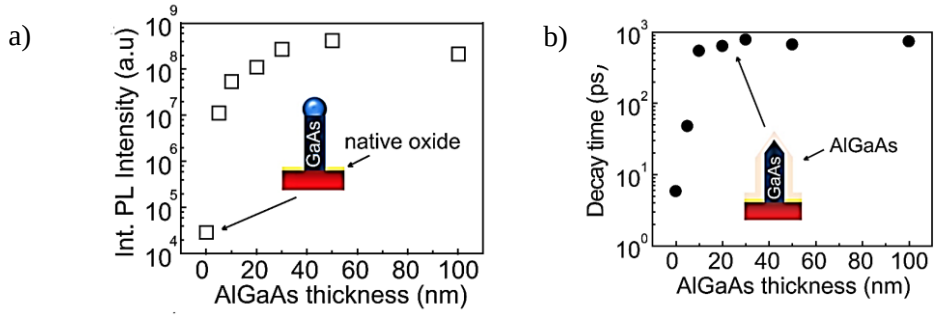

Figure 3. 6 a) Integrated photoluminescence intensity versus shell thickness at 5 K. b) Decay time of the photoexcited carriers versus shell thickness at 5 K [5].

Figure 3.6a show the spectrally integrated PL intensity at 5K from various nanowires with different shell thickness. Evidently, bare nanowires have low emission while for core-shell nanowires the intensity increases by increasing the shell thickness and saturates for shells thicker than 20nm with a reinforcement of over than four orders of magnitude. Figure 3.6 b shows the low temperature PL decay time of the band edge excitonic emission as a function of shell thickness. As observed, the decay time increases with increasing the shell thickness by more than two orders of magnitude, which reveals that the passivation shell reduces the non-radiative recombination channels at the surface of the core [5], ensuring lifetimes close to the intrinsic limit [39].

Considering the PL spectra in the region of GaAs core emission, it is observed a systematic red shift of the PL peak and broadening of the PL linewidth by increasing the shell thickness (fig. 3.7a).

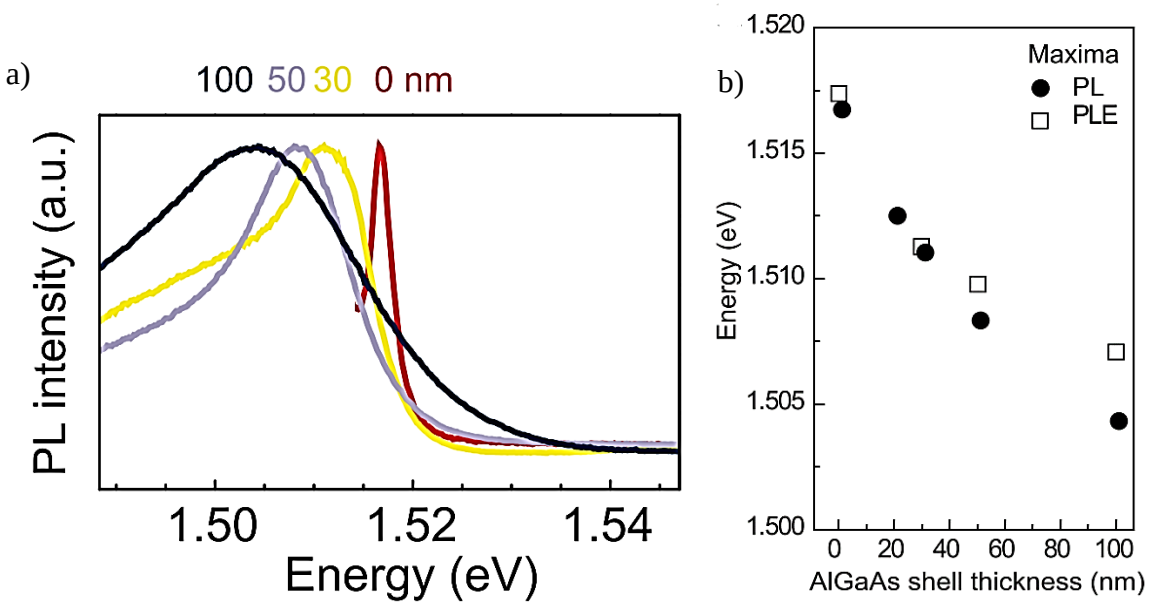

Figure 3. 7 a) PL spectra of nanowire ensembles with shell thicknesses varying from 0 to 100 nm at 5 K. c) Shift of the band edge emission and absorption photon energy versus shell thickness at 5 K [5].

Figure 3.7 b suggest a mechanism where the strain in the core increases by increasing the shell thickness. Micro-PL measurements also detect a shell-dependent localization mechanism related to inhomogeneities within the shell along the NW axis. As seen in figure 3.8a several discrete emission peaks appear above the GaAs energy gap in a range of 1.55-1.7eV, energies much lower than the energy gap of a homogeneous $Al_{0.35}Ga_{0.65}As$ alloy (E_g=2eV). This is clearer in figure 3.8b where by considering that the core material increasingly feels the strain of thicker shells, localization energies of several meV can be easily generated in the core assuming variations of the Al content along the nanowire axis between 0-40%.

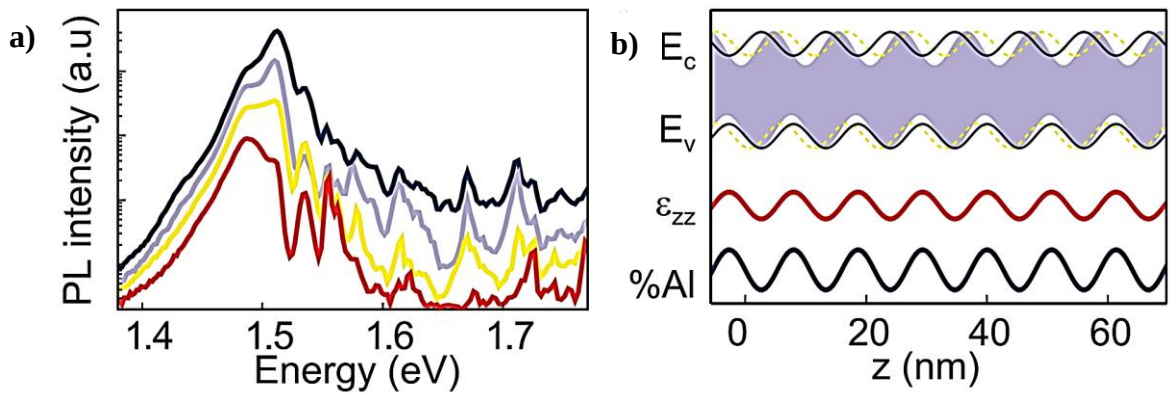

Figure 3. 8 a) μ-PL at 5 K of few 100 nm-thick core-shell nanowires, where the excitation power increases from P to 4P from bottom to top (P =0.5 mW). The main PL peak at high powers corresponds to the GaAs band edge emission discussed throughout this work. The PL peak at lower energy (1.49 eV) is associated to a band-to acceptor transition involving residual carbon. b) Scheme of the total variation of the GaAs band structure (light blue area) along the z-axis due to the simultaneous presence of strain (blue line) and PZ fields (yellow dotted line) induced by variations of the Al content in the shell over length scales comparable to the exciton Bohr radius. Holes and electrons are spatially confined along the nanowire axis [5].

A similar GaAs/AsGaAs core shell heterostructure is also reported from Th Kehagias et al [40]. Nanowires are grown on n-type Si (111) substrate via Ga-assisted VLS mechanism. The optical properties of the nanowires are investigated with temperature depended macro-PL measurements.

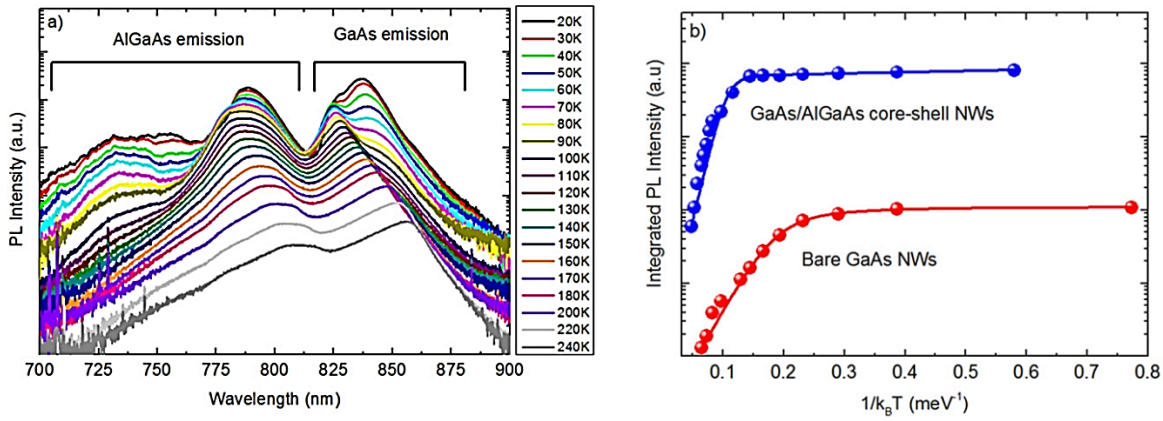

Figure 3. 9 a) Temperature-dependent PL measurements of ensemble GaAs/AlGaAs core–shell NWs. b) Arrhenius plots of the spectrally integrated GaAs FX emission for the GaAs/AlGaAs core–shell NWs and a reference sample with bare GaAs NWs of similar structural characteristics [40].

As seen in figure 3.9a two emission regions are observed in the PL spectra. The first region for wavelengths shorter than 800nm is attributed to recombination at localized centers in the AlGaAs shells. When the temperature increasesthe higher energy (lower wavelengths) side of AlGaAs region losses intensity faster while the 790nm peak persists up to 240 K. An Arrhenius plot of the 790 nm peak gives a thermal activation energy of ~110meV which is in agreement with the strongly localized nature of the specific recombination.

The second region is for wavelengths higher than 800nm and is attributed to GaAs core emission. More precisely, at low temperature the dominant peak in the range of 820-840nm range is around 837nm and is attributed to donor-acceptor recombination. By increasing the temperature, this peak is rapidly decreasing giving rise to free excitons recombination. The FX GaAs peak at 20 K is 1505eV. The red shift with respect to bulk materials is a consequence of the residual strain and piezoelectric effects according to M. Hocevar et al. [5].

Figure 39b shows an Arrhenius plot of the reference bare GaAs nanowires in compare with GaAs/AlGaAs core-shell integrated GaAs FX emission. The PL intensity of the core-shell nanowires is increases by two orders of magnitude compared to the bare nanowires, proving the efficient passivation of the core surface by shell. Additionally, the FX PL drop for the bare nanowires is already visible at 60 K with an activation energy of 35meV, while for the core-shell nanowires the drop starts at 120 K with the corresponding the activation energy increasing to 80meV. As a result of the passivation AlGaAs shell, the activation energy is enhanced for the GaAs core due to thermal de-trapping of carriers localized in the AlGaAs shell and subsequent transfer to the GaAs shell.

Nanowire core-shell devices

As previously mentioned, semiconductor nanowires are under extensive research due to their unique properties which provide a wide range of applications. Nanowires constitute promising building blocks for future applications such as LEDs, lasers, photodetectors and photovoltaic devices.

E. Dimakis et al. [41] employ coaxial multishell Nanowires for near-infrared LED emission. The GaAs-based nanowires are grown catalyst-free on Si substrate by MBE method.

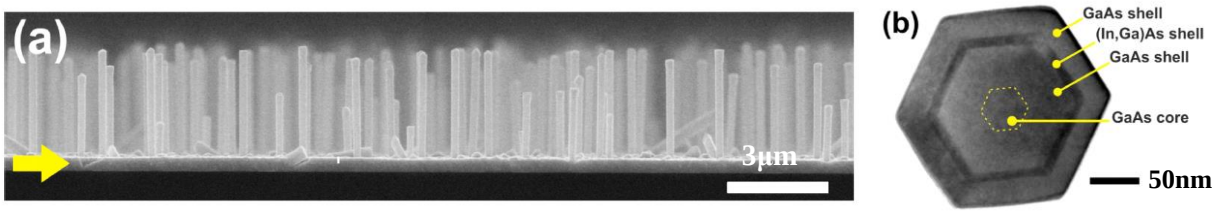

Figure 3. 10 a) Side-view SEM image of nanowires grown on Si(111). The arrow indicates the parasitic layer. b) TEM image of single nanowire, showing the coaxial heterostructure [41].

Figure 3.10a illustrate a SEM image, showing the morphology of an as grown sample, with a density of the free-standing nanowires of ~ 10^8 NWs/cm^2. Figure 3.10b illustrates a TEM cross-section image of the multishell structure around the 50 nm thick GaAs core, which consists of a 50 nm thick inner GaAs shell (this is indicated artificially, because it cannot be distinguished from the GaAs core), an 11 nm thick (In,Ga)As intermediate shell that appears as a well-defined hexagonal stripe with dark image contrast, and finally, a 30 nm thick outer GaAs shell.
The device structure is illustrated in figure 3.11. The cross section of the LED NWs is sketched in figure 3.11a where the core and each shell are shown with different colors. Figure 3.11b with the false color shows that light was emitted only from the radial QWs inside the NWs, while no emission is recorded from the highly defective parasitic layers (where the carrier recombination via defect-states is mainly nonradiative).

Figure 3.11c shows a side-view SEM image of the fully processed device. The n-type shell was contacted from the front side of the device with sputtered indium tin oxide (ITO), while the p-type shell was contacted through the p^+−Si substrate with an aluminum back-contact. A 1.5 µm thick benzocyclobutene (BCB) layer was employed to electrically insulate the ITO contact from the substrate. The device consists of approximately 10^5 parallel contacted NWs (assuming that all of them have been contacted successfully).

The I-V plot of the device is presented in figure 3.12. The leakage current is in the range of a few µA for a reverse bias of 10 V, which is satisfactory considering the ambiguous quality of the p−n junction at the defective NW tips, where no CL signal was never detected, and the NW bases, where the shells are in contact with the defective parasitic layers.

The Si-oxide layer should also be the source of the series resistance that limits the current at high voltages [41].

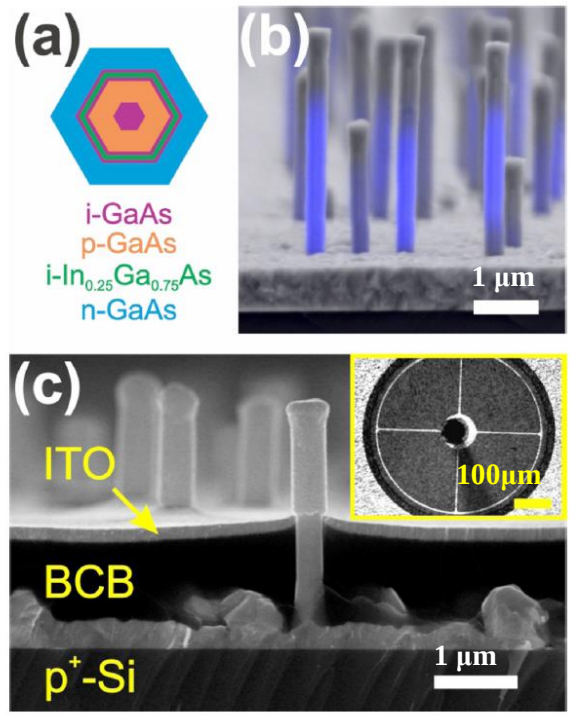

Figure 3. 11 a) Cross-sectional schematic of the (In,Ga)As/GaAs LED NWs. b) False-color monochromatic CL map of the as-grown LED sample at 7 K. The probe wavelength was 940 nm. c)Side-view SEM image of the fully processed LED. Inset: Top-view optical image of the LED [41].

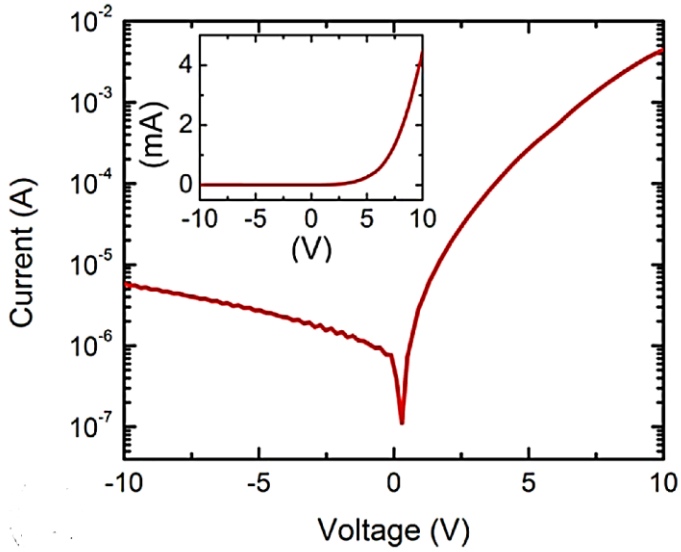

Figure 3. 12 Current−voltage characteristic of the (In,Ga)As/GaAs NW LED. Inset: The same characteristic in linear scale [41].

Using the characteristic, I-V for these device (fig 3.12), I try to extract the characteristic values of the dark I-V, according to the analysis as shown in chapter 4 for the dark I-V's in our NW devices.

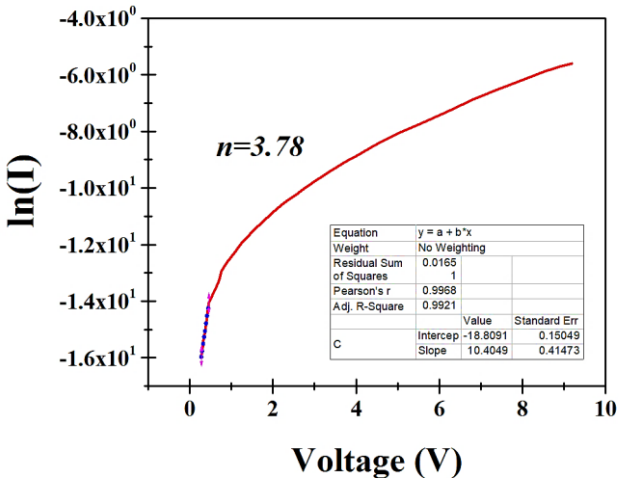

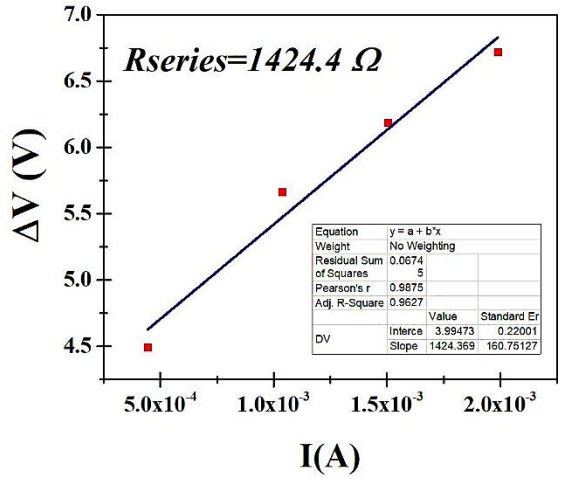

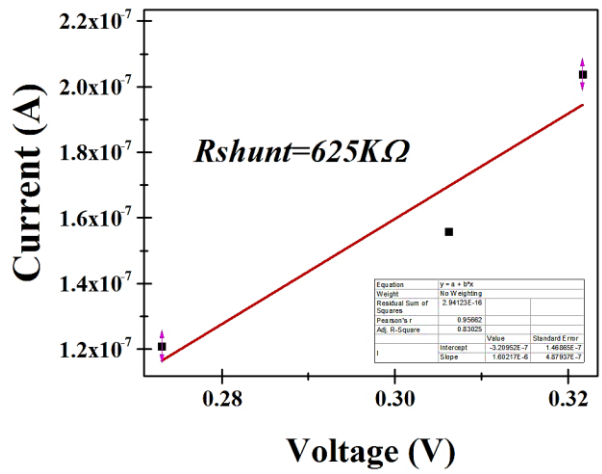

Figure 3. 13 a) The extracted ideality factor from the dark I-V using linear fitting for low values of voltage is n=3.78. b) The series resistance is R_{series}=1.424KΩ while, c) the shunt resistance give values close to 625KΩ.

In order to compare the diode values with our results, the extracted values were multiplied with the area of the diode and the ''effective'' area which represents the area of the nanowires in 2D for each diode area ($A=10^{-3}$ cm^2 and $A_{active}=3.14\ 10^{-5}$ cm^2). The multiplied parameters are given in the table below:

$R_{series}A\ (\Omega cm^2)$	$R_{series}\ A_{active}\ (\Omega cm^2)$	$R_{shunt}A\ (\Omega cm^2)$	$R_{shunt}\ A_{active}\ (\Omega cm^2)$
1.42	0.045	625	20

Table 1. Extracted series and shunt resistance multiplied with the diode area and the effective area of the nanowires

The diode characteristics approaching the bulk limits in GaAs nanowire array photodetectors is investigated from A. C. Farrell et al. [42]. They present a p-type GaAs core nanowire with an

InGaP passivation shell grown on n-type GaAs substrate by selective-area metal−organic vapor deposition (SA-MOCVD) as shown in figure 3.14.

The ideality factor and the dark current density are investigated in order to examine the effectiveness of passivation layer. Using the Shockley equation:

$$I = I_0 \cdot (e^{\frac{V - I \cdot R_{series}}{n \cdot k_B \cdot T/q}} - 1) \qquad (32)$$

for an 80µm diameter NW array area (~5026 NWs) with I_0=4.8 10^{-12} A, n=1.15 and R_s=1.8Ω as fitting parameters as shown in figure 3.14a. In figure 3.14b is illustrated the ideality factor for different values of temperature and voltage (inset). Since series resistance is not considered when extracting the ideality factor from the slope of the current, the ideality factor at high forward bias is not actual, but an effective ideality factor [43]. The ideality factor reaches at the value of 1.1 at 250K.

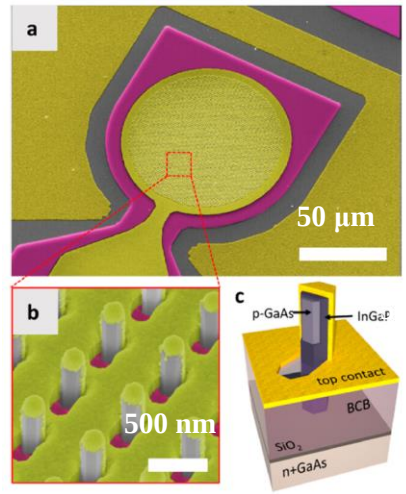

Figure 3. 14 a) SEM image of fabricated nanowire array photodetector. b) Close-up view of active area showing a nanowire array. c) Schematic of the device structure [42].

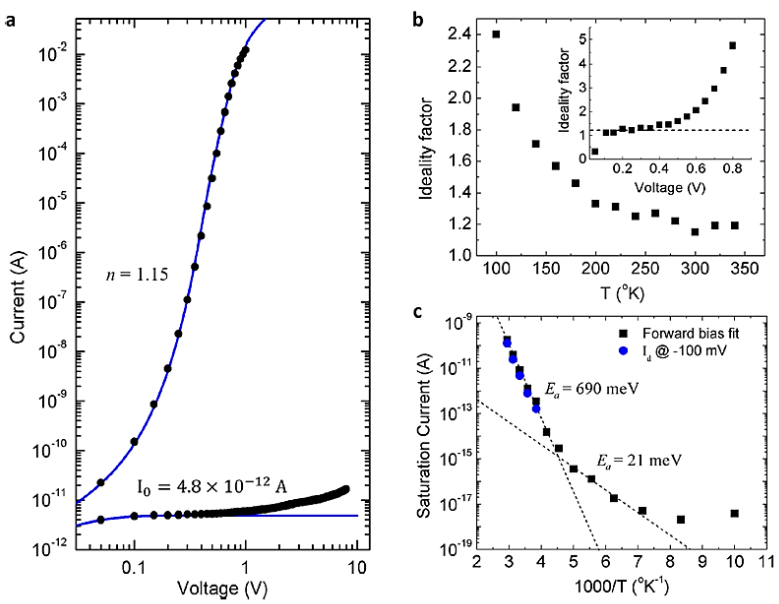

Figure 3. 15 a) Measured (symbols) I−V of a typical photodetector at room temperature and the calculated (line) I−V using the Shockley equation. b) Temperature dependence of the ideality factor. Inset: Bias dependence of the ideality factor at room temperature. c) Arrhenius plot of the saturation current [42].

In figure 3.15c an, Arrhenius plot of the saturation current is used to extract the activation energy. giving E_a = 690 meV at room temperature and E_a = 21 meV at low temperature. The activation

energy at room temperature is roughly half the bandgap of GaAs, indicative of states in the midgap while the low temperature activation energy of 21 meV is likely due to zinc dopants and/or carbon impurities.

Krogstrup et al. [43] measure the electric characteristics of a single-core-shell p-i-n junction GaAs nanowire solar cell grown on silicon substrate (fig. 3.16). The GaAs nanowire solar cells, are grown on a silicon substrate, where the p-section is contacted through a highly doped substrate and the n-section through a transparent top contact. The electric characteristics are extracted from dark current-voltage measurements and photo measurements under AM 1.5G illumination (fig. 3.17). In the dark IV, the extracted ideality factor of the device is η=2.6 while for the photo IV the short circuit current is 256pA. By dividing the short-circuit current with the apparent NW cross section area of 180 mA/cm^2 . Additionally, the open-circuit voltage is 0.43V while the FF=52%. Dividing the generated power density (P_{in}=40mW/cm^2) with the extracted power density extract the efficiency of the device ~40% [43].

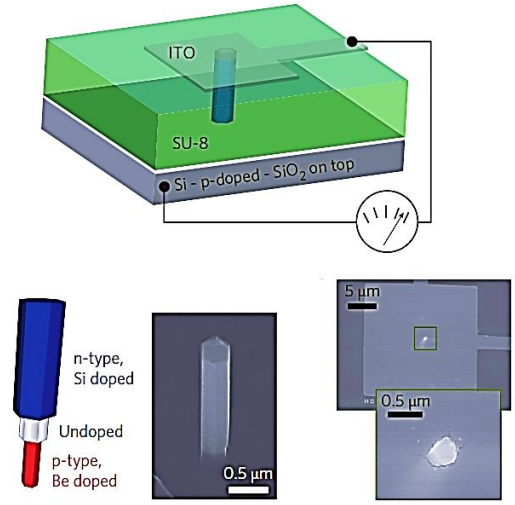

Figure 3. 16 Schematic of the vertical single-nanowire radial p–i–n device connected to a p-type doped silicon wafer. A p-type doped core is in contact with the doped silicon substrate and an n-type doped shell is in contact with the ITO. SEM image of a nanowire solar cell before adding the top contact, shows a 30º angle from the vertical. The SEM images of the device is illustrated from the top electrode. The nanowire is ~2.5 mm high and has a diameter of ~425 nm [43].

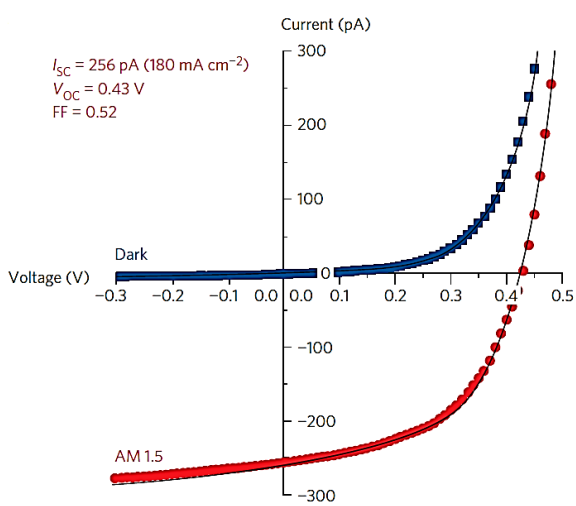

Figure 3. 17 Dark and Photo I-Vs of the device [43].

InGaAs axial-junction nanowire-array solar cells with AlInP passivation layer are fabricated and discussed by Nakai et al. [43]. The InGaAs nanowires are fabricated by calatyst-free selective-area metal organic vapor phase epitaxy (SA-MOVPE) on p-type GaAs(111)B substrate with a pitch of 600 nm and 0.9x0.9mm^2 active area containing ~ 6 10^6 NWs. After nanowire growth, the nanowire array was filled with BCB for electrical insulation. The photovoltaic performance of this device was measured under 1 sun illumination (fig. 3.18).

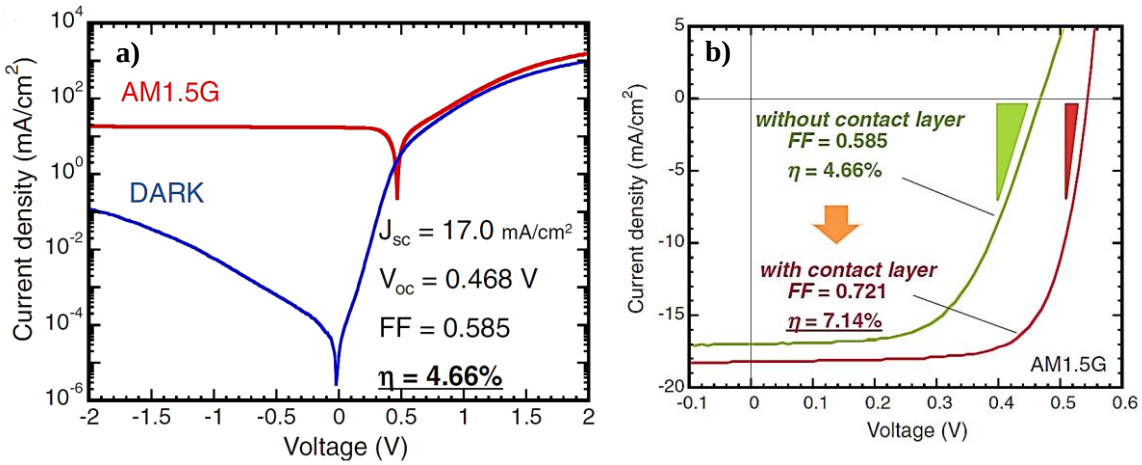

Figure 3. 18 a) Characteristic dark and photo (1sun illumination) J-V of InGaAs NWs array. b) J–V characteristic of InGaAs NW-array SCs with and without tin-doped layer [44].

The extracted parameters of the J-V analysis show a I_{SC}=17 mA/cm^2, V_{OC}=0.468V, FF=58.5% and n=4.66%. Additionally, the ideality factor is 1.46 while the series resistance 4.723 Ωcm^2, much higher than that of conventional SCs. The high value of resistance is considered to be due to the contact resistance between the ITO and GaAs-based NWs. In order to restrict the series resistance effect, a Sn-doping contact layer is introduced between ITO and nanowire array, formed by pulse doping. This contact layer improved significantly the SC performance (fig. 3.18b).
The improved structure of the SCs exhibited an V_{OC}=0.544V, a I_{SC}=18.2 mA/cm^2, a FF=72.1% and an efficiency of n=7.14% under 1 sun illumination. The series resistance also improved dropping down to the value of 0.132 Ωcm^2.

CHAPTER 4

Experimental part

Nanowires

In this chapter we present the fabrication method as well as the optical and structural characterization of the nanowire samples. All samples are core-shell nanowires with different architectures in order to study the behavior of samples with different widths, lengths, densities and structures.

All samples are grown by Molecular Beam Epitaxy (MBE) using the Vapor-Liquid-Solid (VLS) growth method. An n^+ Si (111) (ρ_{Si}=0,01 Ω·cm) wafer from Siltronics prepared in Ultra High Vacuum (UHV) conditions is used as substrate. The first step of growth process is the annealing of the substrate at ~640°C for 10 minutes, a very important step for the "porosification" of the native oxide on Si (~1nm) and the nucleation of Ga droplets on pores of the oxide. After annealing, the temperature decreases to 600°C and a flux of Ga atoms for 20 seconds creates droplets on the substrate (fig. 4.1a, b). For the core, a flux of Ga and As atoms is released and the atoms incorporate through the Ga droplets for 30 minutes to grow the GaAs nanowire (fig. 4.1c, d). After the growth of the core, the Ga droplets still exist at the top of the nanowires, so As flux remains open for 10 minutes to eliminate these droplets and create a triangular top of the intrinsic GaAs (~30nm) core (fig.4.1e, f).

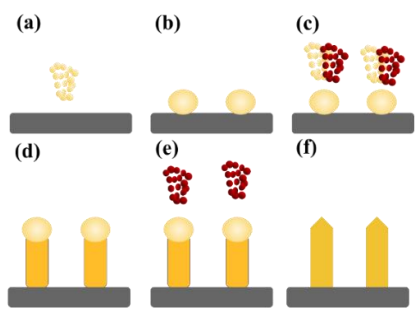

Figure 4. 1 VLS growth steps of GaAs nanowires.

Two different samples have been grown with an intrinsic GaAs core. For the first sample (438) following the core growth the temperature decreases at ~510°C and atoms of Ga, As, In and Be (dopant) are released. The shutter remains open for 40 minutes till a 30nm thick p^+ $In_{0.1}$ $Ga_{0.9}As$ shell is formed. After that process, the In shutter closes, Ga, As and Be remain open for 3 minutes and an additional 3nm of p^+ GaAs is created.

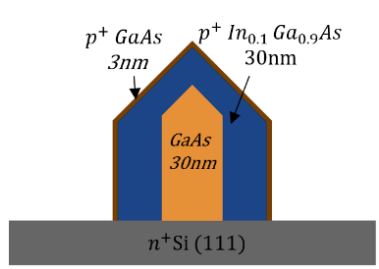

Figure 4. 2 Structure of sample 438.

For the second sample (439), atoms of Ga, As and Be incorporate in the shell for 40 minutes forming a 6nm thick p^+ GaAs shell.

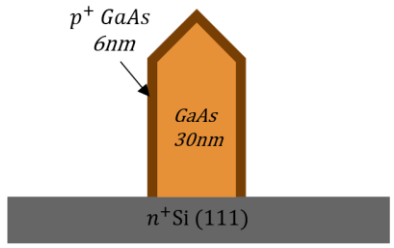

Figure 4. 3 Structure of sample 439.

Similar process of VLS growth take place for the preparation of another set of three different samples, with a p doped GaAs core (~45nm in diameter). For the core, after nucleation of Ga droplets on the Si substrate, flux of Ga, As and Be atoms incorporate in droplets for 20 minutes to generate the core. Then Ga shutter closes and the shutter of As and Be remains open for 8 minutes to consume the Ga droplets and a triangular top of p doped GaAs is created.

After core growth, for 586 sample, the substrate temperature increases from 600°C to ~685°C and shutter of Al, Be and As opens for 10 seconds to create a shell of p^+ AlAs (~0.1nm). After that, all shutters close and the substrate temperature decreases to 510°C. Atoms of In, Ga and Be are released for 40 minutes to create a p^+ $In_{0.1}$ $Ga_{0.9}As$ (~35nm) shell. Afterwards, In flux gives place to Al for 30 seconds and a ~0.5nm p^+ $Al_{0.3}$ $Ga_{0.7}As$ shell frames the outer shell. Ultimately, flux of Ga and As remains open for 3 minutes for the formation of a 3nm p^+ GaAs.

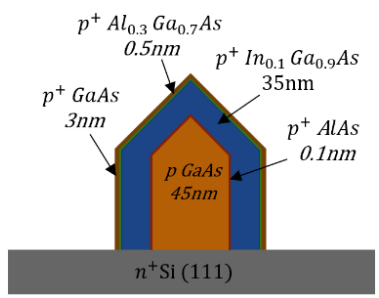

Figure 4. 4 Structure of sample 586.

For 590 sample the process is similar to 586. After the formation of the core, the duration of Al, As and Be flux is 1 minute to create p^+ AlAs shell of 0.5nm. Thence, the substrate temperature goes to ~510°C and In, Ga and Be flux is opened for 40 minutes for the creation of a p^+ $In_{0.1}$ $Ga_{0.9}As$ 37nm shell. Afterwards, the In flux is replaced from Al for 4 minutes and a 4nm p^+ $Al_{0.3}$ $Ga_{0.7}As$ is formed. Finally, flux of Ga, As and Be remains open for 3 minutes to create a 3nm p^+ GaAs.

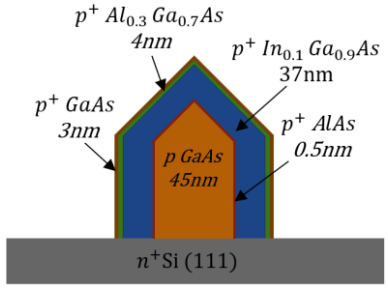

Figure 4. 5 Structure of sample 590.

Ultimately, for 591 sample after the core growth flow of Al, As and Be agglutinate the core for 1 minute to a p^+ AlAs shell of 0.5nm. The substrate temperature decreases to 600°C and Ga, As and Be atoms released to incorporate to the nanowire for 40 minutes forming a 8nm p^+ GaAs shell. Al atoms are released for 4 minutes and a 3nm p^+ $Al_{0.3}$ $Ga_{0.7}As$ shell is grown. Finally, Ga, As and Be atoms are released for 3 minutes for an outer 2nm p^+ GaAs shell.

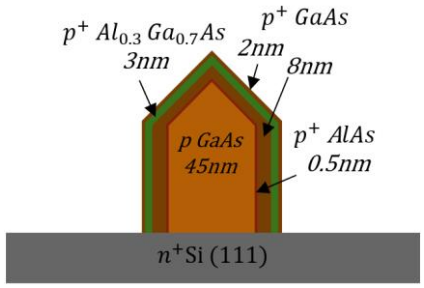

Figure 4. 6 Structure of sample 591.

It is important to notice that the structure dimensions are not the nominal. During the growth process, the incorporation rate is not the same for all the materials mentioned above, so dimensions are results of SEM analysis and growth conditions. Finally, we should mention that the doping level for p^+ and n^+ is $3 \cdot 10^{18}$ cm^{-3} while for p is 10^{17} cm^{-3}. These doping levels are nominal and are based on thin film calibrations.

SEM Analysis of Nanowire samples

To extract statistical data for the structure characteristics of each sample, Scanning Electron Microscopy (SEM) images are analyzed. A SEM cross section image give us information about diameter, length and parasitic layer's thickness. The NW density is extracted from top view SEM images, not shown here. After analysis using ImageJ software, we extract the results below:

For 438 sample:

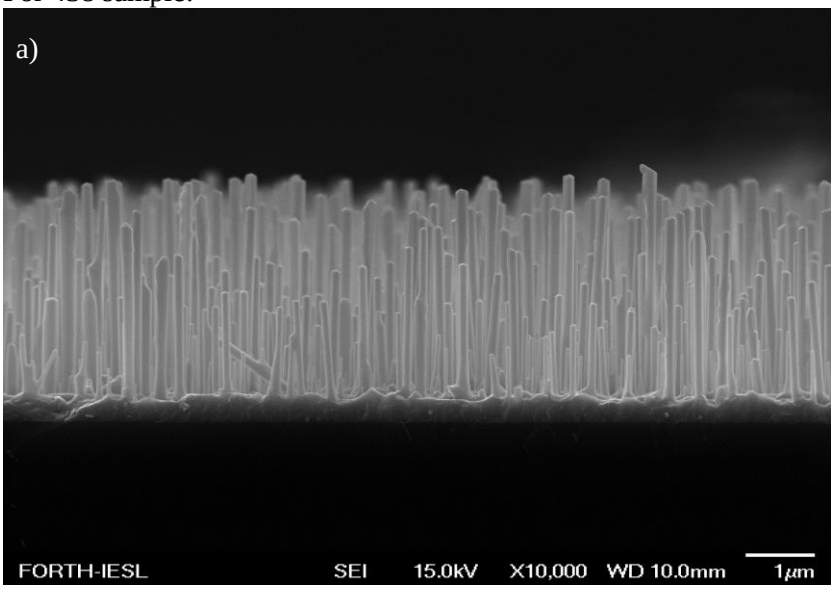

b)

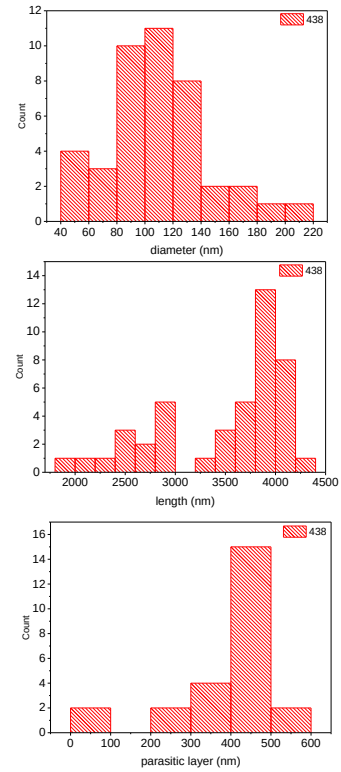

Figure 4. 7 a) 438 cross section SEM Image b) Statistics analysis of 438 with <d>=110 nm, <h>=3.5μm, <P.L.>=396.5nm and <Density>=3x10^{8} $\frac{NW's}{cm^2}$.

For 439 sample:

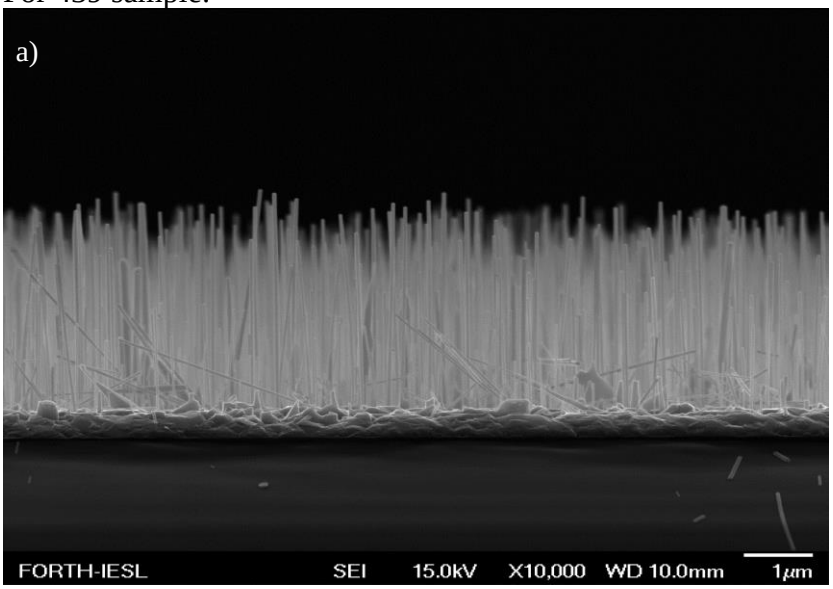

b)

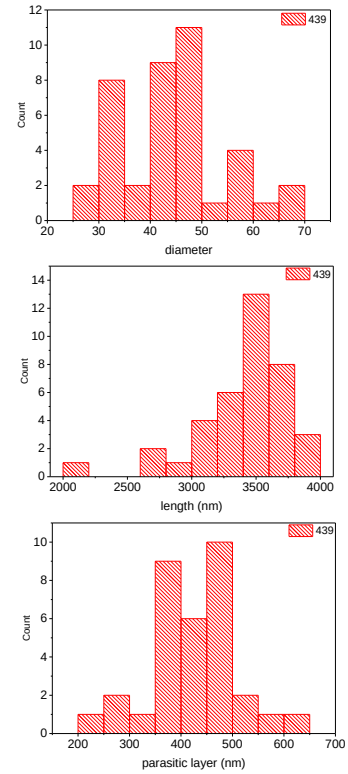

Figure 4. 8 a) 439 cross section SEM Image b) Statistics analysis of 439 with <d>=42nm, <h>=3.4μm, <P.L.>=425.7nm and <Density>=3x10^{8} $\frac{NW's}{cm^2}$.

For 586 sample:

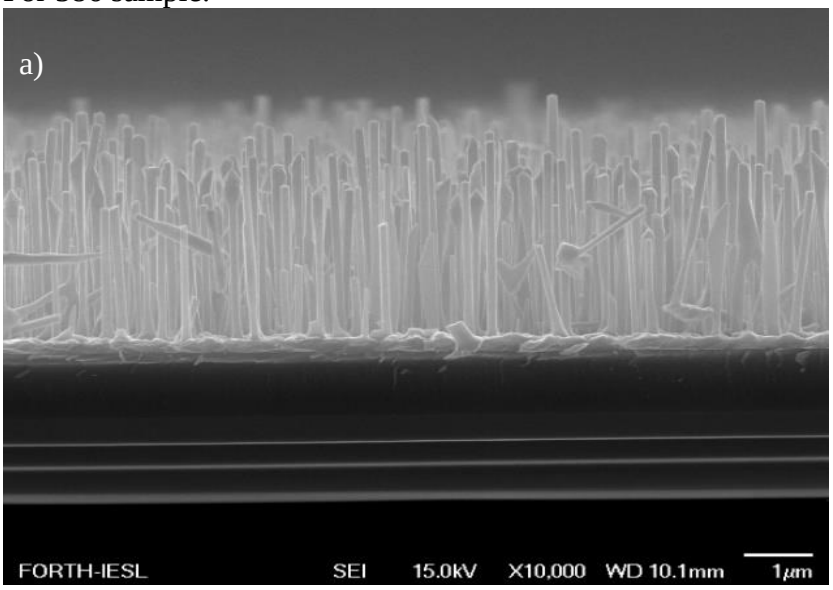

b)

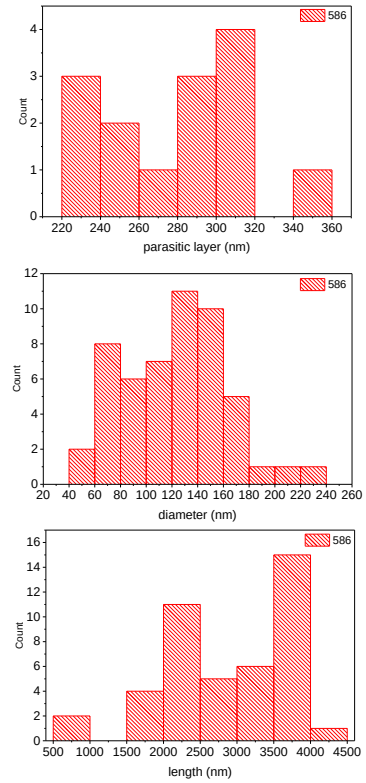

Figure 4. 9 a) 586 cross section SEM Image b) Statistics analysis of 586 with <d>=122.3nm, <h>=2.88 μm, <P.L.>=279.5 nm and <Density>=2.8 x10^8 $\frac{NW's}{cm^2}$.

For 590 sample:

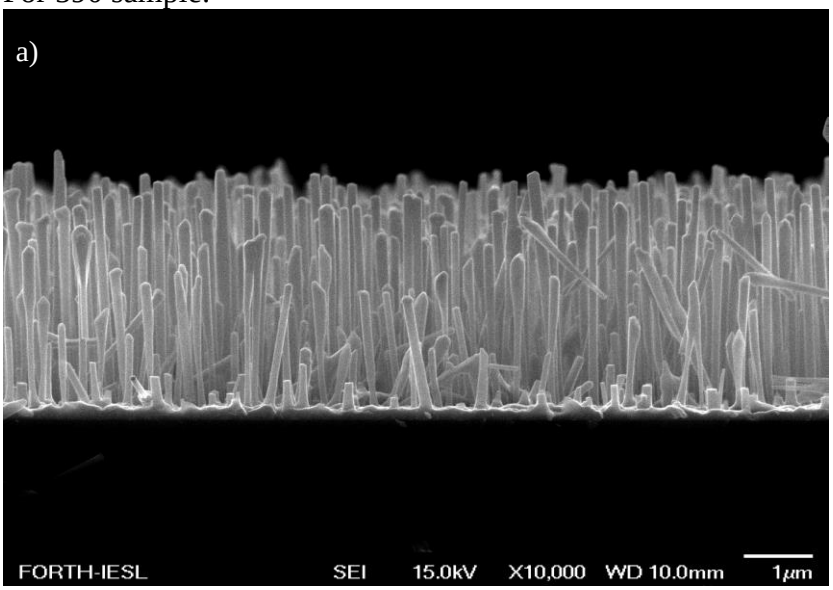

b)

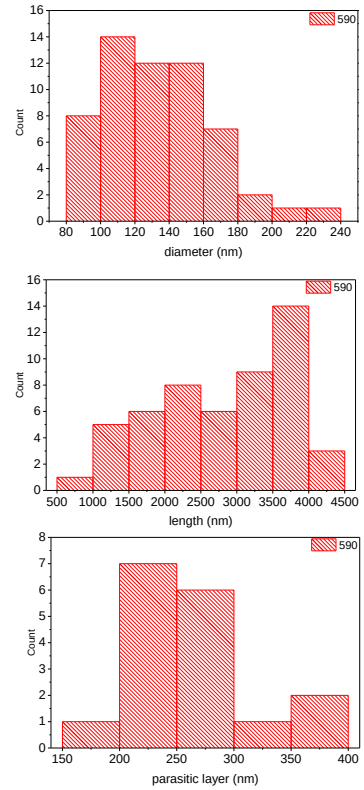

Figure 4. 10 a) 590 cross section SEM Image b) Statistics analysis of 590 with <d>=134nm, <h>=2.82 μm, <P.L.>=264.8nm and <Density>=3.4 x10^8 $\frac{NW's}{cm^2}$.

For 591 sample:

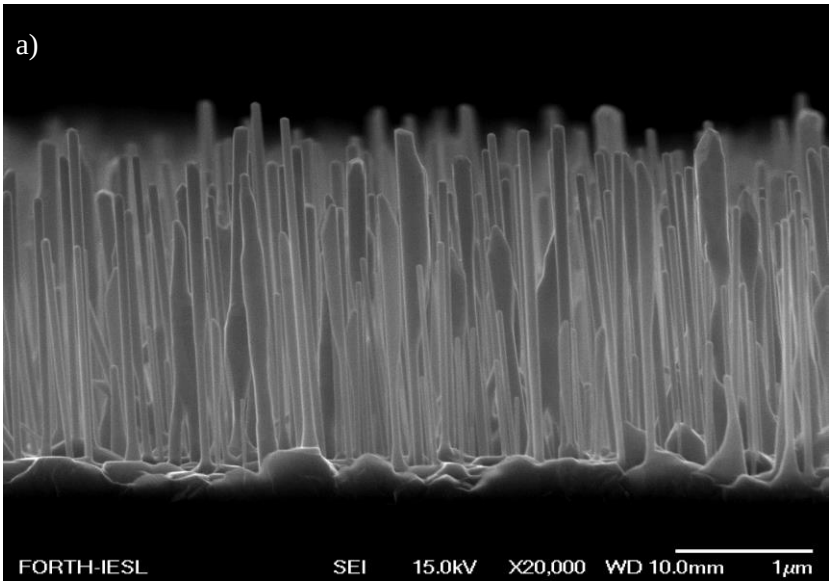

b)

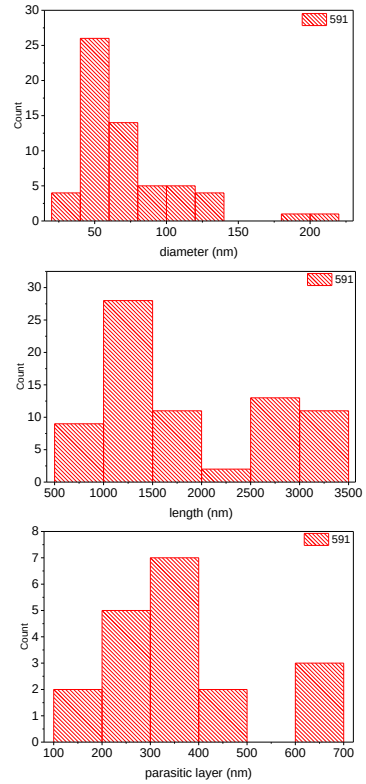

Figure 4. 11 a) *591 cross section SEM Image b) Statistics analysis of 591 with <d>=72nm, <h>=2 μm, <P.L.>=362.6nm and <Density>=5.2 x10*^{8} $\frac{NW's}{cm^2}$.

Sample	<Diameter> (nm)	<Height> (μm)	<Parasitic Layer> (nm)	<Density> $\frac{NW's}{cm^2}$
438	128	3.5	369.5	3 *x10*^{8}
439	42	3.2	425.7	3 *x10*^{8}
586	122.3	2.88	279.5	2.8 *x10*^{8}
590	134	2.82	264.8	3.4 *x10*^{8}
591	72	2	362.6	5.2 *x10*^{8}

Table 2. Summarizing the statistical results from SEM images.

Photoluminescence Measurements

For the optical characterization, photoluminescence spectroscopy was used for each sample at the same conditions. For the excitation was used a laser at 325nm and the samples were placed in the cryostat under vacuum.

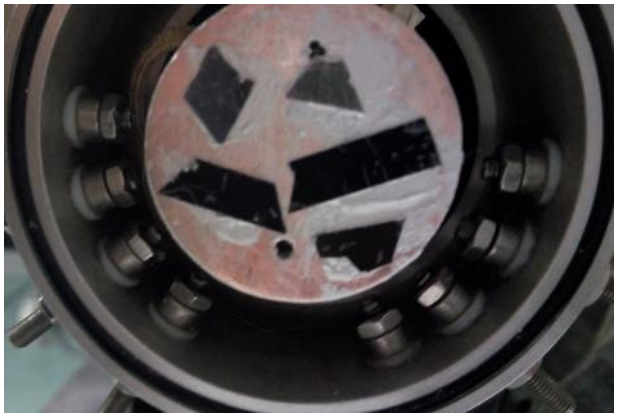

Figure 4. 12 Samples in the cryostat before measurement (438, 439, 586, 590 and 591 from top left clockwise).

The incident light from the laser is focused by lens on the samples while the emitted light is focused on the entrance slit of the monochromator where is analyzed. In front of the slit is placed a UV 350nm filter to discard scattered laser from the spectra. Before the samples a suitable neutral density filter is placed, which decreases the power of the incident beam by an order of magnitude (ND1) and the incident power to the samples is ~ 4mW.

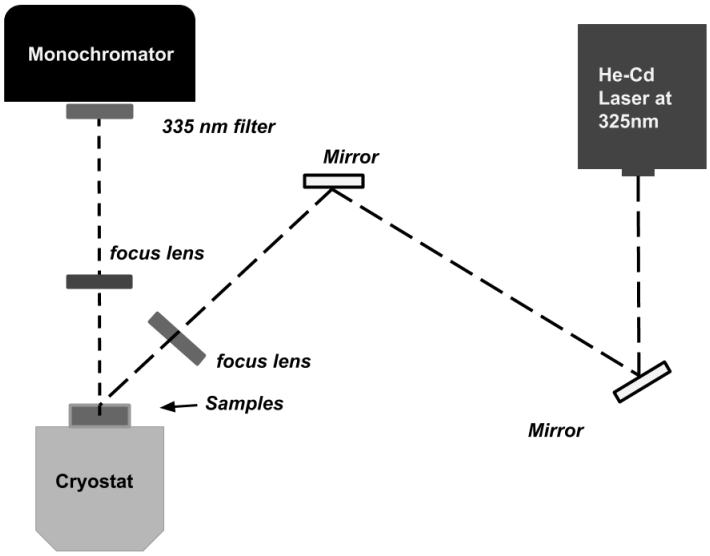

Figure 4. 13 Animation of the experimental PL set up.

To apprehend the optical properties of the samples, PL measurements versus Temperature took place. The results are presented in figure 4.14. The PL intensities, though in arbitrary units, can be compared between samples.

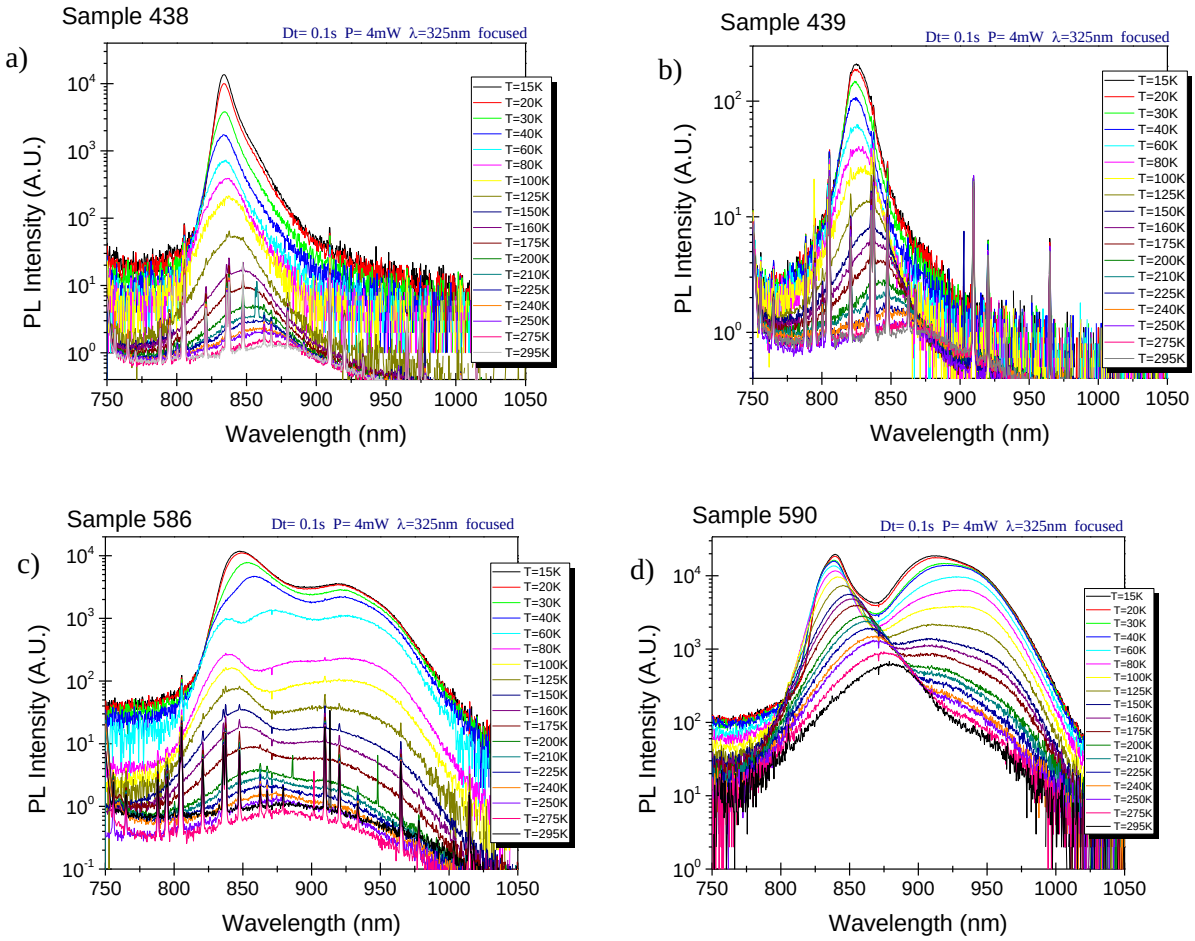

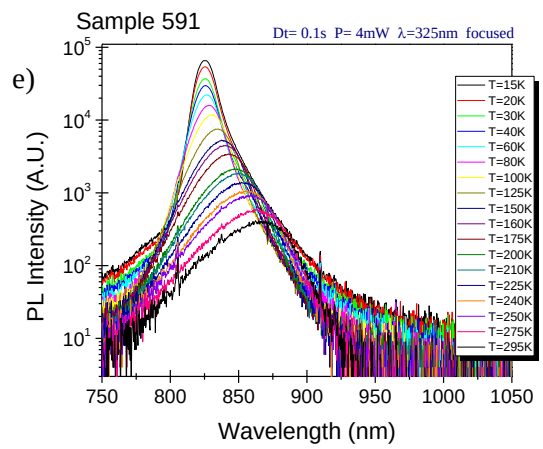

Figure 4. 14 a) From the temperature dependent PL spectra, we observe the main peak of sample 438 at 833nm for T=15K, which is shifted to 872nm for T=295K, with a simultaneous intensity drop by a factor of ~10^4. An additional shoulder appears with temperature at ~823nm. b) The main peak of 439 sample is at 825nm (T=15K) which is shifted to 875nm (T=295K) with intensity drop by a factor of ~200. c) Sample 586: the main transitions are at 846 and 922nm (T=15K) with a temperature drop from low to room temperature of ~10^4. d) Sample 590: the main transitions are again at 846 and 922nm (T=15K) but the intensity drop is now only a factor of ~30. e) Sample 591: the main transition is at 825nm (T=15K) and it is shifted to 872nm (T=295K) with the intensity drop of ~200.

As we observe from the PL diagrams at 15K, the main peak of the GaAs/p^+ GaAs NW samples (439 and 591) are at 825nm (~1.502eV). This peak could possibly be attributed to an electron-

acceptor transition, considering the high doping level in the shell. The intensity of 591 is two orders of magnitude higher than 439, as a consequence of the thicker NW diameter and the AlGaAs passivation layer in this sample. Somewhat unexpectedly, however, the intensity drop with temperature in these two samples is very similar, suggesting that the non-radiative mechanism in these samples is not only related to surface recombination. Further studies are needed to clarify this point.

Regarding the GaAs/p^+ InGaAs NW samples (438, 586, 590) the following remarks apply for the low T spectra. In sample 438, there is one main PL peak at 833nm, while in samples 586 and 590 we observe two main peaks, one in the 840-845nm range and one centered around 910-920nm. Based on previous work on similar core-shell NWs (Nanoscale Research Letters by Moratis et al.), the high energy peak in samples 586 and 590 can be attributed to emission from the nanowire InGaAs tips while the lower energy peak from localized states in the InGaAs shell. With increasing temperature, an additional high energy shoulder appears on all samples. In sample 438, the shoulder is at 825nm, in sample 586 at 833nmm while in sample 590 at 830nm. The origin of this shoulder is not certain at the moment, but a likely hypothesis is emission from the tensile-strained GaAs core, which is increasingly populated with increasing temperature. From its overall spectral behavior, sample 438 seems to contain less In in the shell, compared to samples 586 and 590. Interestingly, the localized emission in the above 900nm spectral range loses intensity faster with temperature. The intensity drop with temperature is much weaker in sample 590, most likely due to the efficient passivation in this sample by its relatively thick AlGaAs shell.

Nanowire Solar Cells

After optical and structural characterization of the nanowire samples, devices based on these samples are fabricated in order to study their performance.

The first set of devices are based on 438 and 439 samples. After nanowire's growth, BCB deposition is necessary to insulate electrically the top metal contact from the conducting substrate. In order to exhume the top of nanowires, the BCB planarization is etched back lower than the NW tips. After that process, Ti is deposited with rf-sputtering technique for more efficient adsorption of the Transparent Conducting Oxide (TCO). In these samples, as TCO is used Indium Tin Oxide (ITO) which is deposited with rf-sputtering as the p^+ top contact. For back contact Au is evaporated with e-beam technique.

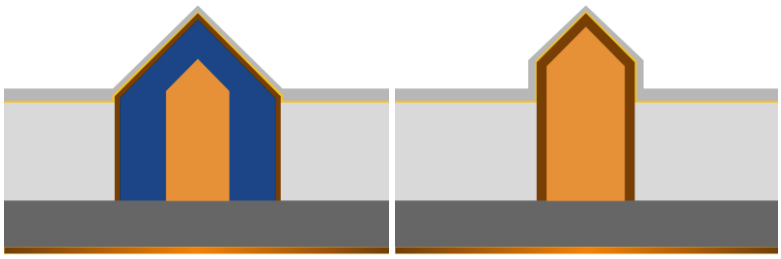

Figure 1. 438 and 439 samples after BCB etching

A second set of 3 samples based on 586, 590 and 591 Nanowire samples (586C, 590C, 591B) were fabricated with e-beam evaporated Ti/Au back contact, BCB planarization etched back to NW tips, and pulsed laser deposited (PLD) ITO top contact. Prior to ITO PLD deposition, thin Kapton tape

strips were used to form a grid mask on the sample to create multiple large-area devices. The samples were etched in dilute ammonia solution to remove native oxide before loading into the PLD chamber.

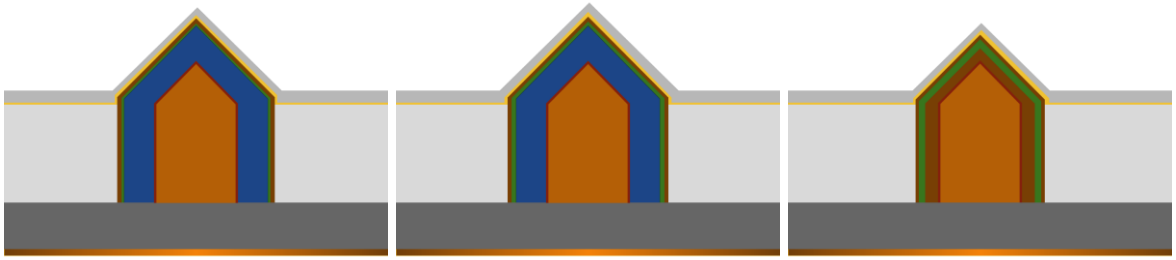

Figure 2. 586C, 590C and 591B samples after BCB etching

The final set of samples is again on 586, 590 and 591 NW samples (586A/B, 590A/B, 591A) complements the previous set (586C, 590C, 591B), by having the BCB planarization layer etched down by a further 400-500 nm to increase the density of the exposed NW tips. These samples share the same Ti/Au back contact and hard-cured BCB layer processing as the previous set. ITO top contact was deposited by pulsed laser deposition (PLD) on the samples after patterning with mesa mask windows. Lift off was successful with a brief (1-2 s) sonication.

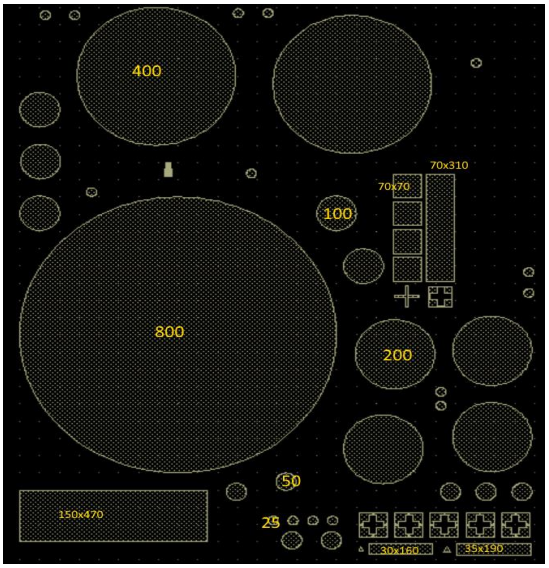

Figure 4. 15 The mask contains the following patterns: a) Circles with diameters: 800, 400, 200, 100, 50, 25 μm, b) Squares: 70μm×70 μm and c) Rectangles: 70 μm×310 μm,

SEM Analysis of Nanowire Solar Cells

After BCB etching it is important to study the surface structure of the devices. One basic parameter which is important to study is the density of the exposed Nanowires, as only these nanowires are active for the device performance. To export information about the density of the exposed nanowires SEM pictures were taken (fig. 4.16).

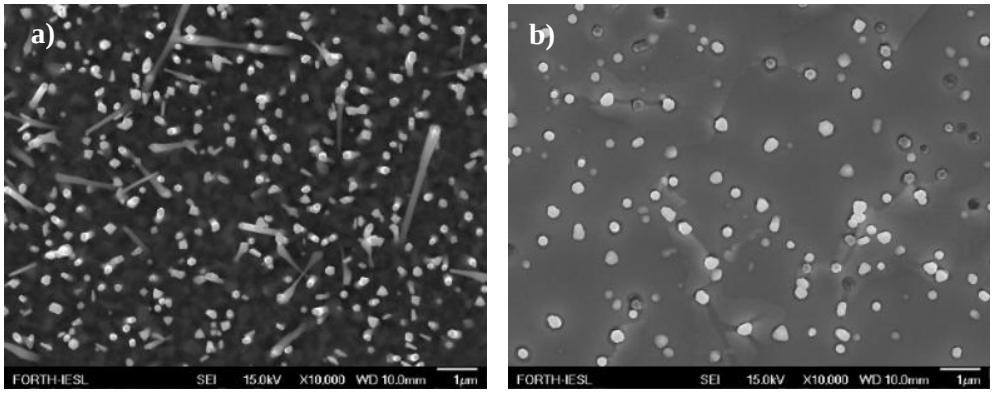

Figure 4. 16 a) SEM Images of 586A as grown and b) following BCB etching and ITO metallization.

For each sample, multiple areas were formed in order to study the devices performance and uniformity. The samples with numbered diodes are shown below:

Figure 4. 17:

a) 438 and b) 439 nanowire devices with a density of the exposed NWs ~ $5{\cdot}10^7$ NW's/cm² respectively

c) 586C with ~$3.7{\cdot}10^7$ NW's/cm²,

d)590C with ~$8.4{\cdot}10^7$NW's/cm² ,

e)591B with ~$2.6{\cdot}10^7$NW's/cm² ,

f)586A with ~$1.8{\cdot}10^8$NW's/cm² ,

g)586B with ~$1.16{\cdot}10^8$NW's/cm²,

h)590A with ~$1{\cdot}10^8$NW's/cm²,

i) 590B with ~$3.73{\cdot}10^8$NW's/cm² and

j)591A with average density of the exposed NWs ~$7.76{\cdot}10^7$NW's/cm²

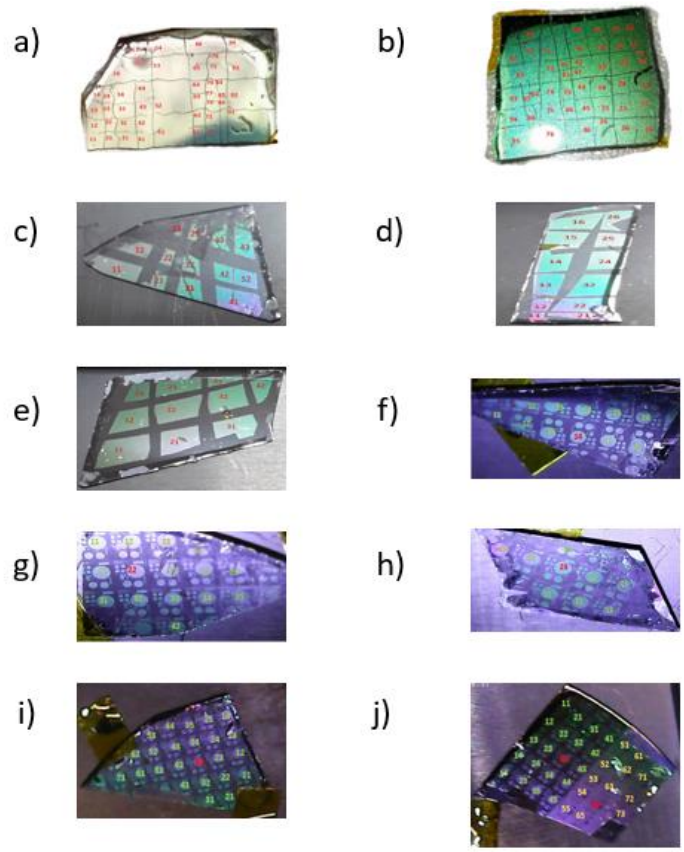

I-V Analysis of Nanowire Solar Cells

The performance of solar cell devices can be described from the efficiency of each cell to convert the incident sunlight into current. Each solar cell follows the photovoltaic effect where carriers are generated from the incident light, separated and collected from the electrodes. To examine the cell's performance, I-V measurements should take place. For these experiments, a suitable experimental set up is necessary.

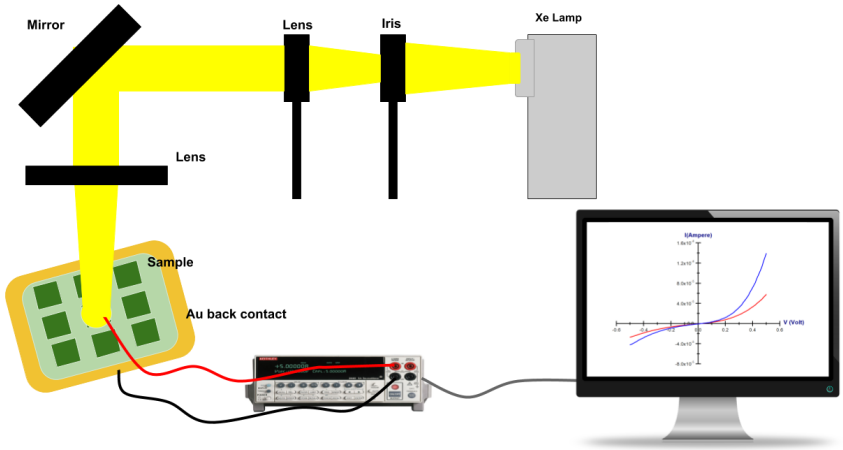

Figure 4. 18 Experimental Set up for I-V measurements.

In the picture above, there is the cartoon representation of the experimental setup for the IV measurements. The beam from the light source (Xe lamp) arrives to an iris to reduce its intensity. The light is collimated by a lens and is directed by a mirror toward the sample. Between the mirror and the sample is placed another condenser lens which focuses the light on the desirable diode. The sample is placed on an gold-metallized surface as back contact. The two contacts are connected to multimeter (KETHLEY 2000) which is connected with a computer in order to convert the signal from the amperometer to I-V curves.

To export the desirable results, I-V measurements were taken when the diodes were illuminated (photo I-V) and when they were not (dark I-V).

Dark I-V analysis

For the dark I-V, voltage is applied to the circuit and the characteristic I-V curves are collected. The main extracted parameters from dark I-V analysis are the ideality factor (η) of the device which is a measure of how closely to an ideal diode is the measured diode, the series (R_{series}) resistance which is a parameter reducing the Fill Factor of the cell and the shunt (R_{shunt}) resistance which contributes to the power losses of the device.

The measured I-V plot of 586A for a circular pattern with 200 μm diameter after annealing at 300°C for 30min is presented below. As it is expected the I-V curve has nonlinear characteristics. The current equation for dark I-V is given as:

$$I = I_0 \cdot (e^{\frac{q \cdot V}{\eta \cdot k_B \cdot T}} - 1) \qquad (33)$$

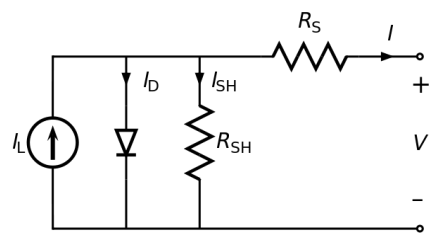

Figure 4. 19 Conventional equivalent circuit representation of Solar Cells

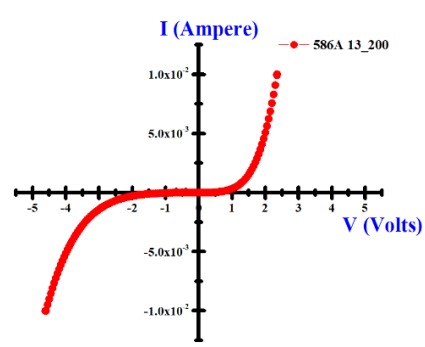

Figure 4. 20 Dark I-V of 586A sample.

For applied voltage V > 50-100mV the last term -1 of the equation can be ignored and the equation changes to:

$$I = I_0 \cdot e^{\frac{q \cdot V}{\eta \cdot k_B \cdot T}} \qquad (34)$$

where Io is the dark saturation current, q is the electron charge, k_B is Boltzmann constant, T is the absolute temperature (we assume here T=295K), I and V are the measured current and voltage respectively and η is the ideality factor of the device.

To approximate the ideality factor of the device we should Log both sides of the equation

$$ln(I) = ln(I_0) + \frac{q}{\eta \cdot k_B \cdot T} \cdot V \qquad (35)$$

It is clear that if we plot the diagram with ln(I) at y-axis and V at x-axis the slope will be equal to $\frac{q}{\eta \cdot k_B \cdot T}$ while the interception will represent the ln(Io). The value of ideality factor in real cells varies with the voltage, as η is a parameter which reflects the recombination effects in the device. So, for different values of voltage, we can assume that the recombination mechanism changes. Thus, we can plot the ideality factor as a function of the applied voltage. If the ideality factor is given as a constant value, the corresponding voltage value should be determined. To determine η and I_0, we fit linearly the semi log I-V curve at low voltages as shown in figure 4.21.

The linear fitting equation from the diagram is given as:

$$y = 18.3217 \cdot x - 16.414 \qquad (36)$$

where 18.3217 leads to η=2.147 and -16.414 to Io=7.438·10^{-8} A. The next parameter that we are interested in, is the value of R_{series}. To extract the series resistance we calculate the difference between the expected values of the fitted equation and the experimental values at high voltage (fig.4.22), where R_{series} is directly proportional to ΔV (R_{series} = ΔV/I).

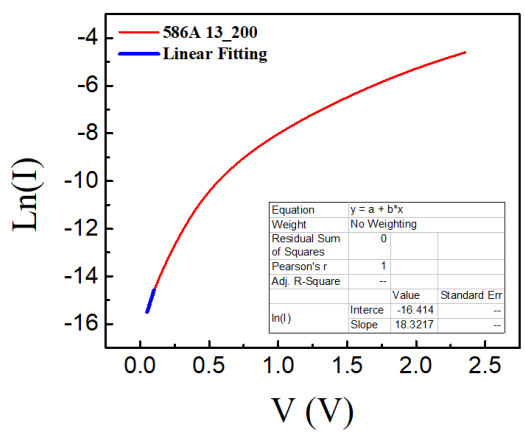

Figure 4. 21 Plotted ln(I)-V curve in order to extract ideality factor and Io values at low voltage.

As we observe in figure 4.21, at high bias the slope from the curve decreases. This drop of the slope testifies the domination of R_{series}. When the current is getting larger the power losses are significant and the voltage of the junction is given as a function of the applied voltage V_a , the current and the series resistance as:

$$V_j = V_a - IR_{series} \qquad (37)$$

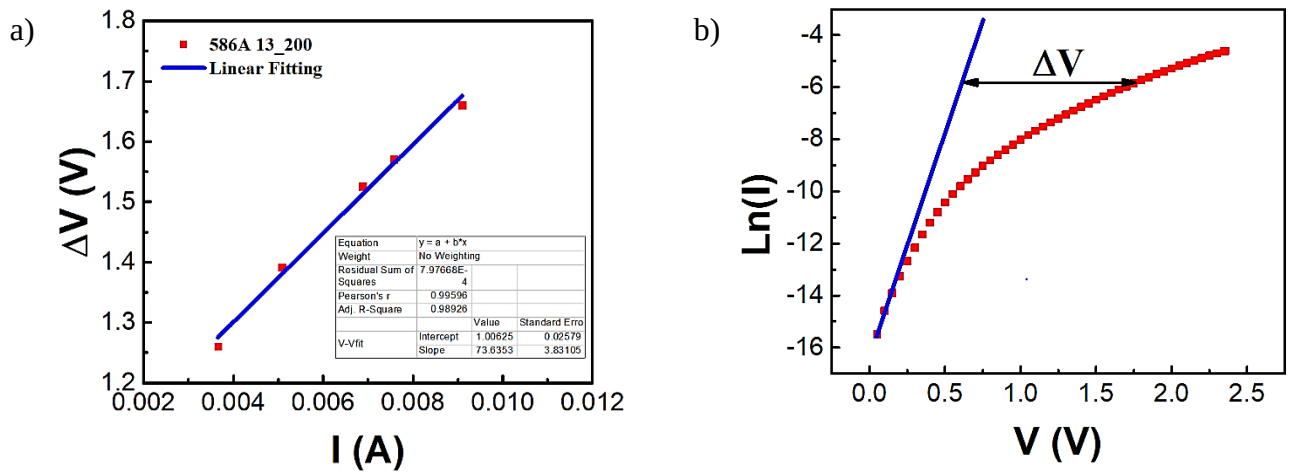

Figure 4. 22 a) calculation of ΔV vs I from Ln(I)-V plot b) ΔV-I plot with linear fitting.

From the slope of the ΔV-I diagram, the specific value of R_{series}= 73.64 Ω is obtained for the diode at hand. The last parameter which we can export is R_{shunt} which dominates at low voltage. The slope from the linear region of an I-V curve gives us the R_{shunt} value. The extracted value of R_{shunt}=283.8KΩ. Evidently, from the dark I-V curve, we can extract basic quantities for the device characterization. The shunt current is observed to have non-linear dependence on voltage and a space-charge-limited (SCL) mechanism has been proposed to explain the shunt behavior.

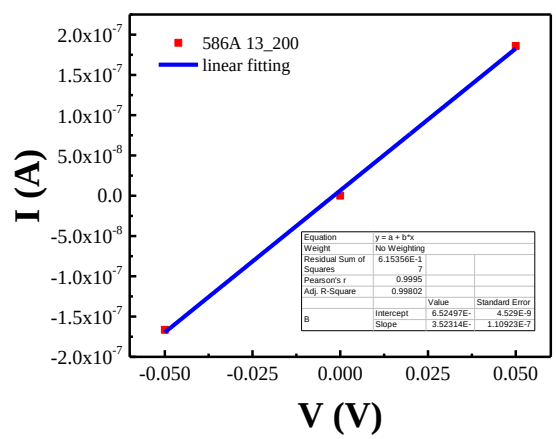

Figure 4. 23 Linear Fitting to I-V curve at low voltage where R_{shunt} dominates.

The SCL model for non-ohmic parasitic shunts yields the following parameterized expression for the shunt current:

$$I_{shunt} = G_{0,shunt} \cdot V + I_{0,shunt} \cdot V^{n_{shunt}} \tag{38}$$

where, $I_{0,shunt}$ is the SCL shunt current magnitude, n_{shunt} is the shunt current power exponent and $G_{0,shunt}$ is the constant conductance component at low biases. This conductance component is to account for linear conduction of shunt at low bias values (~0.1-0.2 V). Similarly, a parameterized Shockley equation for diode can used to fit the diode current, including the series resistance as,

$$I_D = I_0 \cdot (e^{\frac{V - I_D \cdot R_{series}}{n \cdot k_B \cdot T/q}} - 1) \tag{39}$$

where, I_0 is the diode saturation current, n is the diode ideality factor and R_{series} is the series resistance. It is important for reliable analysis the points that will be selected to be representative. A tool which can be found in the web and analyzes the dark I-V curve and extract's the diode and shunt parameters is PV analyzer. This tool utilizes the symmetry of shunt current to separate the shunt and diode current components and then uses separate equations to fit the two current components. This separation and fitting method yield parameter values which are free from fluctuations due to parasitic and can be related to physical processes in the device. The tool can also analyze multiple IV data at once, and all the data as well as fit parameters can be downloaded as text files for further analysis. After using PV analyzer, we extracted the diagrams below:

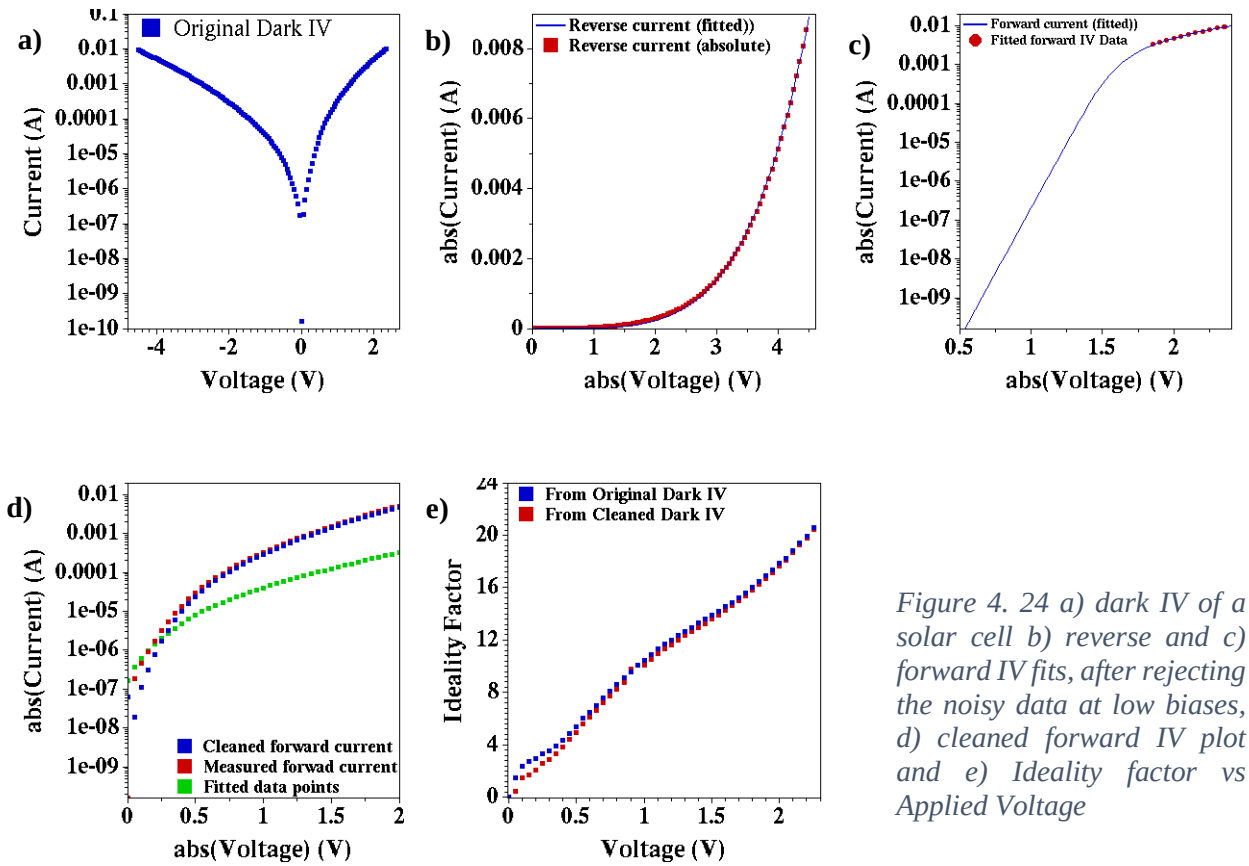

Figure 4. 24 a) dark IV of a solar cell b) reverse and c) forward IV fits, after rejecting the noisy data at low biases, d) cleaned forward IV plot and e) Ideality factor vs Applied Voltage

In figure 4.24 a) is presented the original dark current as a function of the voltage while in figure 4.24 b) and c) are presented the plots for the forward and reverse IV data and the fits obtained respectively. For the forward IV, the noisy data at the low bias are rejected. The tool does this iteratively by neglecting 1 noisy data point at a time until a good fit is obtained. The reverse current is plotted and compared with shunt current parameters. For the cleaning of the dark I-V current (fig. 4.24 d) was used the equation:

$$I_{D,fw}(V) = I_{fw}(V) - |I_{rev}(V)| \tag{40}$$

For the ideality factor calculation versus voltage (Fig. 26 b) was used the equation:

$$\eta(V) = \frac{qI}{k_B T} \left(\frac{dI}{dV}\right)^{-1} \tag{41}$$

Evidently, the PV analyzer and the conventional dark I-V analysis extract the same results with minor deviations occurred by minor errors at the analysis (table 2).

PV analyzer results	*Conventional method*
n = 2.51	n = 2.15
R_s = 71.55 Ω	R_s = 73.64 Ω
R_{sh}=263.43KΩ	R_{sh}=283.8 KΩ

Table 3. Extracted parameter comparing SCL and conventional method

Using the conventional method, the same parameters are extracted for the rest samples as presented in figure 4.25 and 4.26.

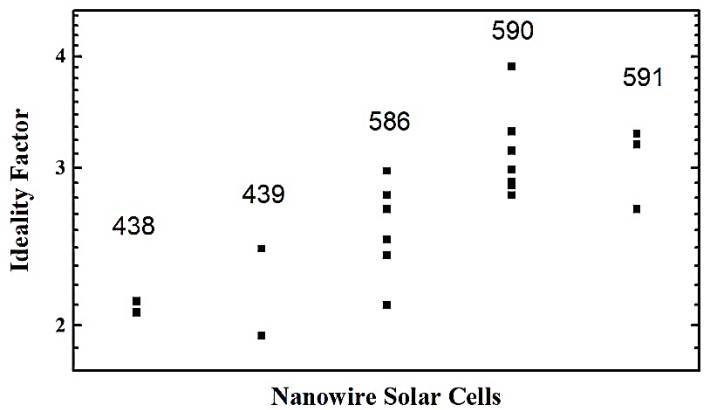

Figure 4. 25 Ideality Factor of Nanowire Samples at low voltage .

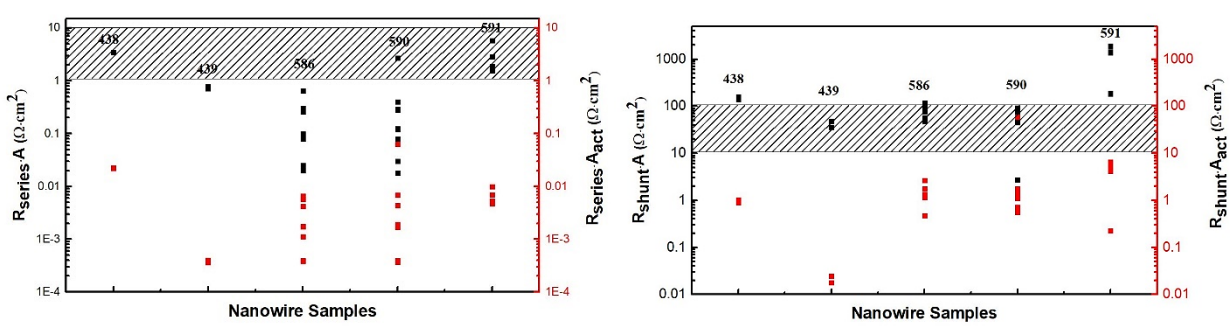

Figure 4. 26 Series Resistance multiplied with the diode and effective area for the nanowire samples and Series Resistance multiplied with the diode and effective area for the nanowire samples.

The series resistance depends on the metal/semiconductor contact resistance, on carrier movement within semiconductor and on the metal resistance, where the last term is typically small in our case. In addition, the shunt resistance represents an alternative path for the carriers. To a better comparison of the diodes, the extracted values were multiplied with the area of the diode and the

‘’effective’’ area which represents the area of the nanowires in 2D for each diode area (A and Aactive respectively). In any case A>Active for all samples. In our system, it is not clear enough which area should normalize the resistance, as the parasitic layers tend to increase the effective area beyond the 2D area occupied by the NWs, as we can see in figure 4.27.

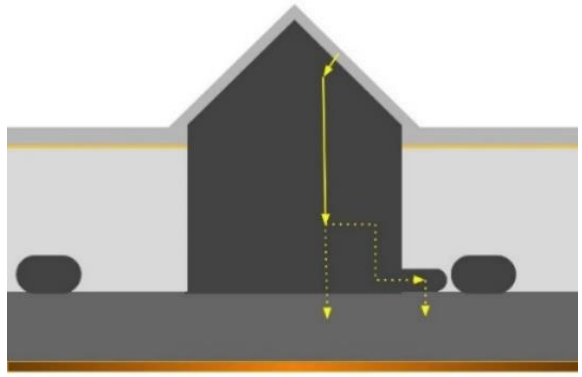

Figure 4. 27 Possible free carriers' path.

In the rest, both areas were used to normalize the resistance values (fig. 4.26). Using the PV education simulator for a thin film solar cell, we realize that R_{series} becomes visible in the I-V when is higher than 1Ωcm^2 while when R_{series} ~ 10Ωcm^2 the correction is important. Similarly, the shunt resistance becomes visible for values lower than 100 Ωcm^2 with important correction to the I-V when R_{shunt} is lower than ~10Ωcm^2.

By inspection of the graph, all the red points in the shunt resistance are below the shaded area implying that we have serious “shunt resistance” problems. On the other hand, the same holds for series resistance which seems to suggest that we have no series resistance problems. A thought of the results is that the main conduction channel may be through the 2D parasitic layer.

Comparing the series resistance values before and after annealing of the ITO contact, they seem not to be affected by the annealing step.

When we multiply the resistance values with the area we observe that series resistance does not scale with diode area in 586 and 590. This is not true in 591. This result is not understood at the moment. On the other hand, R_{shunt} scales with area, for all samples.

The series resistance of 586 and 590 are generally lower compared to 438. A first thought is that this could be attributed to the p-doping of the core. The shunt resistance for the same samples is similar to 438. This implies that the AlAs interlayer and AlGaAs passivation layer did not affect parasitic paths.

If we compare 439 and 591 samples we observe that both series and shunt resistance are improved for 591 sample (lower series and higher shunt resistance than 439). So, staying with these results alone one would be tempted to say that the changes in the sample design have improved things. Considering however the results on 438, 586 and 590, this conclusion loses certitude.

Photo I-V analysis

By illuminating the solar cell diode, with the same set up as before we can plot the photo I-V curves of the device and we can extract important parameters such as the short circuit current (I_{sc}), the open circuit voltage (V_{oc}), the fill factor (FF) and the device's efficiency (n). All the extracted parameters are important to characterize the device. For the analysis, we use the very same diode as in figures 4.20-4.22, and the photo IV plot is presented in figure 4.28.

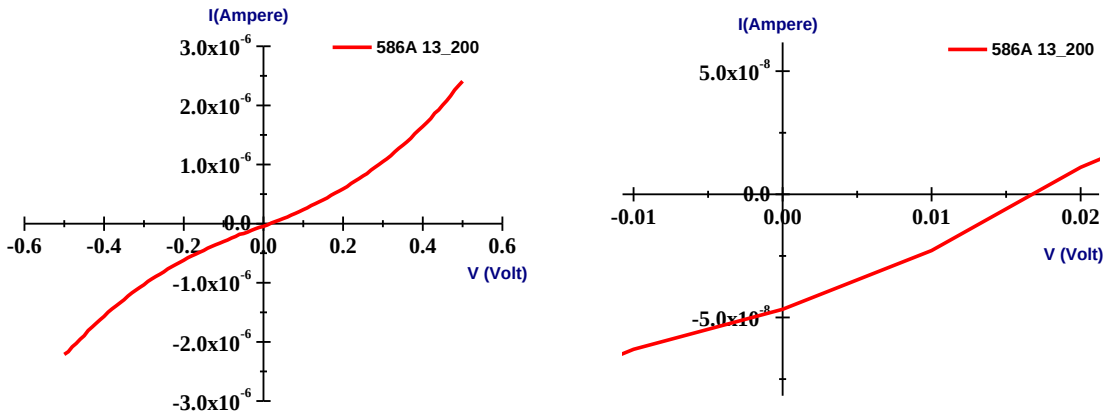

Figure 4. 28 Photo I-V curve (left) and zoom in to interception points (right)

The photo IV curve is a superposition of the I-V curve in the dark with the light generated current. The equation which describes this superposition of the current is given:

$$I == I_L - I_0\, e^{\frac{q(V+IR_s)}{k_B T}} - \frac{V + IR_s}{R_{shunt}} \tag{42}$$

where I_L is the light generated current. It is clear from figure 4.28 that V_{oc}=0.0167 V and I_{sc}=4.6·10^{-8} A. To calculate FF we use the empirical equation:

$$FF = \frac{\upsilon_{oc} - \ln(\upsilon_{oc} + 0.72)}{\upsilon_{oc} + 1}, \tag{43}$$

where,

$$\upsilon_{oc} = \frac{q}{\eta \cdot k_B \cdot T} \cdot V_{oc} \tag{44}$$

The calculated value of FF=0.2214 or 22.14% in this example. The last important parameter is the efficiency of the diode which is determined as the fraction of the incident power converting to electricity and is given as:

$$n = \frac{P_{max}}{P_{in}} \tag{45}$$

where assuming that the incident power was 1sun (100mW/cm^2) and the illuminated area was 3.142·10^{-4}cm^2, we can easy calculate that $P_{in} = 0.3142 \cdot 10^{-4} W$. The equation for P_{max} is given as:

$$P_{max} = V_{oc} \cdot I_{sc} \cdot FF \quad (46)$$

Calculating the $P_{out} = 1.75 \cdot 10^{-10} W$, the respective value of efficiency is $n = 0.0006\%$.

The low efficiency of the diodes could be attributed to the existence of series and shunt resistance. The main impact of both R_{series} and R_{shunt} resistance are significant power losses. More specifically, series resistance reduces the fill factor while at high values reduces the short circuit current. Significant power losses are provided with the shunt resistance, which at low values provides an alternative path for the carriers. The main impact for shunt resistance is the reduction of open circuit voltage. So according to eq.11 the P_{max} value is reduced and the diode efficiency drops to low values as expected.

For a thorough understanding of the sample's behavior, the corresponding measurements are presented (fig. 4.29 - 4.30).

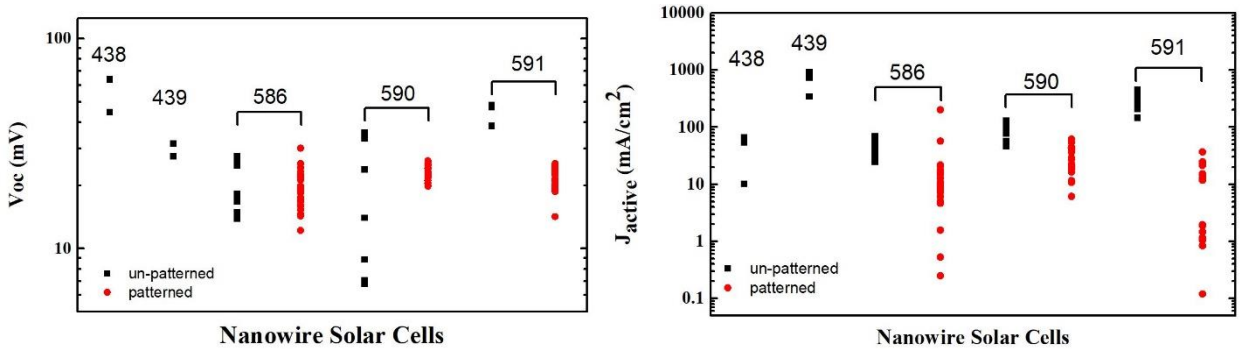

Figure 4. 29 Open Circuit voltage (left) and active current (right) of nanwire samples.

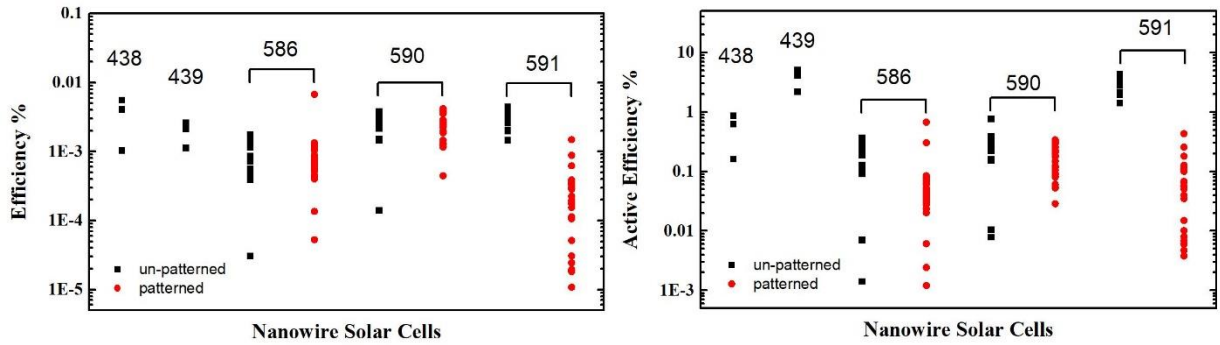

Figure 4. 30 Efficiency (left) and active efficiency (right) of nanowire samples.

According to figure 4.29 we observe that V_{oc} values are very low. This is typically an outcome of shunt resistance problems, already pointed out in the analysis of dark I-V data.

If we normalize the current by the diode area we observe that current density is very low but if we normalize by the diode A_{active} the current density values are between one and several hundreds of mA/cm^2. Considering that in a planar thin film solar cell, the current density is limited by the solar irradiance and gives values of 25-30 mA/cm^2, obtaining in our case values that exceed this value is probably an artifact of normalizing by the NW cross-sectional area. The latter is probably an

exaggeration considering that the NW diameter is strongly subwavelength and that incident light's wavelength covers several NWs simultaneously. The obtained efficiency values are very small. However these values are not fair as our NW arrays are quiet empty. On the other hand, if we normalize by the active area, we obtain efficiencies up to 5% in some cases, which as commented before is probably an overestimate.

The un-patterned diodes give systematically somewhat better results compared to the patterned diodes (third set of NW samples). This is visible on all samples but is more pronounced in the case of 591.

Comparing the samples, we could say that 590 is no better than 586, while 586 and 590 are worse than 438. The GaAs nanowires gave longer active efficiency compared to GaAs/InGaAs samples (fig. 4.30).

Overall, we have analyzed several NW diodes fabricated from different samples. The diodes exhibit low PV efficiencies as a result of strong shunt resistance effects and low NW densities. A likely parasitic path is through the 2D/Si p-n interface in between the NWs. Efforts to limit this path using the AlAs interlayer between core and shell, to render the 2D layer more resistive, did not seem to work. The AlGaAs passivation layer and p-type doping of the core did not affect PV characteristics either.

EQE and Responsivity measurements

Responsivity is a measure how much of the incident optical power is converted to photocurrent. It is important to study the responsivity of the material as it will be clear at which wavelengths the semiconductor converts the maximum number of photons into current. The main parameter is the bandgap of the semiconductor. If the energy of the incident photon is lower than the energy gap of the semiconductor, the interaction between the light and the material is weak, the photon passes through the semiconductor and no carriers are generated. If the energy is higher than the bandgap, the photon is strongly absorbed and the electron is found at excited states of the conduction. In this case the excess energy is wasted as the electron (holes) thermalizes to the bottom of the conduction valence band. In this case the photon is absorbed efficiently and a pair of electron-hole is generated. The equation to calculate the responsivity is given as:

$$Responsivity(\frac{A}{W}) = \frac{j_{photo}(\frac{A}{cm^2})}{P_{in}(\frac{W}{cm^2})} \tag{47}$$

External Quantum Efficiency is one of the most important parameters for a solar cell. EQE is determined as the fraction of number of carriers collected at the contacts to the number of incident photons. Ideally, an EQE plot has a square shape with highest value close to unity but for most solar cells is reduced due to recombination effects.

$$EQE = \frac{\#n_{out}}{\#n_{in}} = Responsivity \cdot \frac{1239.8}{\lambda(nm)} \tag{48}$$

The experimental set up for these measurements is presented below:

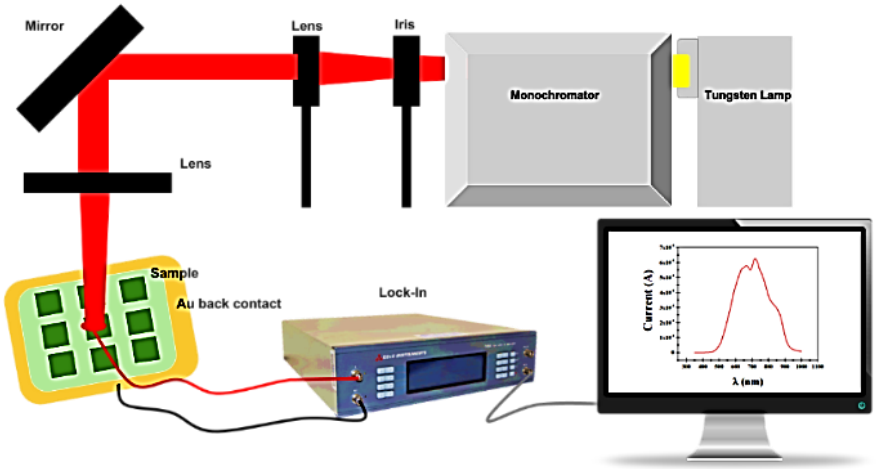

Figure 4. 31 Cartoon representation of EQE/Responsivity measurements.

For the measurements a light source (tungsten lamp) is placed in front of the monochromator in order to analyze the light to different wavelengths. The light from the source arrives to an iris to reduce the intensity. Next, the light incident to a condenser lens is collimated to a mirror in order to be directed toward the sample. Between the mirror and the sample is placed another condenser which focuses the light on the diode. The sample is placed on an Au surface as back contact. The two contacts are connected to a Lock-In device to increase the signal. The lock in is connected with a computer in order to extract the results.

During the measurements photocurrent and power versus wavelength are measured. After analysis and using equations 47 and 48 we extract Responsivity and EQE plots.

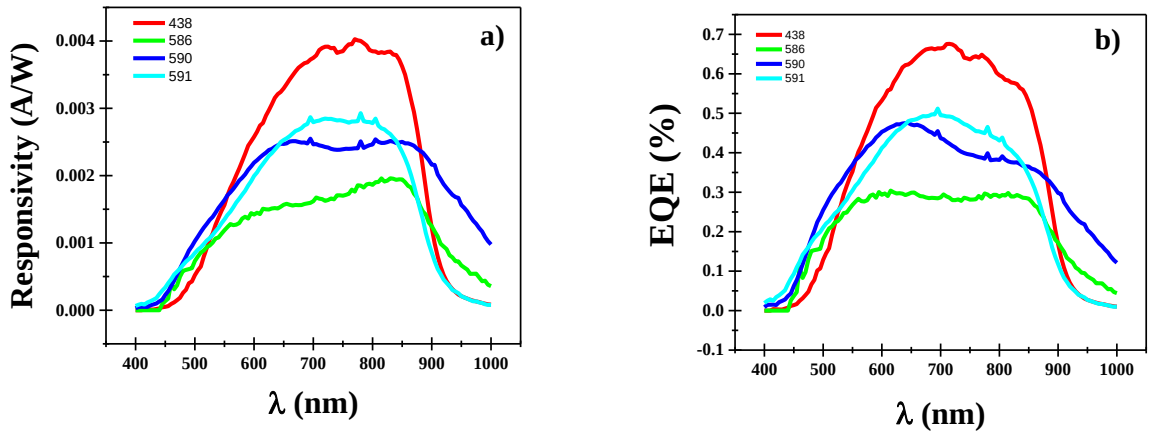

Figure 4. 32 a) Responsivity and b) EQE (right) plots for 438, 586, 590 and 591 samples.

We observe the sharp onset of absorption at or near the GaAs bandgap. This excludes the possibility that the photocurrent is due to absorption in the Si substrate and clearly indicates absorption process at the GaAs NW structure.

The curves of the InGaAs shell containing NWs shows extended absorption in the sample >900nm spectral region, in agreement with absorption in the InGaAs layer. This is more pronounced in 590 compared to 586 and to 438. In fact, 438 is not very different in this respect compared to the pure GaAs NW diodes of 591, confirming our assertion in the PL analysis that 438 has lower In content (lower than nominal).

The overall EQE values remain smaller than 1% throughout in line with the low PV efficiencies of these NW solar cells.

Conclusions

In this thesis, GaAs-InGaAs core-shell nanowire diode samples are investigated in view of photovoltaic applications. Five different nanowire heterostructures are grown by MBE on an n^+Si(111) substrate via Ga-assisted VLS method. The as-grown nanowires have diameters between ~ 40-135nm, height ~ 2-3.5μm and densities ~10^8NWs/cm^2. The optical properties of the different nanowire samples (438, 439, 586, 590 and 591) are measured with temperature dependent photoluminescence in order to investigate the excitonic transitions and efficient passivation of shell. The p doped GaAs core with p^+ InGaAs shell (590 sample) nanowire array seems to present the most efficient passivation behavior. The electrical properties of SC devices based on the NW samples are investigated. The characteristic I-Vs are used to extract the desirable values. The ideality factor of all samples converge between 2-3, which is in agreement with Farell et al. [42] who reports that the vast majority of NW-based p-n Junction is higher than 2. The series resistance multiplying with the diode area presents values between 10^{-2}-10 Ωcm^2, while multiplied with the active area of the nanowires present values between 10^{-4}-10^{-1} Ωcm^2. The shunt resistance multiplied with diode area and active area present values between 10-1000 Ωcm^2 and 0.01-10 Ωcm^2, respectively. Comparing these values with previews results (chapter 4), we can say that our system seems to have serious shunt resistance problems which affect the final performance of the devices. These problems could be attributed to the parasitic layers on the interface with the substrate and could explain the low values of photovoltaic efficiencies.

Supplementary Tables

SAMPLE	ITO deposition	Contact anneal. temp. (°C)	BCB etching	A (cm²)	Aactive	Ideality factor	Rs (Ω)	Rshunt (KΩ)	Rs·A (Ω·cm²)	Rshunt*A (kΩ·cm²)	Rs·Aact (Ω·cm²)	Rshunt*Aact (kΩ·cm²)
438_51	RF sputtering	350		0.0445	$2.86\cdot10^{-4}$	2.13	78.4	3.6	3.49	0.16	0.0224	0.00103
438_52	RF sputtering	350		0.0426	$2.74\cdot10^{-4}$	2.07	81.7	3.3	3.48	0.14	0.0224	0.00090
439_34	RF sputtering	350		0.0199	$0.10\cdot10^{-4}$	2.44	39.7	1.8	0.79	0.04	0.0004	0.00002
439_44	RF sputtering	350		0.0150	$0.07\cdot10^{-4}$	1.95	48.1	3.2	0.72	0.05	0.0004	0.00002
586A_13 (800)	PLD	300	deep	0.0050	$1.09\cdot10^{-4}$	2.80	51.8	11.6	0.26	0.06	0.0057	0.00127
586A_13 (400)	“	300	deep	0.0013	$0.28\cdot10^{-4}$	2.50	62.7	94.4	0.08	0.12	0.0018	0.00264
586A_13 (200)	“	300	deep	0.0003	$0.06\cdot10^{-4}$	2.98	62.6	283.5	0.02	0.09	0.0004	0.00177
586B_22 (800)	“	No anneal	deep	0.0050	$0.71\cdot10^{-4}$	2.40	59.3	19.0	0.30	0.10	0.0042	0.00134
586B_22 (400)	“	No anneal	deep	0.0013	$0.15\cdot10^{-4}$	2.70	77.7	80.5	0.10	0.10	0.0011	0.00116
586B_22 (200)	“	No anneal	deep	0.0003	$0.05\cdot10^{-4}$	2.80	81.0	241.9	0.03	0.08	0.0004	0.00116
586C_22	“	300	shallow	0.0070	$0.30\cdot10^{-4}$	2.11	92.0	6.7	0.64	0.05	0.0028	0.00020
590A_11 (800)	“	300	deep	0.0050	$0.55\cdot10^{-4}$	2.99	79.4	12.9	0.40	0.07	0.0044	0.00071
590A_11 (400)	“	300	deep	0.0013	$0.19\cdot10^{-4}$	3.90	97.9	73.0	0.12	0.09	0.0019	0.00142
590A_11 (200)	“	300	deep	0.0003	$0.04\cdot10^{-4}$	3.30	96.4	144.0	0.03	0.05	0.0004	0.00056
590B_33 (800)	“	No anneal	deep	0.0050	$1.21\cdot10^{-4}$	2.80	56.6	14.8	0.29	0.07	0.0068	0.00178
590B_33 (400)	“	No anneal	deep	0.0013	$0.27\cdot10^{-4}$	2.90	62.8	50.8	0.08	0.06	0.0017	0.00137
590B_33 (200)	“	No anneal	deep	0.0003	$0.07\cdot10^{-4}$	2.87	57.2	162.3	0.02	0.05	0.0004	0.00111
590C_11	“	300	shallow	0.0140	$1.33\cdot10^{-4}$	3.14	192.5	181.2	2.70	2.54	0.0257	0.02415
591A_33 (800)	“	300	deep	0.0050	$0.14\cdot10^{-4}$	3.19	373.7	363.9	1.88	1.83	0.0053	0.00520
591A_33 (400)	“	300	deep	0.0013	$0.04\cdot10^{-4}$	2.70	1231.3	1098.8	1.55	1.38	0.0047	0.00420
591A_33 (200)	“	300	deep	0.0003	$0.01\cdot10^{-4}$	3.28	9173.8	5987.5	2.88	1.88	0.0099	0.00648
591B_11	“	300	shallow	0.0620	$0.74\cdot10^{-4}$	3.19	93.4	3.0	5.79	0.19	0.0070	0.00022

Table 4. Extracted parameters from dark I-V

438 diode	I_{sc} A	V_{oc} V	A_{active}/A %	j A/cm²	j_{active} A/cm²	FF	P_{out} W/cm²	n %	n_act %
350°C							P_{in}=0.1 W/cm²		
33	$0.09\cdot10^{-5}$	0.064	0.64	$0.67\cdot10^{-4}$	0.010	0.25	$1.05\cdot10^{-6}$	0.0011	*0.16*
51	$1.90\cdot10^{-5}$	0.045	0.64	$4.27\cdot10^{-4}$	0.066	0.21	$4.09\cdot10^{-6}$	0.0041	*0.64*
52	$1.50\cdot10^{-5}$	0.065	0.64	$3.52\cdot10^{-4}$	0.055	0.25	$5.64\cdot10^{-6}$	0.0056	*0.88*

Table 5. Extracted parameters from photo I-V for 438 sample

439 diode	I_{sc} A	V_{oc} V	A_{active}/A %	J A/cm^2	j_{active} A/cm^2	FF	P_{out} W/cm^2	n %	n_act %
350°C							P_{in}=0.1 W/cm^2		
34	$7.60\cdot10^{-6}$	0.028	$5.09\cdot10^{-2}$	$3.82\cdot10^{-4}$	0.75	0.20	$2.12\cdot10^{-6}$	0.0021	4.16
44	$7.10\cdot10^{-6}$	0.028	$5.09\cdot10^{-2}$	$4.73\cdot10^{-4}$	0.93	0.20	$2.63\cdot10^{-6}$	0.0026	5.18
66	$2.10\cdot10^{-6}$	0.032	$5.09\cdot10^{-2}$	$1.78\cdot10^{-4}$	0.35	0.20	$1.13\cdot10^{-6}$	0.0011	2.23

Table 6. Extracted parameters from photo I-V for 439 sample

586A diode	Diameter µm	I_{sc} A	V_{oc} V	A_{active}/A %	J A/cm^2	j_{active} A/cm^2	FF	P_{out} W/cm^2	n %	n_act %
No anneal								P_{in}=0.1 W/cm^2		
13	800	$5.80\cdot10^{-8}$	0.021	2.17	$1.15\cdot10^{-5}$	$5.31\cdot10^{-4}$	0.22	$5.29\cdot10^{-8}$	$5.29\cdot10^{-5}$	0.0024
	400	$3.00\cdot10^{-12}$	0.017	2.22	$2.39\cdot10^{-9}$	$1.07\cdot10^{-7}$	0.23	$9.26\cdot10^{-12}$	$9.26\cdot10^{-9}$	4.10^{-7}
	200	$1.00\cdot10^{-7}$	0.019	1.99	$3.18\cdot10^{-4}$	0.016	0.22	$1.34\cdot10^{-6}$	0.00134	0.0674
14	800	$9.30\cdot10^{-7}$	0.030	2.17	$1.85\cdot10^{-4}$	0.008	0.20	$1.13\cdot10^{-6}$	0.00113	0.052
	400	$2.40\cdot10^{-7}$	0.019	2.22	$1.91\cdot10^{-4}$	0.009	0.22	$7.90\cdot10^{-7}$	$7.90\cdot10^{-4}$	0.036
	200	$9.50\cdot10^{-8}$	0.015	1.99	$3.02\cdot\cdot10^{-4}$	0.015	0.24	$1.04\cdot10^{-6}$	0.00104	0.052
15	800	$9.00\cdot10^{-7}$	0.022	2.17	$1.79\cdot10^{-4}$	0.008	0.22	$7.81\cdot10^{-7}$	$7.80\cdot10^{-4}$	0.036
	400	$1.07\cdot10^{-6}$	0.025	2.22	$8.51\cdot10^{-4}$	0.038	0.21	$6.75\cdot10^{-6}$	0.00675	0.304
	200	$2.90\cdot10^{-8}$	0.020	1.99	$9.23\cdot10^{-5}$	0.005	0.22	$4.01\cdot10^{-7}$	$4.01\cdot10^{-4}$	0.020
12	400	$2.80\cdot10^{-7}$	0.023	2.22	$2.23\cdot10^{-4}$	0.010	0.21	$1.10\cdot10^{-6}$	0.0011	0.049
11	400	$7.00\cdot10^{-9}$	0.023	2.22	$5.57\cdot10^{-6}$	$2.51\cdot10^{-4}$	0.21	$2.68\cdot10^{-8}$	$2.68\cdot10^{-5}$	0.0012
300°C								P_{in}=0.1 W/cm^2		
13	800	$8.50\cdot10^{-7}$	0.022	2.17	$1.69\cdot10^{-4}$	0.0078	0.22	$7.86\cdot10^{-7}$	$7.87\cdot10^{-4}$	0.036
	400	$2.40\cdot10^{-7}$	0.022	2.22	$1.91\cdot10^{-4}$	0.0086	0.22	$8.88\cdot10^{-7}$	$8.88\cdot10^{-4}$	0.040
	200	$4.60\cdot10^{-8}$	0.018	1.99	$1.46\cdot10^{-4}$	0.0074	0.23	$5.58\cdot10^{-7}$	$5.58\cdot10^{-4}$	0.028
14	800	$7.90\cdot10^{-7}$	0.020	2.17	$1.57\cdot10^{-4}$	0.0072	0.22	$6.75\cdot10^{-7}$	$6.75\cdot10^{-4}$	0.031
	400	$4.40\cdot10^{-8}$	0.017	2.22	$3.50\cdot10^{-4}$	0.0016	0.23	$1.36\cdot10^{-7}$	$1.36\cdot10^{-4}$	0.006
	200	$9.20\cdot10^{-8}$	0.018	1.99	$2.93\cdot10^{-4}$	0.015	0.22	$1.20\cdot10^{-6}$	0.0012	0.060
15	800	$5.50\cdot10^{-7}$	0.022	2.17	$1.09\cdot10^{-4}$	0.005	0.21	$5.15\cdot10^{-7}$	$5.15\cdot10^{-4}$	0.024
	400	$1.70\cdot10^{-7}$	0.024	2.22	$1.35\cdot10^{-4}$	0.006	0.21	$6.91\cdot10^{-7}$	$6.91\cdot10^{-4}$	0.031
	200	$5.60\cdot10^{-8}$	0.022	1.99	$1.78\cdot10^{-4}$	0.009	0.22	$8.26\cdot10^{-7}$	$8.26\cdot10^{-4}$	0.042

Table 7. Extracted parameters from photo I-V for 586A sample

586B diode	Diameter µm	I_{sc} A	V_{oc} V	A_{active}/A %	j A/cm^2	j_{active} A/cm^2	FF	P_{out} W/cm^2	n %	n_act %
No anneal								P_{in}=0.1 W/cm^2		
22	800	$6.44\cdot10^{-7}$	0.015	1.41	$1.28\cdot10^{-4}$	0.009	0.23	$4.32\cdot10^{-7}$	$4.32\cdot10^{-4}$	0.031
	400	$2.50\cdot10^{-7}$	0.016	1.15	$1.99\cdot10^{-4}$	0.017	0.23	$7.20\cdot10^{-7}$	$7.20\cdot10^{-4}$	0.063
	200	$1.05\cdot10^{-7}$	0.017	1.53	$3.34\cdot10^{-4}$	0.022	0.22	$1.29\cdot10^{-6}$	0.00129	0.084
24	800	$7.71\cdot10^{-7}$	0.012	1.41	$1.53\cdot10^{-4}$	0.011	0.24	$4.52\cdot10^{-7}$	$4.52\cdot10^{-4}$	0.032
	400	$2.20\cdot10^{-7}$	0.014	1.15	$1.75\cdot10^{-4}$	0.015	0.23	$5.84\cdot10^{-7}$	$5.84\cdot10^{-4}$	0.051
	200	$9.70\cdot10^{-7}$	0.014	1.53	0.00309	0.202	0.23	$1.03\cdot10^{-5}$	0.01029	0.67
32	800	$9.20\cdot10^{-7}$	0.015	1.41	$1.83\cdot10^{-4}$	0.013	0.23	$6.43\cdot10^{-7}$	$6.43\cdot10^{-4}$	0.046
	400	$2.60\cdot10^{-7}$	0.018	1.15	$2.07\cdot10^{-4}$	0.018	0.22	$8.06\cdot10^{-7}$	$8.06\cdot10^{-4}$	0.070
	200	$1.03\cdot10^{-7}$	0.017	1.53	$3.28\cdot10^{-4}$	0.021	0.22	$1.25\cdot10^{-6}$	0.00125	0.082
33	800	$9.04\cdot10^{-7}$	0.014	1.41	$1.80\cdot10^{-4}$	0.013	0.23	$6.00\cdot10^{-7}$	$6.00\cdot10^{-4}$	0.043
	400	$3.00\cdot10^{-7}$	0.016	1.15	$2.39\cdot10^{-4}$	0.021	0.23	$8.72\cdot10^{-7}$	$8.72\cdot10^{-4}$	0.076
	200	$1.04\cdot10^{-7}$	0.017	1.53	$3.31\cdot10^{-4}$	0.022	0.22	$1.24\cdot10^{-6}$	0.00124	0.081

Table 8. Extracted parameters from photo I-V for 586B sample

586C diode	*Isc* A	*Voc* V	*Aactive/A* %	*j* A/cm^2	*jactive* A/cm^2	*FF*	P_{out} W/cm^2	n %	n_act %
No anneal.							*P_{in}=0.8 W/cm^2*		
21	$7.50\cdot10^{-6}$	*0.045*	*0.435*	$9.38\cdot10^{-4}$	*0.216*	*0.21*	$9.03\cdot10^{-6}$	*0.0011*	0.26
31	$4.20\cdot10^{-5}$	*0.087*	*0.435*	*0.0025*	*0.568*	*0.29*	$6.28\cdot10^{-5}$	*0.0079*	1.81
41	$6.07\cdot10^{-5}$	*0.086*	*0.435*	*0.0016*	*0.358*	*0.29*	$3.88\cdot10^{-5}$	*0.0049*	1.12
12	$1.30\cdot10^{-5}$	*0.0544*	*0.435*	$9.29\cdot10^{-4}$	*0.214*	*0.23*	$1.16\cdot10^{-5}$	*0.0015*	0.33
22	$2.60\cdot10^{-5}$	*0.096*	*0.435*	*0.0037*	*0.855*	*0.31*	$1.10\cdot10^{-4}$	*0.0138*	3.18
32	$2.90\cdot10^{-5}$	*0.087*	*0.435*	*0.0029*	*0.667*	*0.29*	$7.37\cdot10^{-5}$	*0.0092*	2.12
42	$3.76\cdot10^{-5}$	*0.089*	*0.543*	*0.0029*	*0.533*	*0.29*	$7.62\cdot10^{-5}$	*0.0095*	1.76
52	$4.87\cdot10^{-5}$	*0.093*	*0.409*	*0.0030*	*0.745*	*0.30*	$8.60\cdot10^{-5}$	*0.0108*	2.63
23	$1.40\cdot10^{-5}$	*0.077*	*0.435*	*0.0028*	*0.644*	*0.27*	$5.87\cdot10^{-5}$	*0.0073*	1.69
33	$3.17\cdot10^{-5}$	*0.075*	*0.435*	*0.0032*	*0.729*	*0.27*	$6.38\cdot10^{-5}$	*0.0080*	1.83
43	$3.97\cdot10^{-5}$	*0.063*	*0.357*	*0.0018*	*0.505*	*0.24*	$2.78\cdot10^{-5}$	*0.0035*	0.97
300°C							*P_{in}=0.1 W/cm^2*		
12	$1.20\cdot10^{-7}$	*0.0168*	*0.435*	$8.57\cdot10^{-6}$	$1.97\cdot10^{-3}$	0.214	$3.08\cdot10^{-8}$	$3.08\cdot10^{-5}$	0.0071
13	$4.00\cdot10^{-9}$	*0.0140*	*0.435*	$2.00\cdot10^{-6}$	$4.60\cdot10^{-4}$	0.223	$6.24\cdot10^{-9}$	$6.23\cdot10^{-6}$	0.0014
21	$8.70\cdot10^{-7}$	*0.0171*	*0.435*	$1.09\cdot10^{-4}$	$2.50\cdot10^{-2}$	0.213	$3.97\cdot10^{-7}$	$3.97\cdot10^{-4}$	0.0912
22	$9.70\cdot10^{-7}$	*0.0149*	*0.435*	$1.39\cdot10^{-4}$	$3.19\cdot10^{-2}$	0.219	$4.54\cdot10^{-7}$	$4.54\cdot10^{-4}$	0.1043
23	$9.10\cdot10^{-7}$	*0.0139*	*0.435*	$1.82\cdot10^{-4}$	$4.19\cdot10^{-2}$	0.223	$5.64\cdot10^{-7}$	$5.64\cdot10^{-4}$	0.1298
31	$3.90\cdot10^{-6}$	*0.0249*	*0.435*	$2.29\cdot10^{-4}$	$5.28\cdot10^{-2}$	0.203	$1.15\cdot10^{-6}$	$11.50\cdot10^{-4}$	0.2651
32	$2.10\cdot10^{-6}$	*0.0183*	*0.435*	$2.10\cdot10^{-4}$	$4.83\cdot10^{-2}$	0.212	$8.09\cdot10^{-7}$	$8.09\cdot10^{-4}$	0.1862
33	$2.30\cdot10^{-6}$	*0.0179*	*0.435*	$2.30\cdot10^{-4}$	$5.29\cdot10^{-2}$	0.211	$8.70\cdot10^{-7}$	$8.70\cdot10^{-4}$	0.2002
41	$8.60\cdot10^{-6}$	*0.0276*	*0.435*	$2.21\cdot10^{-4}$	$5.07\cdot10^{-2}$	0.201	$1.22\cdot10^{-6}$	$12.20\cdot10^{-4}$	0.2810
42	$4.40\cdot10^{-6}$	*0.0263*	*0.543*	$3.38\cdot10^{-4}$	$6.24\cdot10^{-2}$	0.201	$1.78\cdot10^{-6}$	$17.90\cdot10^{-4}$	0.3297
43	$4.20\cdot10^{-6}$	*0.0181*	*0.357*	$1.91\cdot10^{-4}$	$5.35\cdot10^{-2}$	0.211	$7.29\cdot10^{-7}$	$7.29\cdot10^{-4}$	0.2041
52	$4.60\cdot10^{-6}$	*0.0265*	*0.409*	$2.88\cdot10^{-4}$	$7.03\cdot10^{-2}$	0.201	$1.53\cdot10^{-6}$	$15.30\cdot10^{-4}$	0.3745

Table 9. Extracted parameters from photo I-V for 586C sample

590A diode	Diameter µm	Isc A	Voc V	Aactive/A %	j A/cm^2	jactive A/cm^2	FF	P_{out} W/cm^2	n %	n_act %
No anneal.								P_{in}=0.1 W/cm^2		
11	800	$2.30\cdot10^{-6}$	0.0242	1.10	$4.58\cdot10^{-4}$	0.0416	0.22	$2.43\cdot10^{-6}$	0.0024	0.22
	400	$5.30\cdot10^{-7}$	0.0198	1.55	$4.22\cdot10^{-4}$	0.0272	0.23	$1.92\cdot10^{-6}$	0.0019	0.12
	200	$1.60\cdot10^{-7}$	0.0229	1.23	$5.09\cdot10^{-4}$	0.0415	0.22	$2.59\cdot10^{-6}$	0.0026	0.21
23	800	$2.50\cdot10^{-6}$	0.0262	1.10	$4.97\cdot10^{-4}$	0.0452	0.22	$2.81\cdot10^{-6}$	0.0028	0.26
	400	$7.20\cdot10^{-7}$	0.0226	1.55	$5.73\cdot10^{-4}$	0.0369	0.22	$2.88\cdot10^{-6}$	0.0029	0.19
	200	$2.40\cdot10^{-7}$	0.0252	1.23	$7.64\cdot10^{-4}$	0.0623	0.22	$4.18\cdot10^{-6}$	0.0042	0.34
24	800	$2.50\cdot10^{-6}$	0.0257	1.10	$4.97\cdot10^{-4}$	0.0452	0.22	$2.76\cdot10^{-6}$	0.0028	0.25
	400	$7.10\cdot10^{-7}$	0.0217	1.55	$5.65\cdot10^{-4}$	0.0364	0.22	$2.75\cdot10^{-6}$	0.0028	0.18
	200	$2.40\cdot10^{-7}$	0.0233	1.23	$7.64\cdot10^{-4}$	0.0623	0.22	$3.93\cdot10^{-6}$	0.0039	0.32
300°C								P_{in}=0.1 W/cm^2		
11	800	$1.20\cdot10^{-6}$	0.0217	1.10	$2.39\cdot10^{-4}$	0.0217	0.22	$1.16\cdot10^{-6}$	0.0012	0.11
	400	$3.20\cdot10^{-7}$	0.0219	1.55	$2.55\cdot10^{-4}$	0.0164	0.22	$1.25\cdot10^{-6}$	0.0012	0.08
	200	$1.64\cdot10^{-7}$	0.0242	1.23	$5.22\cdot10^{-4}$	0.0426	0.22	$2.77\cdot10^{-6}$	0.0028	0.23
23	800	$2.20\cdot10^{-6}$	0.0241	1.10	$4.38\cdot10^{-4}$	0.0398	0.22	$2.31\cdot10^{-6}$	0.0023	0.21
	400	$1.20\cdot10^{-7}$	0.0205	1.55	$9.55\cdot10^{-5}$	0.0062	0.23	$4.45\cdot10^{-7}$	$4.45\cdot10^{-4}$	0.03
	200	$2.13\cdot10^{-7}$	0.0251	1.23	$6.78\cdot10^{-4}$	0.0553	0.22	$3.70\cdot10^{-6}$	0.0037	0.30
24	800	$2.10\cdot10^{-6}$	0.0211	1.10	$4.18\cdot10^{-4}$	0.0380	0.23	$1.99\cdot10^{-6}$	0.0019	0.18
	400	$5.70\cdot10^{-7}$	0.0229	1.55	$4.54\cdot10^{-4}$	0.0292	0.22	$2.30\cdot10^{-6}$	0.0023	0.15
	200	$2.10\cdot10^{-7}$	0.0242	1.23	$6.68\cdot10^{-4}$	0.0545	0.22	$3.54\cdot10^{-6}$	0.0035	0.29

Table 10. Extracted parameters from photo I-V for 590A sample

590B diode	Diameter µm	Isc A	Voc V	Aactive/A %	j A/cm^2	jactive A/cm^2	FF	P_{out} W/cm^2	n %	n_act %
No anneal.								P_{in}=0.1 W/cm^2		
33	800	$1.30\cdot10^{-6}$	0.023	2.4	$2.59\cdot10^{-4}$	0.011	0.21	$1.27\cdot10^{-6}$	0.0013	0.053
	400	$5.30\cdot10^{-7}$	0.022	2.14	$4.22\cdot10^{-4}$	0.02	0.22	$2.00\cdot10^{-6}$	0.002	0.093
	200	$1.40\cdot10^{-7}$	0.02	2.17	$4.46\cdot10^{-4}$	0.021	0.22	$1.96\cdot10^{-6}$	0.002	0.09
34	800	$1.40\cdot10^{-6}$	0.0248	2.4	$2.79\cdot10^{-4}$	0.012	0.21	$1.45\cdot10^{-6}$	0.0015	0.06
	400	$5.06\cdot10^{-7}$	0.0218	2.14	$4.03\cdot10^{-4}$	0.019	0.22	$1.90\cdot10^{-6}$	0.0019	0.089
	200	$1.55\cdot10^{-7}$	0.0211	2.17	$4.93\cdot10^{-4}$	0.022	0.22	$2.26\cdot10^{-6}$	0.0023	0.104
42	800	$1.34\cdot10^{-6}$	0.023	2.4	$2.67\cdot10^{-4}$	0.011	0.21	$1.31\cdot10^{-6}$	0.0013	0.055
	400	$5.20\cdot10^{-7}$	0.022	2.14	$4.14\cdot10^{-4}$	0.019	0.22	$1.96\cdot10^{-6}$	0.002	0.092
	200	$1.55\cdot10^{-7}$	0.024	2.17	$4.93\cdot10^{-4}$	0.023	0.21	$2.51\cdot10^{-6}$	0.0025	0.115

43	800	$1.39\cdot10^{-6}$	0.0219	2.4	$2.77\cdot10^{-4}$	0.012	0.22	$1.31\cdot10^{-6}$	0.0013	0.054
	400	$4.90\cdot10^{-7}$	0.0224	2.14	$3.90\cdot10^{-4}$	0.018	0.21	$1.88\cdot10^{-6}$	0.0019	0.087
	200	$1.50\cdot10^{-7}$	0.0251	2.17	$4.77\cdot10^{-4}$	0.022	0.21	$2.52\cdot10^{-6}$	0.0025	0.115

Table 11. Extracted parameters from photo I-V for 590B sample

590C diode	Isc A	Voc V	Aactive/A %	j A/cm^2	jactive A/cm^2	FF	P_{out} W/cm^2	n %	n_act %
No anneal.							P_{in}=0.8 W/cm^2		
11	$9.80\cdot10^{-5}$	0.106	0.951	0.0070	0.735	0.260	$1.94\cdot10^{-4}$	0.0242	2.54
12	$1.50\cdot10^{-4}$	0.180	1.334	0.0083	0.625	0.355	$5.33\cdot10^{-4}$	0.0667	4.99
22	$6.02\cdot10^{-5}$	0.059	0.951	0.0013	0.140	0.207	$1.64\cdot10^{-4}$	0.0020	0.21
13	$1.70\cdot10^{-4}$	0.120	1.028	0.0035	0.345	0.279	$1.19\cdot10^{-4}$	0.0149	1.44
32	$1.60\cdot10^{-4}$	0.038	0.952	0.0029	0.306	0.201	$2.23\cdot10^{-5}$	0.0028	0.29
14	$1.80\cdot10^{-4}$	0.115	0.952	0.0036	0.378	0.273	$1.13\cdot10^{-4}$	0.0141	1.48
24	$1.60\cdot10^{-4}$	0.075	0.952	0.0039	0.410	0.222	$6.51\cdot10^{-5}$	0.0081	0.85
15	$1.90\cdot10^{-4}$	0.113	0.952	0.0043	0.454	0.270	$1.32\cdot10^{-4}$	0.0165	1.73
25	$1.50\cdot10^{-4}$	0.121	0.952	0.0048	0.508	0.281	$1.64\cdot10^{-4}$	0.0205	2.16
16	$1.90\cdot10^{-4}$	0.106	0.495	0.0037	0.738	0.261	$1.01\cdot10^{-4}$	0.0126	2.55
26	$1.50\cdot10^{-4}$	0.116	0.952	0.0048	0.508	0.274	$1.54\cdot10^{-4}$	0.0192	2.02
300°C							P_{in}=0.1 W/cm^2		
11	$1.05\cdot10^{-5}$	0.0071	0.952	0.0075	0.078	0.277	$1.47\cdot10^{-6}$	0.0015	0.15
21	$2.40\cdot10^{-5}$	0.0068	0.952	0.0013	0.133	0.279	$2.39\cdot10^{-6}$	0.0024	0.25
12	$3.50\cdot10^{-7}$	0.0359	1.330	$1.94\cdot10^{-5}$	0.002	0.202	$1.41\cdot10^{-7}$	0.0001	0.01
22	$2.02\cdot10^{-5}$	0.0141	0.952	0.0004	0.047	0.244	$1.54\cdot10^{-6}$	0.0015	0.16
13	$5.50\cdot10^{-7}$	0.0351	1.030	$1.15\cdot10^{-5}$	0.001	0.2032	$8.15\cdot10^{-8}$	$8.15\cdot10^{-5}$	0.01
32	$5.00\cdot10^{-5}$	0.0089	0.952	0.0009	0.096	0.267	$2.16\cdot10^{-6}$	0.0022	0.23
14	$4.00\cdot10^{-10}$	0.0341	0.952	$8.00\cdot10^{-9}$	$8.40\cdot10^{-7}$	0.203	$5.54\cdot10^{-11}$	$5.54\cdot10^{-8}$	$5.8\cdot10^{-6}$
24	$2.18\cdot10^{-5}$	0.0239	0.952	0.0005	0.056	0.216	$2.75\cdot10^{-6}$	0.0027	0.29
15	$2.40\cdot10^{-5}$	0.0342	0.952	$5.45\cdot10^{-4}$	0.057	0.203	$3.79\cdot10^{-6}$	0.0038	0.40
25	$1.62\cdot10^{-5}$	0.0337	0.952	$5.23\cdot10^{-4}$	0.055	0.204	$3.59\cdot10^{-6}$	0.0036	0.38
16	$2.90\cdot10^{-5}$	0.0336	0.495	$5.58\cdot10^{-4}$	0.113	0.204	$3.82\cdot10^{-6}$	0.0038	0.77
26	$1.40\cdot10^{-5}$	0.0335	0.952	$4.52\cdot10^{-4}$	0.047	0.204	$3.08\cdot10^{-6}$	0.0031	0.32

Table 12. Extracted parameters from photo I-V for 590C sample

591A diode	Diameter µm	Isc A	Voc V	Aactive/A %	j A/cm^2	jactive A/cm^2	FF	P_{out} W/cm^2	n %	n_act %
No anneal.								P_{in}=0.1 W/cm^2		
22	800	$1.30\cdot10^{-7}$	0.020	0.284	$2.59\cdot10^{-5}$	0.0091	0.225	$1.13\cdot10^{-7}$	$1.13\cdot10^{-4}$	0.039
	400	$3.00\cdot10^{-8}$	0.020	0.304	$2.39\cdot10^{-5}$	0.0079	0.224	$1.06\cdot10^{-7}$	$1.06\cdot10^{-4}$	0.034
	200	$3.00\cdot10^{-9}$	0.025	0.344	$9.55\cdot10^{-6}$	0.0028	0.212	$5.15\cdot10^{-8}$	$5.15\cdot10^{-5}$	0.014
32	800	$2.90\cdot10^{-7}$	0.023	0.284	$5.77\cdot10^{-5}$	0.0203	0.217	$2.85\cdot10^{-7}$	$2.85\cdot10^{-4}$	0.100
	400	$1.00\cdot10^{-7}$	0.022	0.304	$7.96\cdot10^{-5}$	0.0262	0.22	$3.76\cdot10^{-7}$	$3.76\cdot10^{-4}$	0.124
	200	$1.60\cdot10^{-8}$	0.020	0.344	$5.09\cdot10^{-5}$	0.0148	0.224	$2.25\cdot10^{-7}$	$2.25\cdot10^{-4}$	0.065
33	800	$3.20\cdot10^{-7}$	0.025	0.284	$6.37\cdot10^{-5}$	0.0224	0.213	$3.37\cdot10^{-7}$	$3.37\cdot10^{-4}$	0.118
	400	$9.50\cdot10^{-8}$	0.024	0.304	$7.56\cdot10^{-5}$	0.0248	0.215	$3.87\cdot10^{-7}$	$3.87\cdot10^{-4}$	0.127
	200	$1.60\cdot10^{-8}$	0.014	0.344	$5.09\cdot10^{-5}$	0.0148	0.242	$1.75\cdot10^{-7}$	$1.75\cdot10^{-4}$	0.051
34	800	$3.06\cdot10^{-7}$	0.023	0.284	$6.09\cdot10^{-5}$	0.0214	0.217	$3.02\cdot10^{-7}$	$3.02\cdot10^{-4}$	0.106
	400	$9.40\cdot10^{-8}$	0.021	0.304	$7.48\cdot10^{-5}$	0.0246	0.221	$3.50\cdot10^{-7}$	$3.50\cdot10^{-4}$	0.115
	200	$1.40\cdot10^{-8}$	0.019	0.344	$4.46\cdot10^{-5}$	0.0129	0.225	$1.95\cdot10^{-7}$	$1.95\cdot10^{-4}$	0.057
35	800	$3.20\cdot10^{-7}$	0.025	0.284	$6.37\cdot10^{-5}$	0.0224	0.213	$3.34\cdot10^{-7}$	$3.34\cdot10^{-4}$	0.117
	400	$9.40\cdot10^{-8}$	0.023	0.304	$7.48\cdot10^{-5}$	0.0246	0.217	$3.70\cdot10^{-7}$	$3.70\cdot10^{-4}$	0.122
	200	$6.40\cdot10^{-8}$	0.019	0.344	$2.04\cdot10^{-4}$	0.0592	0.226	$8.82\cdot10^{-7}$	$8.82\cdot10^{-4}$	0.256
43	800	$2.20\cdot10^{-7}$	0.020	0.284	$4.38\cdot10^{-5}$	0.0154	0.224	$1.93\cdot10^{-7}$	$1.93\cdot10^{-4}$	0.068
	400	$4.50\cdot10^{-8}$	0.019	0.304	$3.58\cdot10^{-5}$	0.0118	0.226	$1.54\cdot10^{-7}$	$1.54\cdot10^{-4}$	0.051
	200	$2.60\cdot10^{-8}$	0.019	0.344	$8.28\cdot10^{-5}$	0.024	0.227	$3.51\cdot10^{-7}$	$3.51\cdot10^{-4}$	0.102
300°C								P_{in}=0.1W/cm^2		
33	800	$1.50\cdot10^{-8}$	0.020	0.284	$2.98\cdot10^{-6}$	0.0011	0.223	$1.34\cdot10^{-8}$	$1.34\cdot10^{-5}$	0.005
	400	$7.20\cdot10^{-9}$	0.019	0.304	$5.73\cdot10^{-6}$	0.0019	0.227	$2.44\cdot10^{-8}$	$2.44\cdot10^{-5}$	0.008
	200	$1.30\cdot10^{-10}$	0.021	0.344	$4.14\cdot10^{-7}$	0.0001	0.221	$1.93\cdot10^{-9}$	$1.93\cdot10^{-6}$	0.0006
34	800	$2.10\cdot10^{-8}$	0.021	0.284	$4.18\cdot10^{-6}$	0.0015	0.221	$1.95\cdot10^{-8}$	$1.95\cdot10^{-5}$	0.007
	400	$7.50\cdot10^{-9}$	0.024	0.304	$5.97\cdot10^{-6}$	0.002	0.215	$3.08\cdot10^{-8}$	$3.08\cdot10^{-5}$	0.010

	200	$4.00\cdot10^{-8}$	*0.022*	*0.344*	$1.27\cdot10^{-4}$	*0.037*	*0.218*	$6.22\cdot10^{-7}$	$6.22\cdot10^{-4}$	**0.181**
43	*800*	$1.20\cdot10^{-8}$	*0.020*	*0.284*	$2.39\cdot10^{-6}$	*0.0008*	*0.223*	$1.08\cdot10^{-8}$	$1.08\cdot10^{-5}$	**0.004**
	400	$4.50\cdot10^{-9}$	*0.024*	*0.304*	$3.58\cdot10^{-6}$	*0.0012*	*0.216*	$1.82\cdot10^{-8}$	$1.82\cdot10^{-5}$	**0.006**
	200	$1.01\cdot10^{-7}$	*0.021*	*0.344*	$3.21\cdot10^{-4}$	*0.0934*	*0.221*	$1.49\cdot10^{-6}$	*0.00149*	**0.432**

Table 13. Extracted parameters from photo I-V for 591A sample

591B	*Isc*	*Voc*	*Aactive/A*	*j*	*jactive*	*FF*	*P'*	**n**	**n_act**
diode	**A**	**V**	**%**	**A/cm²**	**A/cm²**		**W/cm²**	**%**	**%**
No anneal.							$P_{in}=0.8\ W/cm^2$		
11	$2.70\cdot10^{-4}$	*0.110*	*0.120*	*0.0044*	*3.603*	*0.264*	$1.26\cdot10^{-4}$	*0.0158*	**13.08**
11nd1	$3.10\cdot10^{-5}$	*0.026*	*0.121*	*0.0005*	*0.413*	*0.213*	$2.77\cdot10^{-6}$	*0.0034*	**0.29**
21	$1.90\cdot10^{-4}$	*0.130*	*0.103*	*0.0046*	*4.508*	*0.29*	$1.75\cdot10^{-4}$	*0.0219*	**21.26**
31	$1.30\cdot10^{-4}$	*0.122*	*0.103*	*0.0035*	*3.418*	*0.28*	$1.20\cdot10^{-4}$	*0.015*	**14.58**
12	$2.30\cdot10^{-4}$	*0.128*	*0.091*	*0.0068*	*7.422*	*0.288*	$2.49\cdot10^{-4}$	*0.0311*	**34.15**
22	$1.60\cdot10^{-4}$	*0.124*	*0.103*	*0.0036*	*3.538*	*0.282*	$1.27\cdot10^{-4}$	*0.0159*	**15.48**
32	$1.60\cdot10^{-4}$	*0.117*	*0.103*	*0.0042*	*4.096*	*0.273*	$1.35\cdot10^{-4}$	*0.0168*	**16.36**
42	$1.39\cdot10^{-4}$	*0.140*	*0.096*	*0.0077*	*8.014*	*0.303*	$3.28\cdot10^{-4}$	*0.041*	**42.51**
13	$9.20\cdot10^{-5}$	*0.144*	*0.103*	*0.0054*	*5.265*	*0.308*	$2.40\cdot10^{-4}$	*0.03*	**29.21**
23	$1.70\cdot10^{-4}$	*0.118*	*0.103*	*0.0061*	*5.907*	*0.274*	$1.97\cdot10^{-4}$	*0.0246*	**23.91**
33	$7.30\cdot10^{-5}$	*0.155*	*0.103*	*0.0061*	*5.918*	*0.322*	$3.04\cdot10^{-4}$	*0.0379*	**36.93**
300°C							$P_{in}=0.1\ W/cm^2$		
11	$1.70\cdot10^{-5}$	*0.048*	**0.121**	$2.74\cdot10^{-4}$	*0.227*	*0.2011*	$2.64\cdot10^{-6}$	*0.0026*	**2.18**
21	$1.90\cdot10^{-5}$	*0.048*	**0.103**	$4.63\cdot10^{-4}$	*0.451*	*0.2012*	$4.48\cdot10^{-6}$	*0.0045*	**4.36**
31	$1.30\cdot10^{-5}$	*0.048*	**0.103**	$3.51\cdot10^{-4}$	*0.342*	*0.2011*	$3.38\cdot10^{-6}$	*0.0034*	**3.29**
12	$1.40\cdot10^{-5}$	*0.048*	**0.091**	$4.12\cdot10^{-4}$	*0.452*	*0.2011*	$3.95\cdot10^{-6}$	*0.004*	**4.33**
22	$1.60\cdot10^{-5}$	*0.048*	**0.103**	$3.64\cdot10^{-4}$	*0.354*	*0.2011*	$3.50\cdot10^{-6}$	*0.0035*	**3.4**
32	$5.80\cdot10^{-6}$	*0.048*	**0.103**	$1.53\cdot10^{-4}$	*0.148*	*0.2012*	$1.48\cdot10^{-6}$	*0.0015*	**1.44**
42	$5.10\cdot10^{-6}$	*0.048*	**0.096**	$2.83\cdot10^{-4}$	*0.294*	*0.2013*	$2.76\cdot10^{-6}$	*0.0028*	**2.86**
23	$6.10\cdot10^{-6}$	*0.047*	**0.103**	$2.18\cdot10^{-4}$	*0.212*	*0.201*	$2.08\cdot10^{-6}$	*0.0021*	**2.02**
33	$3.10\cdot10^{-6}$	*0.039*	**0.103**	$2.58\cdot10^{-4}$	*0.251*	*0.2014*	$2.01\cdot10^{-6}$	*0.002*	**1.95**

Table 14. Extracted parameters from photo I-V for 591B sample

References

[1] S. Sharma, K. K. Jain, and A. Sharma, "Solar Cells: In Research and Applications—A Review," *Mater. Sci. Appl.*, vol. 06, no. 12, pp. 1145–1155, 2015.

[2] G. Otnes and M. T. Borgström, "Towards high efficiency nanowire solar cells," *Nano Today*, vol. 12, pp. 31–45, Feb. 2017.

[3] F. Jabeen, S. Rubini, V. Grillo, L. Felisari, and F. Martelli, "Room temperature luminescent InGaAs/GaAs core-shell nanowires," *Appl. Phys. Lett.*, vol. 93, no. 8, p. 083117, Aug. 2008.

[4] K. Moratis *et al.*, "Strained GaAs/InGaAs Core-Shell Nanowires for Photovoltaic Applications," *Nanoscale Res. Lett.*, vol. 11, no. 1, Dec. 2016.

[5] M. Hocevar *et al.*, "Residual strain and piezoelectric effects in passivated GaAs/AlGaAs core-shell nanowires," *Appl. Phys. Lett.*, vol. 102, no. 19, p. 191103, May 2013.

[6] S. Mokkapati and C. Jagadish, "Review on photonic properties of nanowires for photovoltaics [Invited]," *Opt. Express*, vol. 24, no. 15, p. 17345, Jul. 2016.

[7] H. Cotal *et al.*, "III–V multijunction solar cells for concentrating photovoltaics," *Energy Env. Sci*, vol. 2, no. 2, pp. 174–192, 2009.

[8] S. R. Wenham, Ed., *Applied photovoltaics*, 2nd ed. London ; Sterling, VA: Earthscan, 2007.

[9] W. Shockley and H. J. Queisser, "Detailed Balance Limit of Efficiency of *p-n* Junction Solar Cells," *J. Appl. Phys.*, vol. 32, no. 3, pp. 510–519, Mar. 1961.

[10] R. Garner, "Solar Irradiance." NASA, 01-Jan-2008.

[11] A. Fick, "Ueber Diffusion," *Ann. Phys. Chem.*, vol. 170, no. 1, pp. 59–86, 1855.

[12] P. Drude, "Zur Elektronentheorie der Metalle; II. Teil. Galvanomagnetische und thermomagnetische Effecte," *Ann. Phys.*, vol. 308, no. 11, pp. 369–402, 1900.

[13] P. Drude, "Zur Elektronentheorie der Metalle," *Ann. Phys.*, vol. 306, no. 3, pp. 566–613, 1900.

[14] P. A. Basore, "Numerical modeling of textured silicon solar cells using PC-1D," *IEEE Trans. Electron Devices*, vol. 37, no. 2, pp. 337–343, Feb. 1990.

[15] W. Shockley and W. T. Read, "Statistics of the Recombinations of Holes and Electrons," *Phys. Rev.*, vol. 87, no. 5, pp. 835–842, Sep. 1952.

[16] O. Hardouin Duparc, "Pierre Auger – Lise Meitner: Comparative contributions to the Auger effect," *Int. J. Mater. Res.*, vol. 100, no. 9, pp. 1162–1166, Sep. 2009.

[17] A. Goetzberger, J. Knobloch, and B. Voss, *Crystalline silicon solar cells*. Chichester : New York: Wiley, 1998.

[18] M. A. Green, *Solar cells: operating principles, technology, and system applications*. Englewood Cliffs, NJ: Prentice-Hall, 1982.

[19] J. V. Holm, "Nanowire Growth for Photovoltaics," Copenhagen, 2013.

[20] J. Nelson, *The Physics of Solar Cells*. PUBLISHED BY IMPERIAL COLLEGE PRESS AND DISTRIBUTED BY WORLD SCIENTIFIC PUBLISHING CO., 2003.

[21] F. A. Lindholm, J. G. Fossum, and E. L. Burgess, "Application of the superposition principle to solar-cell analysis," *IEEE Trans. Electron Devices*, vol. 26, no. 3, pp. 165–171, Mar. 1979.

[22] M. A. Green, "Solar cell fill factors: General graph and empirical expressions," *Solid-State Electron.*, vol. 24, no. 8, pp. 788–789, Aug. 1981.

[23] M. Chegaar, A. Hamzaoui, A. Namoda, P. Petit, M. Aillerie, and A. Herguth, "Effect of Illumination Intensity on Solar Cells Parameters," *Energy Procedia*, vol. 36, pp. 722–729, 2013.

[24] E. E. van Dyk and E. L. Meyer, “Analysis of the effect of parasitic resistances on the performance of photovoltaic modules,” *Renew. Energy*, vol. 29, no. 3, pp. 333–344, Mar. 2004.
[25] C. Kittel and H. Kroemer, *Thermal physics*, 2d ed. San Francisco: W. H. Freeman, 1980.
[26] S. Arrhenius, “Zeitschrift für Physikalische Chemie,” 1889.
[27] H.-J. Choi, “Vapor–Liquid–Solid Growth of Semiconductor Nanowires,” in *Semiconductor Nanostructures for Optoelectronic Devices*, G.-C. Yi, Ed. Berlin, Heidelberg: Springer Berlin Heidelberg, 2012, pp. 1–36.
[28] G. Otnes and M. T. Borgström, “Towards high efficiency nanowire solar cells,” *Nano Today*, vol. 12, pp. 31–45, Feb. 2017.
[29] S. L. Tan, Y. Genuist, M. I. den Hertog, E. Bellet-Amalric, H. Mariette, and N. T. Pelekanos, “Highly uniform zinc blende GaAs nanowires on Si(111) using a controlled chemical oxide template,” *Nanotechnology*, vol. 28, no. 25, p. 255602, Jun. 2017.
[30] R. A. Stradling, P. Klipstein, Imperial College of Science, Technology and Medicine, and Imperial College of Science, Technology and Medicine, Eds., *Growth and characterisation of semiconductors*. Bristol [England] ; New York: Hilger, 1990.
[31] J. J. Hannan, “Growth and Characterization of III–V Semiconductor Nanowires for Optoelectronic Device Applications,” Doctor of Philosophy thesis, Australian National University, 2009.
[32] R. E. Nahory, M. A. Pollack, W. D. Johnston, and R. L. Barns, “Band gap versus composition and demonstration of Vegard’s law for $In_{1-x}Ga_xAs_yP_{1-y}$ lattice matched to InP,” *Appl. Phys. Lett.*, vol. 33, no. 7, pp. 659–661, Oct. 1978.
[33] M. Murayama and T. Nakayama, “Chemical trend of band offsets at wurtzite/zinc-blende heterocrystalline semiconductor interfaces,” *Phys. Rev. B*, vol. 49, no. 7, pp. 4710–4724, Feb. 1994.
[34] F. Martelli, M. G. Proietti, M. G. Simeone, M. R. Bruni, and M. Zugarini, “Room-temperature photoluminescence in strained quantum wells of InGaAs/GaAs grown by molecular-beam epitaxy,” *J. Appl. Phys.*, vol. 71, no. 1, pp. 539–541, Jan. 1992.
[35] L. Pavesi and M. Guzzi, “Photoluminescence of AlxGa1−xAs alloys,” *J. Appl. Phys.*, vol. 75, no. 10, pp. 4779–4842, May 1994.
[36] G. Zhang, K. Tateno, H. Sanada, T. Tawara, H. Gotoh, and H. Nakano, “Synthesis of GaAs nanowires with very small diameters and their optical properties with the radial quantum-confinement effect,” *Appl. Phys. Lett.*, vol. 95, no. 12, p. 123104, Sep. 2009.
[37] E. H. Bogardus and H. B. Bebb, “Bound-Exciton, Free-Exciton, Band-Acceptor, Donor-Acceptor, and Auger Recombination in GaAs,” *Phys. Rev.*, vol. 176, no. 3, pp. 993–1002, Dec. 1968.
[38] L. V. Titova *et al.*, “Temperature dependence of photoluminescence from single core-shell GaAs–AlGaAs nanowires,” *Appl. Phys. Lett.*, vol. 89, no. 17, p. 173126, Oct. 2006.
[39] S. Perera *et al.*, “Nearly intrinsic exciton lifetimes in single twin-free GaAs⁄AlGaAs core-shell nanowire heterostructures,” *Appl. Phys. Lett.*, vol. 93, no. 5, p. 053110, Aug. 2008.
[40] T. Kehagias *et al.*, “Nanostructure and strain properties of core-shell GaAs/AlGaAs nanowires,” *Semicond. Sci. Technol.*, vol. 30, no. 11, p. 114012, Nov. 2015.
[41] E. Dimakis *et al.*, “Coaxial Multishell (In,Ga)As/GaAs Nanowires for Near-Infrared Emission on Si Substrates,” *Nano Lett.*, vol. 14, no. 5, pp. 2604–2609, May 2014.

[42] A. C. Farrell, P. Senanayake, X. Meng, N. Y. Hsieh, and D. L. Huffaker, “Diode Characteristics Approaching Bulk Limits in GaAs Nanowire Array Photodetectors,” *Nano Lett.*, vol. 17, no. 4, pp. 2420–2425, Apr. 2017.
[43] P. Krogstrup *et al.*, “Single-nanowire solar cells beyond the Shockley–Queisser limit,” *Nat. Photonics*, vol. 7, no. 4, pp. 306–310, Apr. 2013.
[44] E. Nakai, M. Chen, M. Yoshimura, K. Tomioka, and T. Fukui, “InGaAs axial-junction nanowire-array solar cells,” *Jpn. J. Appl. Phys.*, vol. 54, no. 1, p. 015201, Jan. 2015.